Experimental and Analytical Tools for Rapid Development of Digital Imaging-based Elasto-Tomography Technology

Hina Muhammad Ismail

A thesis submitted for the degree of

Doctor of Philosophy

in

Mechanical Engineering

Centre of Bioengineering

at the

University of Canterbury,

Christchurch, New Zealand

February 2018

Dedicated to

My husband **Muhammad Atir Ashfaque** (*Love you*)

My father and father in-law, **Muhammad Ismail** (Late) and **Muhammad Ashfaque Asim**,

My mother and mother in-law, **Khair-un-nissa** and **Aasma Ashfaque**

My respected supervisor Professor **J. Geoffrey Chase** (Thank you for your motivation)

All my family and friends for their immensurable support and love

Acknowledgements

Thanks to ALLAH, the most gracious and the most merciful, for His guidance to accomplish this research. Without His help and mercy, this would not been possible. HE is the one who knows the hardships and HE is the one I seek HIS satisfaction and ask HIS acceptance.

I would like to express my deepest gratitude towards my supervisors, Professor J. Geoffrey Chase, Dr. Christopher G. Pretty, and Dr. Matthew K. Signal, and advisor Marcus Haggers for their guidance, encouragement and valuable comments during the research and writing of this dissertation. Their attention and technical expertise were key elements to my success. I am satisfied in gaining an in depth knowledge from them.

I wish to express my appreciation to my bio-engineering lab members for their generous cooperation, hospitality, time and insight on related matters during this research.

My appreciation goes to University of Canterbury (UC). The working environment here in UC was very pleasant, encouraging and supportive towards my study.

Special thank goes to my parents, Muhammad Ashfaque Asim (father-in-law), Aasma Ashfaque (mother-in-law), Muhammad Ismail (father), and Khair-un-nissa (mother) and family members for their patience during my academic career. Their concern, care, encouragement, and moral support over the years has always been a source of motivation that enables me to achieve this degree.

I would like to thank my siblings, Zakir, Sofia, Yasir, Amir, Sana, Imran, Anas, and Aabra for their moral support and care during my PhD.

Last but not the least, special thanks to my best friend, my husband Muhammad Atir Ashfaque for his unconditional love and support during my education.

Contents

List of Figures

List of Tables

Nomenclature

DIET	Digital Imaged Elasto-Tomography
DCIS	Ductal carcinoma in situ
LCIS	Lobular carcinoma in situ
XM	X-ray mammography
MRI	Magnetic resonance imaging
US	Ultrasound
TG	Thermography
MI	Microwave imaging
TPR	True positive rate (Sensitivity)
TNR	True negative rate (Specificity)
FNR	False negative rate
FPR	False positive rate
NA	Not available
E	Elastic modulus
MTS	Mechanical test and simulation
DMA	Dynamic mechanical analysis
W	Strain energy density
I_1	Deviatoric strain invariant
DAQ	Data acquisition
λ	Stretch ratio
μ	Shear modulus
N	Newton
E^*	Complex elastic modulus
E'	Storage modulus
E''	Loss modulus
NH	Neo-Hookean
MR	Mooney Rivlin
FE	Finite element
OF	Optical flow
LDV	Laser Doppler vibrometer

Abstract

Breast cancer is the second most common cancer in the world and has the highest cancer mortality rate in women. Presently, 1 of every 4 women carry an increased risk of breast cancer, of which, 6% are below the minimum screening age of 45. Early detection via regular screening not only reduces mortality rates, but also decreases overall treatment expenditure. X-ray mammography is the clinical standard breast cancer screening technique. However, due to significant limitations, such as unacceptable rates of false positive and false negative results, exposure to ionizing radiation, and discomfort and pain due to the compression of the breast it is not recommended for women under 45 years of age. These women also often have denser breast tissues, which further reduce mammography efficacy and diagnostic capability.

Digital imaged elasto-tomography (DIET) has been developed to overcome some of the limitations of current techniques and mammography in particular. The digital imaged elasto-tomography (DIET) concept is based on non-invasive, pain-free, vibration based analysis of local tissue stiffness, a form of elastographic reconstruction from actuation motion. This technique enables early detection of breast cancer, as it is not restricted in the ages of women who could utilize it for screening. Thus, combined with effective treatment, it could reduce mortality, particularly for younger women. More specifically, recent analysis showing annual mammography down to 40 years of age would save many more lives than current screening, indicating a system like DIET, safely offering screening to any age, could significantly improve breast cancer mortality.

DIET is a novel method and technology, but is not yet at a stage suitable for a large randomised clinical trial. However, its development could be significantly enhanced by a series of tools to improve the speed and repeatability of DIET technology development. Currently, DIET is developed primary by executing pilot clinical testing of human volunteers. This experimental approach is slow, not repeatable as technology progresses and thus not necessarily optima, as well as placing a burden on diagnosed volunteer patients. In particular, repeating trials is not possible, limiting the ability to accurately assess technological changes.

The productivity of DIET technology development could thus be enhanced in three main areas: a) development of realistic and accurate tissue mimicking breast phantoms; b) validation of the surface measurement algorithms to quantify their error and thus to quantify the limits of diagnostic algorithms; and c) development of finite element models to accurately mimic breast phantoms to avoid repeated phantom experiments. The first would allow repeatable phantom trials in lieu of relying on volunteers. The second would enable more accurate assessment of errors and their impact on surface motion diagnostics. Equally, it would also allow assessment of whether improvements in sensing or actuation would make a clinical differences. The final, third element would further improve productivity by replacing phantom tests with models to generate "data". The overall outcome is significantly enhanced development pathways.

In this thesis, mechanical properties of three different materials; agar, gelatine, and silicone used to emulate the mechanical behavior of real breast tissue are measured to assess their suitability for use in phantoms in systems assessing tissue mechanics for diagnostics. The stiffness ratio of adipose to tumor between the phantom materials and real human tissues were compared. Hyperelastic parameters of Neo-Hookean, Mooney Rivil, and Ogden models were obtained for the selected silicone material due to its appropriate mechanical properties,

reliability, and repeatability. Finally, silicone based three homogenous phantoms of selected material were fabricated with different sizes of tumor.

Finite element models of breast shaped phantoms were developed using ABAQUS software. The geometry of the model was constructed with the same dimensions from fabricated phantoms. The mechanical properties were modeled by using the Neo-Hookean hyperelastic material model. Results showed good to strong correlation ranging from 0.7 to 1.0 in all cases with over 90% having a value over 0.9.Overall, the comparison of the DIET experimental data and the FE model data showed good agreement.

A single point laser Doppler vibrometer was used to validate the optical flow motion measuring algorithm used in DIET experimental data. Results show excellent validation with errors less than 6 % for healthy phantom, and errors less than 8 % for 10 mm and 20 mm inclusions. Overall results show the optical flow algorithm is validated with relatively small errors compared to a gold-standard, non-contact laser measurement.

Finally, because of the validation effectiveness and accuracy of finite element modeling compared to DIET experimental data. Six new phantoms were modeled with different tumor positions. This analysis assess the impact of tumor position on diagnosis of breast cancer using surface motions and basic elastography assumptions, which should further impact and encourage the development of DIET.

Overall, all 3 goals are accomplished. The results of this thesis provide means to dramatically speed up development of the DIET system. More generally, they provide significant results to enable elastographic technology development.

Chapter 1: Introduction

Breast cancer is a leading cause of death among women [1]. In 2012 almost 1.67 million new cases were diagnosed worldwide with approximately 324,000 and 198,000 deaths recorded in less and more developed regions, respectively [2]. Table 1 shows a summary of breast cancer worldwide in 2012 by the World Health Organization [3]. Regardless of advances in treatment over the past decades, breast cancer still remains the second leading cause of cancer related death in women [4]. The American Cancer Society estimated the number of new breast cancer cases and at 234,190, with around 40,730 deaths in the United States during 2015 alone [5] . Of these deaths, 10,000 – 12, 000 cases are invasive cancer in women less than 40 years who are not typically screened [6], with around 3000 deaths in women aged less than 45 [7].

Breast cancer is also the leading cause of cancer related deaths in New Zealand [8]. Approximately 3100 cases of breast cancer were registered in New Zealand in 2012, which is 1 in every 1355 people in New Zealand [3]. Maori women are 28% more likely to be diagnosed with breast cancer, and 68% more likely to die from it, reflecting issues with genetics and compliance to screening [9]. The more common the cancer, the higher the results premature mortality rate.

Breast cancer can affect both men and women of any age, but the incidence is much higher in women [10]. Several other factors increase the risk of developing breast cancer, including a family history, environmental factors, lifestyle, for example alcohol, diet and activity,

hormone status, reproductive factors, and radiation exposure [11, 12]. The two most significant risk factors for women are family history and increasing age [13]. Thus, for example, risk of breast cancer increased for women of all ages in Hiroshima and Nagasaki due to low dose radiation exposure [12]. Nulliparity, early menarche, late menopause also increase womens' risk of developing breast cancer. Finally, during womens' reproductive years the ovary produces steroid hormones that directly affect development and function of the breast.[14, 15].

Table 1.1: Breast cancer worldwide in 2012 by World Health Organization [3]

Regions	**Cases**	**Deaths**	**5 year- prev**
Africa	99760	49061	317873
United states of America	232714	43909	970693
East Mediterranean	99284	42228	347565
Europe	494076	142979	1936362
South-East Asia	239612	109631	734902
West Pacific	329762	85837	1276205
China	187213	47984	697327
India	144937	70218	396991

Cancer treatments are expensive. In the United States breast cancer remains one of the most costly cancers [16]. In 2010, the United States spent approximately $16.5 billion on breast cancer treatment [17]. Reducing the cost of treatments and balancing patient needs with available healthcare resources is far from easy or intuitive. Using breast cancer related health insurance claims, Ray et al. [18] showed increased follow up periods for breast cancer patients were associated with reduced mean monthly per patient costs. However, the cumulative costs per patient increased from US$78,882 for a follow up period of <6 months to US$443,062 for a follow up period of >36 months, indicating timely treatment is cost effective over time. Similarly, early detection of breast cancer screening not only reduces

mortality rate, but also decreases overall treatment expenditure [19, 20]. Thus, screening programs for the early detection of breast cancer are a key element for increasing the chances of successful treatment and reducing costs.

There are several tests and examinations routinely used for the detection of breast cancer [21-23]. To reduce breast cancer mortality rates, breast screening needs to be accurate [24], low cost, fast, and available without risk to women of all ages. However, such systems do not currently exist.

The digital imaged elasto-tomography (DIET) concept is based on non-invasive, vibration based analysis of local tissue stiffness elastographic reconstruction [25-30]. The DIET system consists of 5 digital cameras and synchronized strobe lights to capture steady state surface motion in response to 16 – 50 Hz low amplitude sinusoidal mechanical actuation applied to the breast [31]. Several images are captured during one cycle of a given actuation frequency at different phases relative to the input motion [32-36]. Surface motions are used to assess local tissue stiffness for diagnosis of stiffer inclusions e.g. [27, 28]. Recent analysis showing annual mammography down to 40 years of age would save many more lives than current screening [37], indicates a system like DIET, safely offering screening to any age could improve breast cancer mortality.

1.1 Basic overall anatomy of the breast

The healthy breast contains glandular, fatty, and fibrous tissues located over the pectoral muscles of the chest wall and connected to the chest wall by fibrous strands. Figure 1.1 shows the anatomy of the breast.

The glandular tissue includes both ducts and lobules. Each female breast is structured into 15 – 20 lobe sections. Each lobe consists of many smaller lobules, where milk is produced, which connect through a tiny tubes called ducts that lead out to the nipple [38].

Fatty tissue also known as adipose tissue gives the breast shape and size. The majority of the breast contains adipose tissue. Three kinds of fats can be found in the woman breast. The fat that can be found directly under the skin is called subcutaneous fat. The fat that can be found surrounded by the lobes is called mammary layer. The fat found at the back of the breast, above the pectoral muscle layer, is called retro-mammary fat. Behind the retro-mammary fat are two major muscles, called pectoralis major and pectoralis minor which lies underneath the breast tissue.

Most breast cancers form initially in the ducts of the breast [39]. The stages of cancer range from stage 0 to stage IV. Stage 0: carcinoma in situ (also known as pre-cancerous); Stage I: smaller tumor approximately 2 cm with no lymph node involvement; Stage II: tumor size approximately 2-5 cm with/without nodal involvement; Stage III: tumor that has invaded the chest wall without metastasis; Stage IV: any size of tumor and nodal involvement as well as distant metastasis [40]. Earlier detection is generally at stage 0 to II, although aggressive cancers can advance rapidly in the interim between early screening tests.

1.2 Stage-0 breast cancer

Stage-0 are a non-invasive cancers. The two most common types of pre-cancers are Ductal carcinoma in situ (DCIS) and Lobular carcinoma in situ (LCIS). In DCIS, abnormal cells stay

within the milk ducts, where LCIS is a condition in which abnormal cells are found in the lobules of the breast, as shown in Figure 1.1. As noted, most breast cancers initially form in the ducts of the breast.

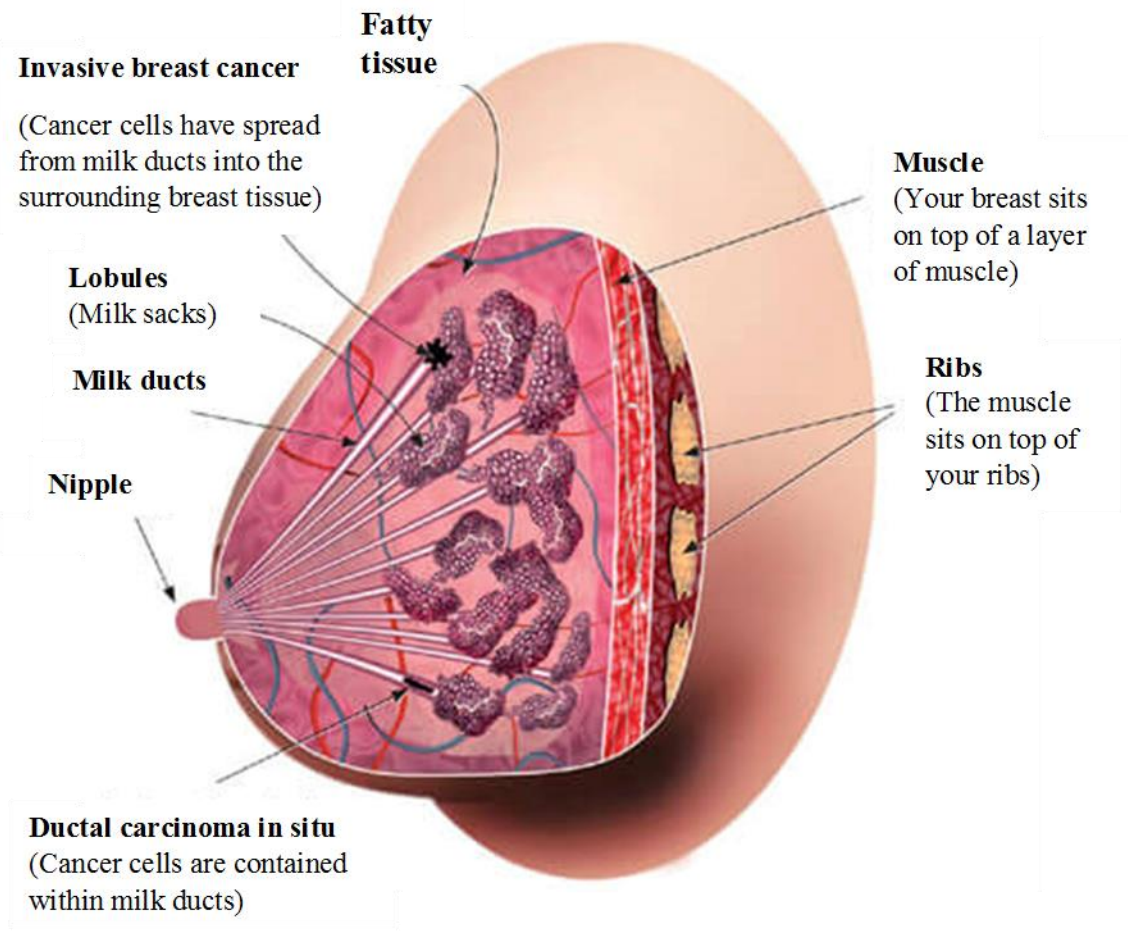

Figure 1.1: DCIS and LCIS abnormal cells [41]

DCIS and LCIS may increase the risk of developing invasive cancer, which is the next stage. When the disease is confined to the ducts it is called “intraductal cancer”. These types of cancers do not have the potential of spreading and are curable. Some carcinoma in situ lesions are believed to rapidly transit to invasive, while others remain unchanged [42]. Currently, it is not possible to predict accurately which carcinoma in situ would be more

likely to progress to invasive breast cancer, but up to 40% of lesions progress to invasive if untreated [43].

When the cancer cells break out of the duct, the cancer becomes an "infiltrating ductal carcinoma". At this time, the cancer cells may gain access to the lymphatic spaces and blood vessels in the breast. In the last stage of breast cancer IV, distant or metastatic cancer, it has spread to distant organs, such as the brain, lung, or liver [44].

1.3 Significance of this research

Among women, breast cancer is the most common type of cancer. Millions of women diagnosed with breast cancer and many of them die every year worldwide. It is the second leading cause of cancer deaths in women. Research has shown early detection, combined with effective treatment, can reduce mortality [23].

A number of screening tests have been employed, but these methods have limitations, such as unacceptable rates of false positive and false negative results, contribute to harm, and have limitations in age due to exposure to ionizing radiation. They also require qualified radiologists, and/or expensive technicians and equipment, which raises cost. Thus, there is a need for a better screening method. The work of this PhD aims to contribute to the development of a novel method for breast cancer screening using surface motion tracking of the skin. These motions can be used to infer the composition of the internal structure of the breast, where stiffer cancerous tissues have significant contrast to surrounding healthy tissues. However, there are still hurdles to the development of this technology.

Digital imaged elasto-tomography (DIET) is a low cost, radiation-free, non-invasive breast cancer screening technique. It analyses local tissue stiffness based on elastographic reconstruction and/or estimation of underlying tissue stiffness [23, 25-28]. In particular, DIET captures steady state surface motion in response to 16 – 50 Hz low amplitude sinusoidal mechanical actuation applied to the breast [31], and can use a range of methods to identify regions of high underlying stiffness, leveraging the high contrast between healthy and cancerous tissues [28].

DIET technology is not yet suitable for a large randomized clinical trial. In particular, there are issues concerning its speed of development that could be addressed by a series of tools to enhance the speed and repeatability of DIET technology development. Currently, DIET is developed largely based on clinical testing of human volunteers in pilot clinical trials, leading to a build and test approach, which is slow and not necessarily optimal as many volunteers have been recently diagnosed with cancer and thus their tests cannot be repeated when technology improves.

Three main areas where this productivity could be enhanced include: a) development of realistic, accurate tissue mimicking breast phantoms; b) validation of the surface measurement algorithms to quantify their error and thus to quantify the limits of diagnostic algorithms; and c) development of finite element models to accurately mimic breast phantoms to avoid repeated phantom experiments. Such a set of tools would allow much more rapid and optimal development of diagnostic metrics, as well as for developing optimised surface motion measurement algorithms. They would allow finite element models to generate data the same as that for realistic phantoms, allowing a rapid test cycle of many possible inclusion locations and sizes. From those results, a limited experimental series using

phantoms could be run to validate these results or optimize them further. Finally, when ready, clinical testing on human volunteers could be undertaken with far greater confidence of success.

This thesis thus addresses these three areas. It develops tools for each of them, and validates the current optical flow algorithm used to obtain surface motion measurements [46]. Together they offer a potentially far faster and more optimal development process.

1.4 Preface

The thesis is organized as follows:

Chapter 2: Background and literature review. This chapter provides an overview of the working principles, benefits, limitations, performance, and cost of current breast cancer detection techniques. It is based on an extensive literature review focusing on published works reporting the main performance, cost, and comfort/compliance metrics considered. Due to limitations and drawbacks of existing breast cancer screening methods there is a need for better screening methods. Emerging, non-invasive methods offer promise to mitigate the issues particularly around comfort/pain and radiation dose, which would improve compliance and enable all ages to be screened regularly.

Chapter 3: Mechanical behavior of tissue mimicking breast phantom materials. In this chapter, the mechanical properties of three different materials used to emulate the mechanical behavior of real breast tissue are measured: agar, gelatin, and silicone, to assess their suitability for use in phantoms in systems assessing tissue mechanics for diagnostics.

Chapter 4: Finite element modelling of breast shaped phantom. In this chapter, three different phantoms were modelled: healthy, with 10 mm and 20 mm inclusions. The overall goal is to create models with enough accuracy to replace experimental phantoms in providing data to optimize diagnostic algorithms for digital imaged elasto-tomography (DIET) screening technologies.

Chapter 5: Validation of finite element modelling with DIET experimental data of breast shaped phantom. In this chapter, validation of FE model results with experimental DIET phantom data uses cross correlation coefficients between experimental simulated data, and direct comparison for over 4000 collected points on each model and phantom.

Chapter 6: Laser Doppler vibrometer validation of an optical flow motion tracking algorithm. The focus of this chapter is to validate recorded peak of horizontal displacement of DIET experimental data and laser Doppler vibrometer data at frequencies of 16Hz, 24Hz, 32Hz, and 40Hz on the breast shaped phantom with and without 10 mm and 20 mm stiffer inclusions.

Chapter 7: Finite element modelling for different sizes of inclusion at different positions. In this chapter the same modelling procedure were followed from chapter 4 and 5. Total 6 phantoms were modelled with 10 mm and 20 mm at three different positions at frequencies of 16 Hz, 24 Hz, 32 Hz, and 40 Hz.

Chapter 8: Conclusions. This chapter concludes the research results and main content of this thesis.

Chapter 9: Future work. This chapter discusses potential future work.

Chapter 2: Background and literature review

Early detection of breast cancer, combined with effective treatment, can reduce mortality. Millions of women are diagnosed with breast cancer and many die every year globally. Numerous early detection screening tests have been tested and employed. A wide range of current breast cancer screening methods are reviewed based on a series of searches focused on clinical testing and performance. The key factors evaluated centre around the trade-offs between accuracy (sensitivity and specificity), operator dependence of results, invasiveness, comfort, time required, and cost. All of these factors affect the quality of the screen, access/eligibility, and/or compliance to screening programs by eligible women.

This chapter thus provides an overview of current breast cancer detection techniques in light of cost, invasiveness and comfort/compliance metrics. All these issue play a role in the quality and compliance of screening, and thus efficacy of screening programs. Finally, it thus sets the context and stage for the research in this thesis.

2.1 Current methods of screening for breast cancer

2.1.1 Mammography

Over the years, X-ray mammography (XM) has become the primary, non-self-exam screening technique for breast cancer [7, 45]. Mammography forms images of breast density by passing X-rays through the tissue as shown in Figure 2.1. However, exposure to this

ionising radiation may be harmful and possibly cause cancer itself [46]. Risk is one of the reasons it is not recommended for screening in women under a minimum of 40 years [47], and is typically reserved for women over 45-50 years.

Mammography can provide benefit to women aged 40 to 49 years. Mortality rates at these ages can be reduced up to 15% after 14 years of follow up [48]. However, women who started screening every second year at age 50, until 69 years of age, have shown more benefit with less harm [49, 50], and thus this age range and interval are more commonly used in national screening programs. Due to the extensive validation and use, mammography is the most widely used and well-accepted imaging modality for breast screening [51].

However, mammography has also been criticized for a number of reasons. Thornton and colleagues listed physical, emotional, social, financial, and/or psychological harm caused by mammograms [52]. Additionally, to get the best possible images, the breast tissue must be squeezed between two plates as the image is taken [53]. Many women found this compression painful and uncomfortable [54]. Several women experienced enough pain that it affected their decision to attend another examination [55-59], reducing compliance and thus the likelihood of early detection.

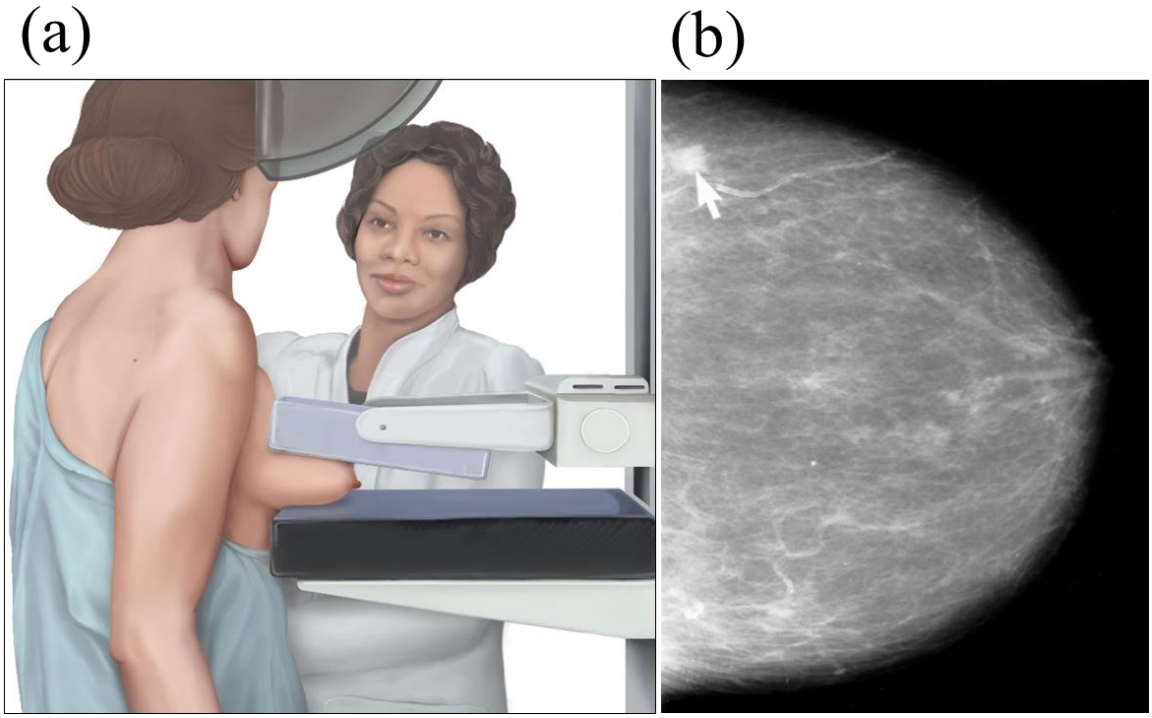

Figure 2.1: (a) Mammogram Equipment (National Cancer Institute by Alan Hoofring, 2003), (b) Mammogram showing a small cancerous lesion as well as calcific deposits in veins (National Cancer Institute, March 1991)

Mammographic breast density is a strong predictor of breast cancer [60-63]. However, denser tissue is harder to compress, reducing image quality and detection potential. Younger women naturally have denser breast tissue and it can be difficult to detect cancer with mammography [64]. All of these issues can lead to misdiagnosis and increased false positive/negative rates [65].

Mammography with adjunctive ultrasonography results in higher rates of cancer detection in younger women or those with dense breast tissues, but also increases the number of false positive results [66]. The Japan Strategic Anti-cancer Randomized Trial (J-START) investigated sensitivity and specificity with 36,000 women in each group (XM and XM+US) and about 180 cancers per group. Sensitivity rises to 90% with added ultrasound but

specificity drops to 87%. Thus, positive predictive value is likely poor given low incidence rates [67].

Mammography is highly dependent on equipment, operator, radiologist, and breast density. False-negative rates for mammography range from 4% to 34% [68-72]. Table 2.1 provides a summary of published performance results for mammography. Research has shown that the sensitivity of mammography for detecting multiple malignant foci is often less than 50% [46, 73, 74]. Due to radiation exposure and false positive results, both patients and physicians are concerned about using mammography to screen women under 45 years [75]. These limitations have this caused many unnecessary biopsies due to the low specificity of mammography [76].

Finally, and more positively, mammography has been proven and established in terms of its detection of ductal carcinoma in situ (DCIS) [77]. It is also established in terms of potentially differentiating the micro-calcifications that can occur in breast tissue from cancerous lesions. However, as noted, these difficult cases are also a function of operator and radiologist experience and capability, even though the physics of the modality enables their detection, differentiation and diagnosis.

The financial costs of breast cancer are high. Several studies show breast cancer screening for women aged 50-70 years is cost-effective and costs range between $13,200 and $28,000 per year of life saved [78-82]. In New Zealand, a mammogram costs approximately $180 [83]. However, for women below 45 years the number of false positives and cost for extra examinations, unnecessary biopsies, and other effects, means it is not cost effective [84-86]. For all these reasons, continuous efforts have been made by researchers to explore alternative

imaging modalities for breast cancer screening and diagnosis, particularly those suited to younger women or those with dense breast tissue, with reduced total costs a further goal.

Mammography usually takes only one picture, across the entire breast, in each of two directions: top to bottom and side to side. Digital breast tomosynthesis is a technique that creates a 3-dimensional picture of the breast to improve breast cancer detection especially with dense breast [87, 88]. Digital breast tomosynthesis has improved on the limitations of traditional digital mammography by increasing cancer detection and decreasing false-positive examinations [89]. Additionally, a digital breast tomosynthesis can reduce the pain and discomfort arising from compressing breast between two plates while performing a mammogram. For these reasons digital breast tomosynthesis can replace traditional mammogram in breast cancer screening [90]. The major disadvantage of digital breast tomosynthesis is prolonged time and more radiation exposure at twice that of standard mammography. Even though it reduces the need for repeat mammographic images and the increased dose from those tests, this added radiation is seen as excessive. In addition, it leads to increased recommendations for biopsies, increasing detection, but also cost when cancer is not present due to increased false positives [91].

Overall, it is still important to note that mammography is still the only proven and accepted wide scale screening modality.

2.1.2 Magnetic Resonance Imaging

Magnetic resonance imaging (MRI) has been progressively integrated into breast imaging and is used to detect lesions [92]. A magnetic field is created to align all the protons in the body in a single direction. Radio waves are sent from a scanner to perturb this alignment. As

the protons realign, they emit radio waves which used to determine the molecule type and location. These radio signals are analysed and converted into an image [93]. When applied to soft tissue, MRI can be used to generate highly detailed images of the internal structure of the breast. MRI signal strength, and thus image contrast, is determined by the density of hydrogen protons within the imaged tissue and their response to rapidly changing radio waves and magnetic fields. The image contrast of MRI systems can be significantly enhanced using a range of chemicals ingested or injected prior to the scan [94]. Figure 2.2 illustrates this modality.

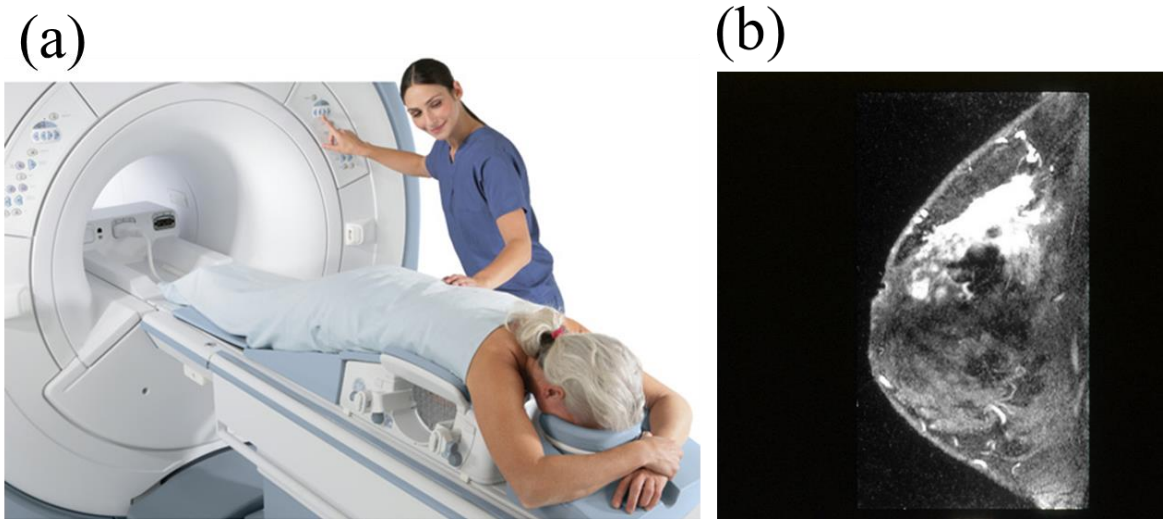

Figure 2.2: (a) MRI Equipment, (b) MRI of individual breast, demonstrating marked enhancement (bright area) which was confirmed to be cancer (National Cancer Institute, February 1994)

MRI can provide superior imaging results and outcomes compared to mammography and other breast screening techniques for women at high risk of breast cancer [95, 96]. MRI is a sophisticated imaging method without the need for ionizing radiation and therefore does not increase the risk of cancers [97]. Women with dense breasts are also considered at high risk,

and for this cohort annual MRI is recommended first for screening with further validation of the outcome [98].

However, there are many unresolved issues in using MRI for breast cancer screening, including lack of standardised techniques and interpretation criteria [99]. In 2013, Sutcliffe Iii and his colleague published an article which reiterated the issues with MRI and noted that the different levels of training and experience of the radiologist result in significant variation in MRI findings of benign and malignant tumours [100]. Other limitations mentioned in past studies have also suggested MRI is less reliable in the detection of ductal carcinoma in situ (DCIS) because it is unable to image calcifications, tiny calcium deposits that can indicate breast cancer [14].

The U.S. Food and Drug Administration (FDA) approved MRI in 1991 to help diagnose breast cancer. However, because of its high sensitivity and lower specificity which can lead to false positives, the American Cancer Society does not recommend MRI for all women [101, 102]. The range of specificity varies from 37% to 100% [103-107] and this low specificity leads to more false positives and unnecessary biopsies [108]. These outcomes are summarised in Table 2.1.

To improve specificity, recommendations for breast MRI state dynamic contrast enhanced (DCE) acquisition should be obtained [109]. The most widely used form of DCE-MRI analysis is the assessment of the type of time-signal intensity curve. The shape of the time-signal intensity curve is an important criterion in differentiating benign and malignant enhancing lesions [110]. To further improve lesion classification, a high-resolution T2 sequence and diffusion-weighted sequences have been added to the state-of-art MRI protocol

[109, 111, 112]. However, these changes make breast MRI time-consuming, with report investigation times between 20 and 40 min [113], and significantly increase cost, as well.

More specifically, the cost of MRI is approximately ten times the cost of mammography [47]. Since the current cost of mammography is one factor leading to limited mammogram prescription and use, this added cost is not sustainable for wide scale screening. MRI cost with screening and treatment is estimated at $123 672 per detected breast cancer [114], which is ten times higher than mammography. In addition to the high cost, results take more time to produce [115, 116], and there is a lack of standardization in terms of technique, as well as interpretation guidelines [100]. Thus, its screening use is limited and relatively very costly.

2.1.3 Ultrasound

Ultrasound sends high frequency sound energy into the tissue from a hand-held transducer. This sound is reflected by boundaries between tissue where the acoustic impedance changes. Reflected sound is received by the transducer and the depth of reflection can be determined by 'time of flight'. Depth and detection information is combined into an image of cancerous tissue, as it has different density to surroundings tissue. This modality is illustrated in Figure 2.3.

Ultrasound is currently used to differentiate breast masses [117], and guide aspirations and biopsies [118]. Studies report ultrasound as a useful adjunct to mammography, and that in this role it yields improved cancer detection [119-121]. However, it is not recommended as a screening tool, in part because it is more specifically useful in clinical use for assessing whether a lump is fluid filled or solid [122].

Current technological advances in ultrasound equipment include very high-frequency 15MHz and multi-array transducers, as well as matrix broadband transducers. These transducers provide high levels of spatial and contrast resolution theoretically allowing detection of breast carcinomas as small as a few millimetres. To yield the highest spatial resolution, all modern transducers should be operated at the highest clinically appropriate frequency. However, high resolution ultrasound equipment can be much more expensive that traditional machines. In addition, there is a limitation that no high frequency probe can image deeper than 4 cm and this limitation should be kept in mind when evaluating large breasts or deeper situated lesions, as the operator may have to switch to a lower-frequency probe to achieve better penetration and a wider field of view with concomitant loss of resolution [123].

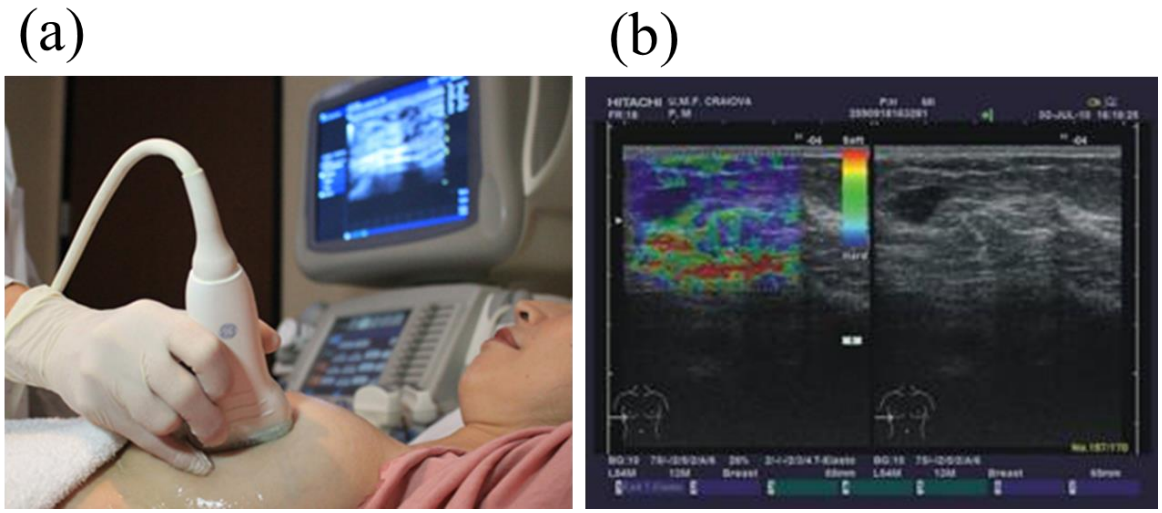

Figure 2.3: (a) US Equipment, (b) Ultrasound elastography of ductal invasive carcinoma in a 51 year old patient with blue elastic appearance and desmoplastic reaction [51]

Similar to Mammography and MRI, ultrasound also has limitations. It too requires a well-trained, skilled operator and a follow up team that includes radiologists, breast surgeons, pathologists, and expert physician input to interpret images [124]. Screening takes 15min or longer for each breast and it takes additional time for radiologists or physicians to review the

images manually. Each of these aspects introduces subjectivity and error based on experience, as well as added cost.

Costs for ultrasound screening include review by radiologists, technician time, and communicating results to the doctors. The average cost per patient has been estimated at €127 (US $ 115) [125], but may vary by country. Hence, it is almost similar to mammography in cost, but with other limitations.

Even at high frequencies, ultrasound has relatively low spatial resolution, low specificity [126], and is unable to image micro calcifications [127], especially when they are inside fibroglandular breast tissues [128-130]. These factors all increase the rate of false positive and false negative results [131, 132]. Table 2.1 summarizes the reported performance of ultrasound in breast cancer screening. The performance, particularly the percentages range of false positive rate (FPR) and false negative rate (FNR) are higher than for other modalities, limiting its efficacy in widespread screening or pre-screening, and increasing its cost per cancer detected.

2.1.4 Thermography

Thermography (TG) was one of the earliest breast cancer screening techniques to be developed [133]. Lawson published the first breast thermogram in 1957 [134-136]. Thermography is a non-contact imaging technique widely used in biomedical research [137-139], including breast cancer detection [127, 140]. The modality is illustrated in Figure 2.4.

Anybody with a temperature above absolute zero emits infrared radiation, where the wave length of light depends on the temperature [141]. Thermography captures only infrared

radiation from the skin, and is completely non-invasive and non-contact [142]. Temperatures of the skin over a tumour are reported to be significantly higher than normal skin temperature due to increased blood flow [133]. The particular temperature and humidity for thermal images used in this application are thus critical and range from 20 to 25 ^{o}C and 40 to 60%, respectively [143]. Unlike mammography, there is no radiation risk in thermography and it is thus suitable for screening at any age [144].

However, this technique also has no standard examination procedure [145, 146], and is very environment dependant [147, 148]. Thus, before a test it is recommended that patients should rest for at least 15min to reduce basal metabolic rate and temperature changes [149]. Another difficulty of thermography screening is to localise the exact tumour position. All of these factors lead to a high level of variability in test quality and efficacy, as well as increased sensitivity to operator skill and experience [150].

The performance of thermography, as reported by several authors, is summarised in Table 2.1. A high rate of false positives limits thermography as a screening tool for breast cancer. Studies show that most false negative results were microcalcifications, meaning that this screening tool is unreliable for detecting these abnormalities [151]. In addition, the cost of this equipment is high and also requires a large temperature controlled area, which is also costly.

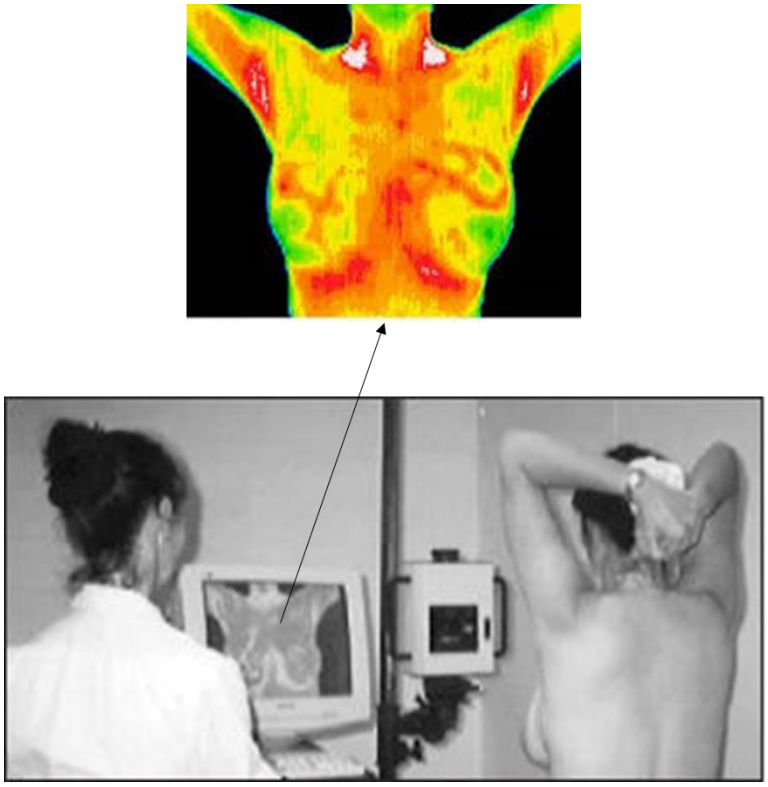

Figure 2.4: Thermography equipment which shows body temperature

Overall, the method was dismissed in the late 1970's due to a very high percentage of false detections resulting from inadequate imaging procedures and the lack of high resolution thermal imaging equipment at the time. In addition, after 1977, researchers found other screening modalities provided better results than thermography. Therefore, the medical community lost interest in this modality [152].

2.1.5 Microwave Imaging

Microwave imaging (MI) is based on the dielectric properties of tissues. This imaging technique is applicable to breast cancer detection, due to the differences in dielectric properties between normal and malignant breast tissues [153-156]. There are three types of microwave: passive, hybrid, and active.

Passive microwave relies on tumour temperature and detects regions of increased temperature in the breast [157-159]. The key concept of passive microwave imaging is similar to thermography with a different spectrum range [160]. Hybrid microwave imaging methods heat tumours with microwaves and form images using an ultrasound transducer to detect pressure waves generated by the expansion of heated tissues [161]. Active microwave imaging techniques are classified as radar or tomographic methods. In both active and passive approaches, scattered microwave signals are measured after transmitting low-power microwave signals into the breast using an array of 16 antennas attached in a circular fashion. Each antenna in turn transmits electromagnetic waves in the microwave spectrum and the remaining 15 antennas collect measured data [156, 162].

In the tomographic approach, narrowband signals are used to record a set of scattering parameters for the breast. An inversion algorithm is used to reconstruct a complete map of the dielectric properties of the breast [163, 164]. In contrast, radar methods use wideband or ultra-wide band (UWB) signals to create images indicating the presence and location of significant scattering objects [165].

Active microwave imaging techniques are totally dependent on the dielectric properties: permittivity and conductivity. It is reported that dielectric properties for cancerous tissues are three or more times greater than healthy tissues providing potentially goal contrast for detection [166]. Radar-based approaches have only involved testing with phantoms [167, 168] and early-stage clinical investigations [169]. There are thus few reports on clinical trials that reflect the significant technical challenges involved in sensor design and implementation, measurement hardware, and the development of patient interfaces [165].

Unlike mammography, this technique is free from ionizing radiation, non-invasive, requires no breast compression, and is less expensive than MRI [170]. The major hurdles limiting patient use are both at the hardware level due to challenges in collecting accurate and no corrupted data, and software level, where they are often plagued by unrealistic reconstruction times in the tens of hours. Resolution of the image is also limited to 0.5cm and 1.0 cm in healthy and denser breast, respectively, which limits overall and early detection [156]. Hence, these modalities are not yet ready for application.

2.1.6 Elastography

Elastography (E) is a medical imaging technique to examine elastic properties of breast tissues, and this technique may be useful to distinguish malignant and benign masses [171]. In elastography, static and dynamic are two methods to examine mechanical properties [172, 173]. Based on viscoelastic behaviour of breast tissues, echo signals are obtained before and after compression from tissues and then converted to displacement distribution images. From measured displacement, elastography is able to provide tissue stiffness information [174].

Elastography is currently the most widely method used in clinic. In various organs, such as the breast, prostate, and thyroid, elastography has proven highly accurate in the evaluation of cancerous tissues [175, 176]. Ultra-sonographic (US) elastography was introduced to overcome limitations of ultrasound and mammography alone, where it combines US technology and the basic principles of elastography [177, 178].

The combination of ultrasound elastography and sonography had the best results in detecting cancer with an average 89.7% sensitivity and 95.7% specificity. Due to the lowest false-negative rates elastography is a promising technique and has the potential to reduce

unnecessary breast biopsies [179]. The performance of elastography reported by several authors is summarised in Table 2.1.

Elastography potentially is lower cost than MRI [180]. Some lesions may contain benign and malignant, elastography can be helpful working with complicated breast lesions. Additionally, elastography reduces unnecessary biopsies costs [181]. However, elastography is expensive, time consuming, and error prone reconstruction inverse problems is a major issue preventing its wider use [26, 182].

2.1.6.1 Digital Imaged Elasto-Tomography

The fundamental concept of DIET (digital imaged elasto tomography) is based on elastography and was first published in 2004 [25]. DIET is non-invasive, portable, inexpensive, comfortable breast cancer screening technique that measures the stiffness of tissue within the breast [27, 30, 36]. Its goal is to maximize the advantage of elastography, while removing its limitations.

The DIET system consists of 5 digital cameras and synchronised strobe lights that capture low amplitude surface oscillations in the range 16 – 50 Hz generated by mechanical actuation applied to the breast [36]. The DIET approach consists of the steps summarised in Figure 2.5. Several images are captured during one cycle of a typical frequency, all at different phase angles relative to the input motion, as shown in Figure 2.6. To avoid the need for expensive high frame rate cameras and to reduce the impact of motion on image quality, a strobe lighting system is used in conjunction with the cameras [35, 183]. Areas of higher stiffness enforce a different surface response that can be detected to identify and locate a tumour [27].

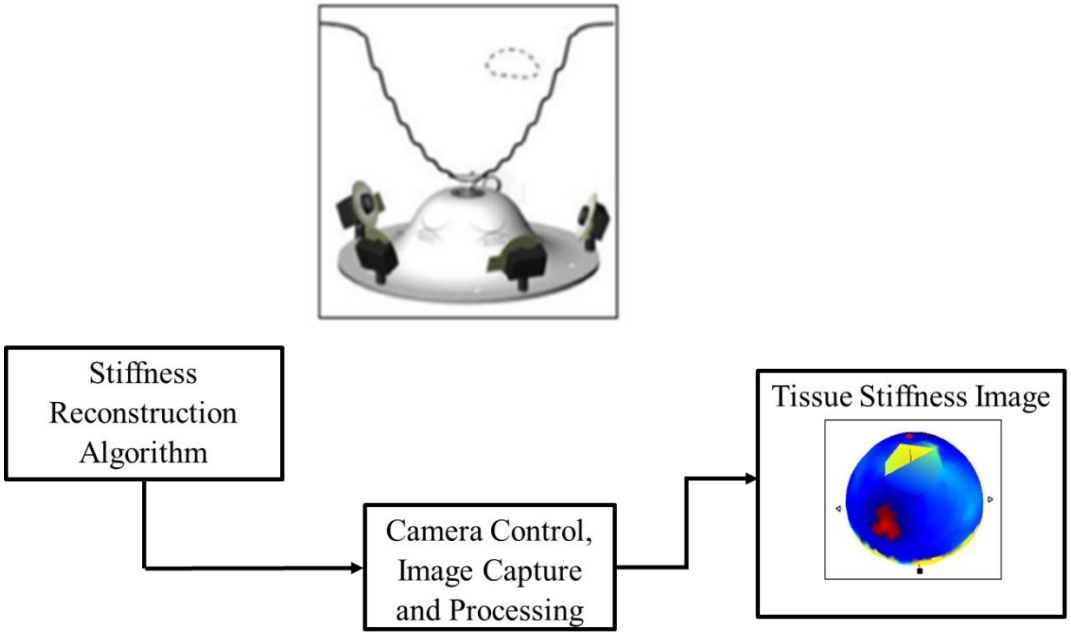

Figure 2.5: Concept of DIET

To reconstruct skin surface motion, an optical flow algorithm is applied to pairs of frames. A 3D model of the breast surface is also computed and combined with the optical flow data to give the 3D motion of the surface of the breast [36]. The motion is then analysed in a variety of objective algorithm based ways to detect stiffness differences and tumours [27, 28, 184].

A silicone-based hydrogel phantom was used during developmental testing of DIET because of its linear elastic behaviour and similar mechanical properties to human soft tissue [184, 185]. During concept validation, DIET produced encouraging results [26, 32, 34, 186-188]. However, clinical results are limited to date.

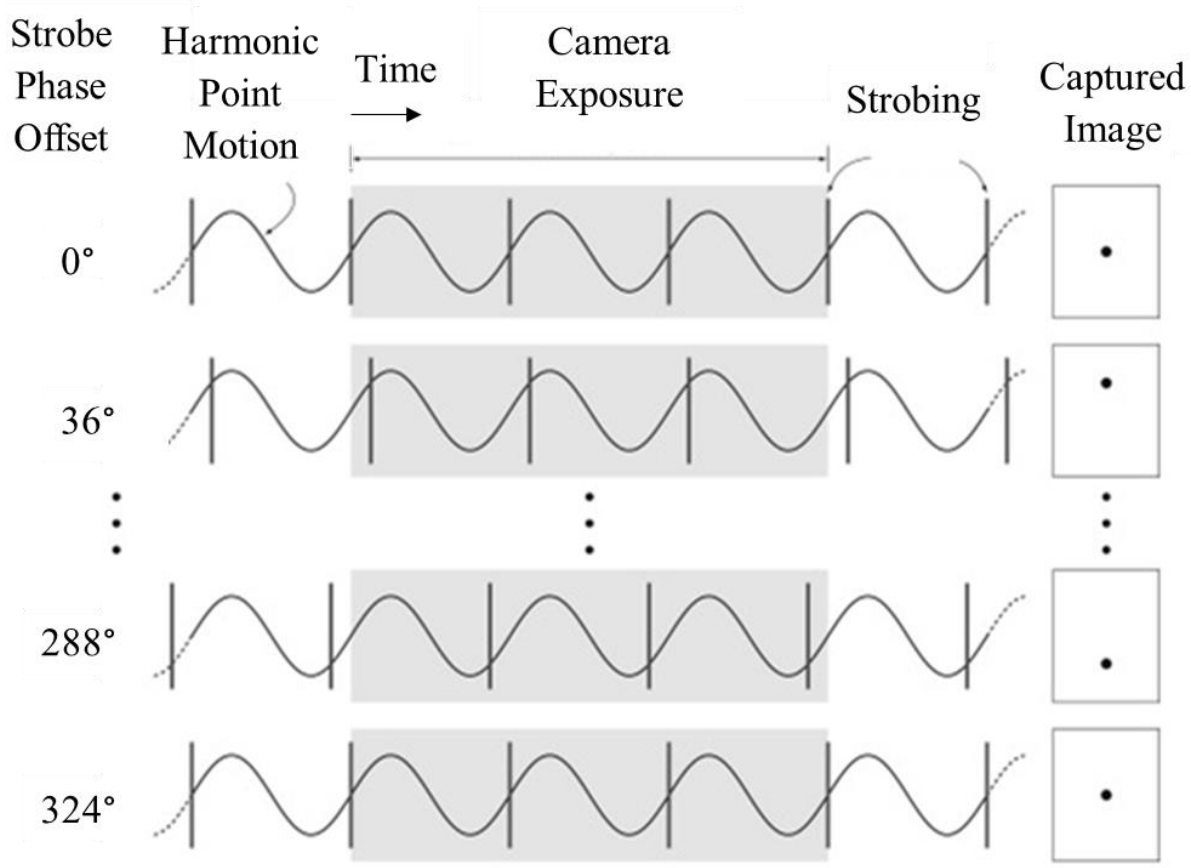

Figure 2.6: A schematic detail of timing of the image capture process

The main features are non-invasive, low cost, and fast. Phantom studies have shown the method is capable of detecting stiff inclusions that mimic cancer. Therefore, it could prove suitable for screening at any age. In addition, it is portable and requires no specialist user, reducing variability. All these factors, and its reliance on low cost digital imaging sensors, means its cost is relatively very low. It requires no special premises or personnel.

2.2 Summary

Tables 2.1 and 2.2 and Figure 2.7 provide an overview of all modalities concerning advantages and disadvantages, such as economic, speed, accuracy, operator independency, risk, and comfort. In particular, the diagram of Figure 2.6 provides an overview of how each

modality interacts in terms of the key features considered. The results summarised here, particularly in Table 2.1 and Table 2.2, clearly show the advantages of the current standard, mammography, in performance, but also its disadvantages in regards to its invasive nature, as well as its wide variability in diagnostic performance. Equally, the results show the potential of emerging modalities, such as ultrasound and elastography, assuming they can overcome specific limitations they face in performance and/or lack of significant clinical data and testing.

Table 2.1: Summary of performance results of every modality

Techniques	Authors	TPR (%)	FNR (%)		TNR (%)	FPR (%)	Patients (#Pos / #Neg)
Mammography	Kuhl et al. [189]	33.0	67.0		93.0	7.0	(9 / 96)
	Dodd [190]	87.2	12.8		85.1	14.9	(3661 / 4051)
	Kolb et al. [191]	77.6	22.4		98.8	1.2	(246 / 27579)
	Manoliu and Ooms [192]	86.6	13.4		80.7	19.3	(279 / 376)
	Ohlinger et al. [193]	100.0	0.0		72.7	27.3	(3 / 11)
	Habib et al. [194]	72.2	27.8		75.0	25.0	(18 / 8)
	Standertskjöld-Nordenstam and Svinhufvud [195]	91.8	8.2		95.6	4.4	NA
	Luczyńska et al. [196]	91.0	9.0		15.0	85.0	(114 / 59)
	Burman et al. [66]	97.8	2.2		83.9	16.1	(47 / 5059)
	Egan and Egan [197]	77.4	22.6		67.4	32.6	(31 / 46)
MRI	Langer et al. [108]	91.6	8.4		70.4	29.6	(36 / 108)
	Spick et al. [198]	100.0	0.0		88.5	11.5	(15 / 96)

	Kuhl et al. [189]	100.0	0.0		95.0	5.0	(9 / 96)
	Heinisch et al. [199]	92.0	8.0		73.3	26.7	(25 / 15)
	Hayashi et al. [200]	43.8	56.2		90.3	9.7	(98 / 166)
	Belli et al. [201]	90.2	9.8		100.0	0.0	(41 / 4)
Ultrasound	Kolb et al. [191]	75.3	24.7		96.8	3.2	(146 / 13,401)
	Egan and Egan [197]	67.7	32.3		93.5	6.5	(31 / 46)
	Satake et al. [202]	89.6	10.4		76.5	23.5	(29 / 17)
	Lumachi et al. [203]	67.5	32.5		80.0	20.0	(37 / 40)
	Stavros et al. [204]	98.4	1.6		67.8	32.2	(125 / 625)
	Ohlinger et al. [193]	100.0	0.0		54.5	45.5	(3 / 11)
	Kuhl et al. [189]	33.0	67.0		80.0	20.0	(9 / 96)
	Habib et al. [194]	94.4	5.6		70.0	30.0	(18 / 10)
	Chang et al. [205]	95.5	4.5		91.4	8.6	(110 / 140)
	Chang et al. [206]	95.5	4.5		77.8	22.2	(110 / 140)
Thermography	Tang et al. [207]	93.6	6.4		44.3	55.7	(47 / 70)
	Ovechkin and Yoon [208]	95.4	4.6		88.0	12.0	(22 / 25)
	Collett et al. [209]	62.1	37.9		68.8	31.2	(66 / 144)
	Kontos et al. [210]	25.0	75.0		84.9	15.1	(20 / 106)
	Borchartt et al. [211]	95.8	4.2		25.0	75.0	(24 / 4)
	FARRELL et al. [212]	87.0	13.0		90.0	10.0	NA
Elastography	Giuseppetti [213]	79	21		89	79	NA
	Thomas [175]	82	18		87	13	(300 / 0)
	Evans [176]	97	3		83	17	(53 / 0)

TPR = True Positive Rate (Sensitivity), TNR = True Negative Rate (Specificity), FNR= False Negative Rate, FPR = False Positive Rate, NA=Not available

Table 2.2: All modalities in terms of main aspects

Techniques	Economic	Fast	Accurate	Operator Independent	Ionizing Radiation	Comfort
Elastography	✓	✓	✓	✓	×	✓
X-ray Mammography	✓	✓	×	×	✓	×
MRI	×	✓	✓	×	×	✓
Ultrasound	✓	✓	×	×	×	✓
Microwave Imaging	✓	×	✓	×	×	✓

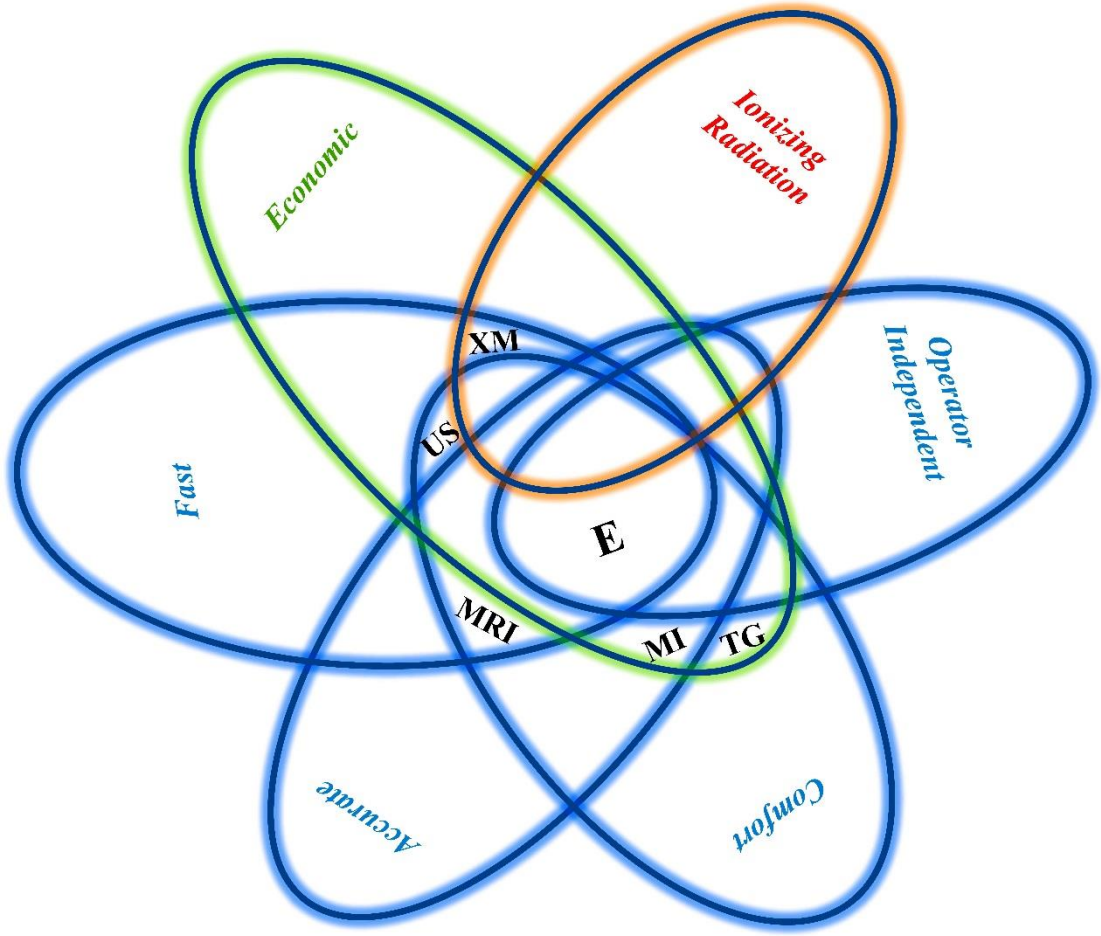

Figure 2.7: All modalities in terms of main aspects, where blue (Fast, Operator Independent and Accurate) and green (Economic) are desirable aspects, and red (Invasive) is undesirable. The diagram shows the relative location of all major modalities considered where the goal is to be in all blue and green circles and avoiding the red. The diagram is also captured in Table 2.2.

Outside of breast self-exam, mammography is the most widely used and well-accepted technique to detect breast cancer, and is thus an effective gold standard in the field. However, its limitations in exposure to ionizing radiation and comfort due to breast compression, both of which can affect compliance to screening, create a significant need for other less invasive approaches. In addition, its variability in diagnosis based on radiologist experience may be a further limitation to be improved by automated methods, within mammography or via another modality. However, it is important to note that mammography is still the only proven and accepted wide scale screening modality.

In contrast, current and emerging methods using ultrasound, thermography, MRI, and Microwave imaging all are non-invasive, but their reported results to date are too variable at this time for use in regular screening. Newer emerging technologies, like DIET and advanced ultrasound systems, can offer non-invasive, all age screening that is low cost. However, these latter emerging technologies still face a long validation process to prove their efficacy in relation to accepted standards before they are accepted as realistic screening alternatives and this thesis addresses some of validation process.

Overall, this review concisely summarises the overall strengths, weaknesses, and thus gaps in the field, with a strong focus on how newer, emerging technologies can offer novel solutions to broader cohorts.

Chapter 3: Mechanical behaviour of tissue mimicking breast phantom materials

Understanding the mechanical properties of soft tissues, particularly stiffness, is relevant for the diagnosis of many illnesses, such as liver, heart disease and breast cancer. The aim of this chapter is to determine which materials and compositions have appropriate elastic modulus and viscoelastic properties to accurately mimic the actual breast tissues for DIET over its frequency range (up to 100Hz) of inputs. Phantoms are an important aspect of diagnosis development and have not been properly investigated over the full range in past.

To investigate the linear elastic properties of tissues, linear stress strain characteristics of agar, gelatin and silicone samples are studied by measuring small strains up to 5%. In this range, the phantom is assumed to exhibit linear elastic behaviour. Using Hooke's law, the elastic behaviour of phantoms can be characterized by its Young's modulus, and particularly its specific storage and loss moduli. More specifically, the viscoelastic behaviour of each material sample is investigated by subjecting the samples by varying dynamic input frequencies to assess the storage ($E^{'}$) and loss modulus ($E^{''}$), and thus elastic modulus of these materials using two proven measurement methods.

Different compositions of each material are used to approximate breast tissues, as well as to determine hyper-elastic model parameters of selected materials with appropriate elastic modulii. This work also examines the effect of preload on strain level on each sample and composition, with results compared to real tissue results for the ratio between healthy and inclusion tissues at 0.1Hz input frequency. Finally, the chapter comments on the reliability

and repeatability of these materials, particularly with respect to environmental conditions and storage. The fabrication process of breast shaped mimicking phantom of selected material is presented for completeness and repeatability.

3.1 Introduction

Demand for better screening modalities has driven growing interest in phantom materials to mimic breast tissue to aid research and design. A tissue-mimicking phantom should emulate important mechanical or radiological properties of biological tissue for the purpose of providing a more clinically realistic imaging test environment. These phantoms in-turn aid development and validation of new imaging techniques, such as elastography [26, 27, 36], which have different phantom requirements than non-contact imaging methods, such as MRI. Thus, the phantoms used may well be different and may, or may not, be multi-modality capable

A multitude of tissue-mimicking materials and phantoms are described in the literature, created using a variety of materials and preparation techniques for a range of biological systems. Mixtures of agar and gelatin, polyacrylamide gel, paraffin-gel waxes, polyvinyl chloride (PVC), and polyvinyl alcohol (PVA) were used in tissue phantoms for ultrasonography [214-222]. Both agar and gelatin have excellent acoustic properties for ultrasound (US) elastography and would be suitable for both MR and US properties [223]. Sinkus et al [224] describe a breast phantom for MRI elastography made from polyvinyl alcohol. The bulk of these phantoms consist of a softer material surrounding a 6-mm cube of harder material, which is a fine standard for non-contact imaging, such as MRI and US, as

well as for validating acoustic approaches. However, they are not representative in shape, which is important when mechanical wave propagation plays a role.

The DIET approach is mechanically based, and thus requires phantoms with mechanical properties to match tissue mechanical properties, as well as being created in a breast shape, as shape and location play a role in this diagnostic approach. Thus, most prior approaches would not be applicable in this more unique case, as well as making comparison difficult to prior phantoms due to differences in shape. Hence, this work focuses on the mechanical properties necessary for making a mechanical tissue mimicking phantom and does not have the scope to enable comparisons to other modalities.

Tissue stiffness has been recognised as playing an important role in diagnosis of breast cancer, as tumour tissues have greater stiffness than the surrounding breast tissues [225]. This difference is the foundation of manual palpation and breast self-exam, which is remarkably effective. Unfortunately, only a few studies reporting the elastic properties of real breast tissue are available in the literature. Studies on the mechanical behaviour of breast tissue show the elastic modulus (E) ratio of adipose to tumour tissue ranges from 1:5 to 1:15, which is a relatively large contrast to leverage in diagnosis.

Sarvazyan [226] found cancer can be 7 times stiffer than normal tissue. In contrast, Skovoroda [227] found a normal to tumour tissue ratio of 1:3. It is unclear what strain levels were used during these tests. Which will affect results significantly. Kroupkop [225] recognized the non-linear behaviour of breast tissues require the computation of an elastic modulus at more than one strain level. At 5% precompression strain, the ratio of normal to tumour tissue was 1:5, while at 20% precompression strain the ratio increased to 1:15. In

contrast, adipose and tumour tissues have similar elastic moduli at small strains (less than 10%). Thus, while it might not be possible to distinguish malignant tumours from benign tumours at small strain levels alone, it may be possible by considering data at larger strain. These results are used in this work to guide the experimental analysis and use of pre-load to delineate the targeted material properties when formulating phantoms using these materials. Hence, one result of this work relates the phantom creation process and materials used to the outcome material properties, relative to the desired tissue properties in breast cancer.

Several materials previously used to mimic breast tissues and their mechanical properties are close to those of breast tissue [228, 229]. Agar and agar/gelatin combinations have been commonly used to mimic the acoustic and elastic properties of soft tissues [215, 230-232]. Agar has also been used successfully to mimic organs, breast tissues, sinus cavities and vascular systems [230]. Agar, gelatin, and silicone are polymers with nonlinear behaviour and can provide similar stress-strain relationships to breast tissue [233]. Agar and gelatin are networks of polymer chains with covalent bonds and water filled interstitial space [234]. They thus mimic the physiology of fluid sense tissues well. Silicone is comprised of linear chains of dimethylsiloxane and is also used for a range of biomedical products [235]. Hence, given its ability to create materials with similar moduli, is a good phantom material candidate.

3.2 Materials and methods

To determine the elastic properties of agar, gelatin, and silicone, sample tests were conducted using a MTS Criterion model C43.104 (MTS Systems Corporation, USA). The dynamic viscoelastic properties of agar, gelatin, and silicone samples testing were conducted using a

Q800 Dynamic Mechanical Analysis (DMA) (TA Instruments, USA). Procedures for sample preparation and testing are described in the following sections.

3.2.1 Sample preparation

Three different "tissue equivalent" material samples were prepared for testing of mechanical properties. Each material is commercially available, but may require mixing. The key materials used were agar, gelatin, and silicone. Sample fabrication procedures were followed from published reports [184, 236, 237].

While the literature provides a range of formulations for similar tissues in these materials [238-240], they were varied here to better obtain the desired properties. In particular, for Agar, the amount of solution (n-propanol and deionized water) containing agar powder (concentration ranges from 2-6 g) is varied. For silicone, the composition is varied by changing the percentage of silicone used from 40-299 g. For gelatin, a bloom value of 125 is used instead of 200, as is used in most literature cases the authors are aware of [241, 242], which should provide more accurate outcome elastic moduli in this case.

Materials from each recipe were poured by injecting 10 ml of prepared solution into a cylindrical Perspex mould. When the samples cured, the bottom plate was carefully removed and unmould the samples with a uniform thickness and flat, smooth surfaces. Each material had three different recipes created to mimic skin, adipose, and much stiffer tumour tissue. The specific materials and constituent quantities are described in Table 3.1.

Sample sizes for the MTS compression tests were 30 mm diameter to fit pre-existing moulds and 12.5 mm thick to match the ASTM standard D 3767. For dynamic measurements,

samples were 30 mm in diameter and 5 mm thick for silicone and gelatin. However, 30 mm diameter and 1 mm thickness was used for agar to avoid sliding on the test system compression plate. These sample sizes are the recommended dimensions from the DMA system user manual [243]. Figure 3.1 shows some typical samples.

Table 3.1: Material quantities for mimicking different tissue

	Agar [237]	**Silicone [184]**	**Gelatin [236]**
Skin	Agar = 4 g n-propanol = 20 ml Deionized water = 97 ml	SoftGel A-341C = 55g	p-toluic acid = 0.294 g n-propanol = 28.69 ml Deionized water = 279.5 ml 125 Bloom gelatin = 35 g Formaldehyde (37% by weight) = 3.33 g Oil (50% Safflower + 50% Kerosene) = 98.6 ml Detergent = 5.86 ml
Adipose	Agar = 2 g n-propanol = 20 ml Deionized water = 97 ml	SoftGel A-341C = 192g DC 200 Silicone (50cst) = 299g	p-toluic acid = 0.133 g n-propanol = 6.96 ml Deionized water = 132.7 ml 125 Bloom gelatin = 10 g Formaldehyde (37% by weight) = 1.53 g Oil (50% Canola + 50% Kerosene) = 265.6 ml Detergent = 12 ml
Tumour	Agar = 6 g n-propanol = 20 ml Deionized water = 97 ml	A-341C = 40g LSR-05 A and B = 60g	p-toluic acid = 0.346 g n-propanol = 17 ml Deionized water =328 ml 125 Bloom gelatin = 100 g Formaldehyde (37% by weight) = 3.72 g Oil (50% Safflower + 50% Kerosene) = 38.4 ml Detergent = 2 ml

g = gram, ml = milli litre, percentage (%) = by weight, SoftGel A-341C (*Factor II, Inc., USA),* LSR-05 A and B (*Factor II, Inc., USA),* DC 200 Silicone *(Dow Corning Corporation, USA),* Agar *(Sigma-Aldrich, New Zealand),* n- propanol *(Fisher Chemical, USA),* p-toluic acid *(Sigma-Aldrich, New Zealand),* 125 Bloom geletin *(Sigma-Aldrich, New Zealand),* Formaldehyde *(Sigma-Aldrich, New Zealand),* Canola *(Pure Oil New Zealand Ltd, New Zealand),* Kerosene *(Sigma-Aldrich, New Zealand),* Detergent *(The Sun Products Corporation, USA)*

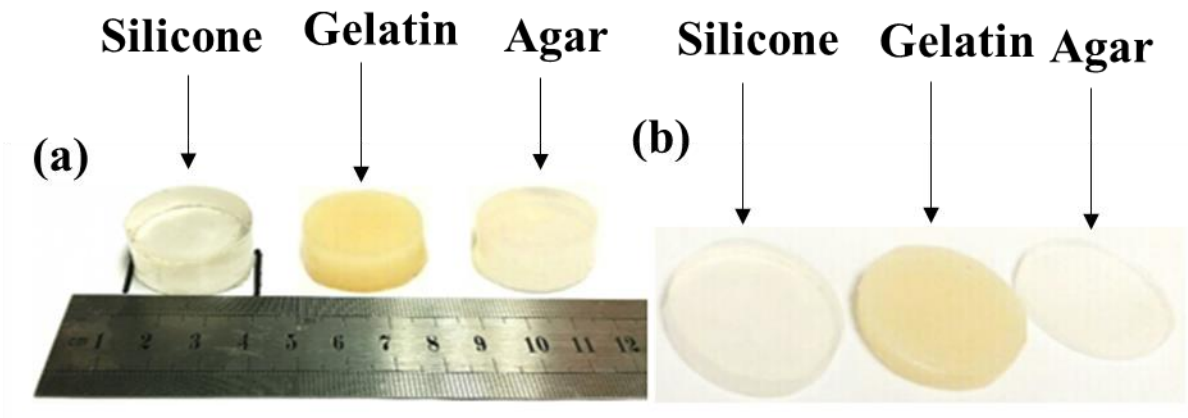

Figure 3.1: Samples size (a) for static property testing using MTS-43, and (b) Viscoelastic property testing using DMA

3.2.2 Mechanical property testing

Compression tests of all three groups of materials were performed using MTS and DMA with preloads of 0.05 N, 0.1 N, and 0.2 N at room temperature (18 ^{o}C to 20 ^{o}C). These preloads were applied to improve contact between the compression plate and the surface of the samples. Using the pre-existing mould, there were 10 samples fabricated for each recipe used to mimic skin, adipose and inclusion tissues. For agar and gelatin, a fresh sample was used for each experiment, to avoid any time history dependent effects on their viscoelasticity. To ensure measurement reliability, each sample was tested five times and the mean of the resulting elastic and storage moduli were calculated for each material.

To determine the hysteresis curve, a quasi-static uniaxial compression loading and unloading applied under a strain rate of +/- 0.5mm/min was performed. The elastic modulus of each sample was calculated during this quasi-static uniaxial compression. A 100 N load cell was used with the MTS machine to perform the tests. Due to the brittle nature of agar, initial testing above 15% of strain damaged the samples, so compression tests were stopped at 15%

strain for this material. While silicone and gelatin are more ductile, the compression tests were also stopped at 15% strain to simplify comparisons with agar samples.

DMA testing is used to characterize the viscoelastic behaviour of materials. To measure the storage modulus, an oscillatory test using a frequency sweep method at room temperature was applied to each sample. The frequency was varied from 0.1-100 Hz with increments of 12 Hz for gelatin and silicone, and 0.1-50 Hz with increments of 25 Hz for agar due to water content beyond 50 Hz samples slides.

Polymers like agar, gelatin and silicone have nonlinear, elastic behaviour that can be represented by a hyperelastic model. Hyperelastic models, namely Neo-Hookean [244], Mooney Rivlin [244, 245] and Ogden [246] models, are fitted to data to capture the nonlinear characteristics of materials to provide insight into tissue stress strain curve nonlinearities. The parameters of the resulting identified hyperelastic model are extracted, which can also be obtained from or utilized in nonlinear elastography.

Neo-Hookean (NH) is the simplest hyperelastic model, and is the reduced version of the Mooney Rivlin model [244]. The stress-strain relationship is derived from the strain energy density function denoted W. For the Neo-Hookean model, the strain energy density is given by the following equation:

$$W = C_{10}(I_1 - 3) \tag{3.1}$$

Where I_1 is the first deviatoric strain invariant and C_{10} is the material constant related to shear modulus.

Mooney Rivlin [244, 245] is the material model are used to represent incompressible, isotropic and elastic materials. For the Mooney Rivlin model, the strain energy density is defined:

$$W = C_{10}(I_1 - 3) + C_{01}(I_2 - 3) \tag{3.2}$$

Where C_{10} and C_{01} are the material constants for a 2 parameter model, which are determined empirically.

The Ogden model [246] is popularly used to fit isotropic biological tissues. The Ogden strain density energy function is written in terms of principal strains instead of the invariants. For the Ogden model, the strain energy density is defined:

$$W = \sum_{r=1}^{N} \frac{\mu_r}{\alpha_r}(\lambda_1^{\alpha_r} + \lambda_2^{\alpha_r} + \lambda_{13}^{\alpha_r} - 3) \tag{3.3}$$

Where $N = 1,2,3,$ ... and λ is the stretch ratio and μ_r and α_r are constants. The initial shear modulus is given as$2\mu = \sum_{r=1}^{N} \mu_r \alpha_r$.

3.3 Results and discussion

The elastic and viscoelastic properties of skin, adipose, and tumour sample made from all three materials are compared with preloads 0.05 N, 0.1 N, and 0.2 N. Elastic modulus, storage modulus, and loss modulus values for agar, gelatin, and silicone are summarized in Tables 3.3, 3.4 and 3.5. Mechanical properties, of real breast tissue, as reported in the

literature, and mimicking materials with adipose to inclusion ratios are summarized in Table 3.6 for comparison.

3.3.1 Effects of preload on strain

In biological tissue, the Young's Modulus cannot be assumed constant as a function of preload. The results in Table 3.2 show the effect of preload on strain on each sample of agar, gelatin, and silicone material. At all preloads of 0.05 N, 0.1 N and 0.2 N, pre-compression strain ranges from 0.3% -4.8%, 0.3% - 6% and 0.3% - 14.6% for agar, gelatin, and silicone, respectively. It can be noted that agar is stiffer as compared to silicone and gelatin. For all three materials, each adipose mimicking tissue sample has a higher pre-compression strain percentage compared to inclusion mimicking tissue sample because adipose mimicking tissue samples are softer than inclusion mimicking tissue samples.

Table 3.2: Effects of preload on samples in MTS testing

Preload (N)	Pre-compression Strain %								
	Agar			**Gelatin**			**Silicone**		
	Skin	Adipose	Tumour	Skin	Adipose	Tumour	Skin	Adipose	Tumour
0.05	0.4	1	0.3	0.3	1.5	0.3	0.3	3.3	0.5
0.1	1	2.2	0.5	0.6	3	0.6	0.5	7.3	1.4
0.2	2.2	4.8	1.1	1.2	6	1.3	1	14.6	3

3.3.2 Elastic characterization using MTS

Figure 3.2 shows the upper and lower portions for the quasi-static uniaxial compression loading and unloading cycle of all three material skin samples. Hysteresis curves show each material is viscoelastic. The energy dissipated during the loading-unloading cycle is given by the area within the loop. Due to their more ductile nature, gelatin and silicone materials show

more energy dissipation than agar. For elastic modulus measurements, only the loading part was considered. The elastic modulus of all three materials were calculated from the initial linear region up to 5% strain.

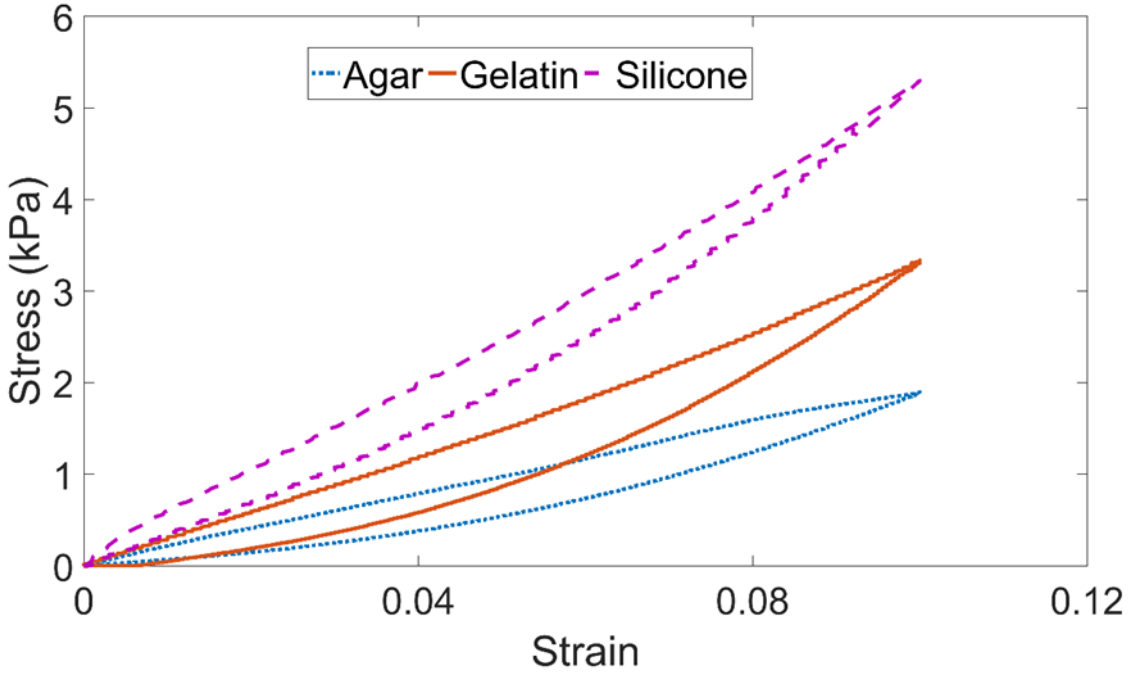

Figure 3.2: Hysteresis curve of agar, gelatin, and silicone for MTS initial testing

Figure 3.3 shows the loading stress strain behaviour of agar, gelatin and silicone samples for skin with preloads of 0.05 N, 0.1 N, and 0.2 N from which elastic modulus can be determined. Elastic moduli for agar and gelatin for skin mimicking tissue sample increases with the increase of preload. However, the elastic modulus for silicone material for skin is independent of preload up to 0.2 N. Thus, a large preload would be required to achieve a greater elastic modulus.

The elastic moduli of the skin samples for each group of materials are shown in Table 3.3. Mechanical properties of human skin depend upon skin thickness, stress applied to the skin during experiments, types of experiments, sex, and age. Elastic moduli of human skin measured in-vivo varies largely from 0.02 MPa to 57 MPa [247]. To obtain mechanical

properties of human skin in-vitro is not easy because removing it from its natural environment and pre-tensioning may cause changes in the mechanical properties.

Figure 3.4 shows the loading stress strain behaviour of agar, gelatin and silicone adipose mimicking tissue samples with preloads of 0.05 N, 0.1 N, and 0.2 N. The elastic modulus for silicone remain almost constant for adipose mimicking tissue sample with increasing increments of preload, similar to results in Krouskop et.al, where breast adipose tissue has a constant modulus over the strain range [225]. For agar, elastic moduli remain constant for preloads 0.05 N and 0.1 N, and then increase with a preload of 0.2 N. In addition, adipose mimicking tissue samples for gelatin significantly decrease with increasing preload. Thus, agar and gelatin are dependent on preload, unlike silicone. Results are summarized in Table 3.3.

Figure 3.5 shows the loading stress strain behaviour of agar, gelatin and silicone tumour mimicking tissue samples with preloads of 0.05 N, 0.1 N, and 0.2 N. The stiffness ratio of adipose to tumour tissues plays an important role in how detectable the tumour is using elastography. It is the key to elastographic diagnosis. The elastic modulus of tumour tissues is much greater than adipose tissues [225]. All three tested materials for tumour mimicking tissue samples have greater elastic moduli than adipose mimicking tissue samples, as shown in Figure 3.5. The elastic modulus of tumour mimicking tissue samples for all materials is preload dependent.

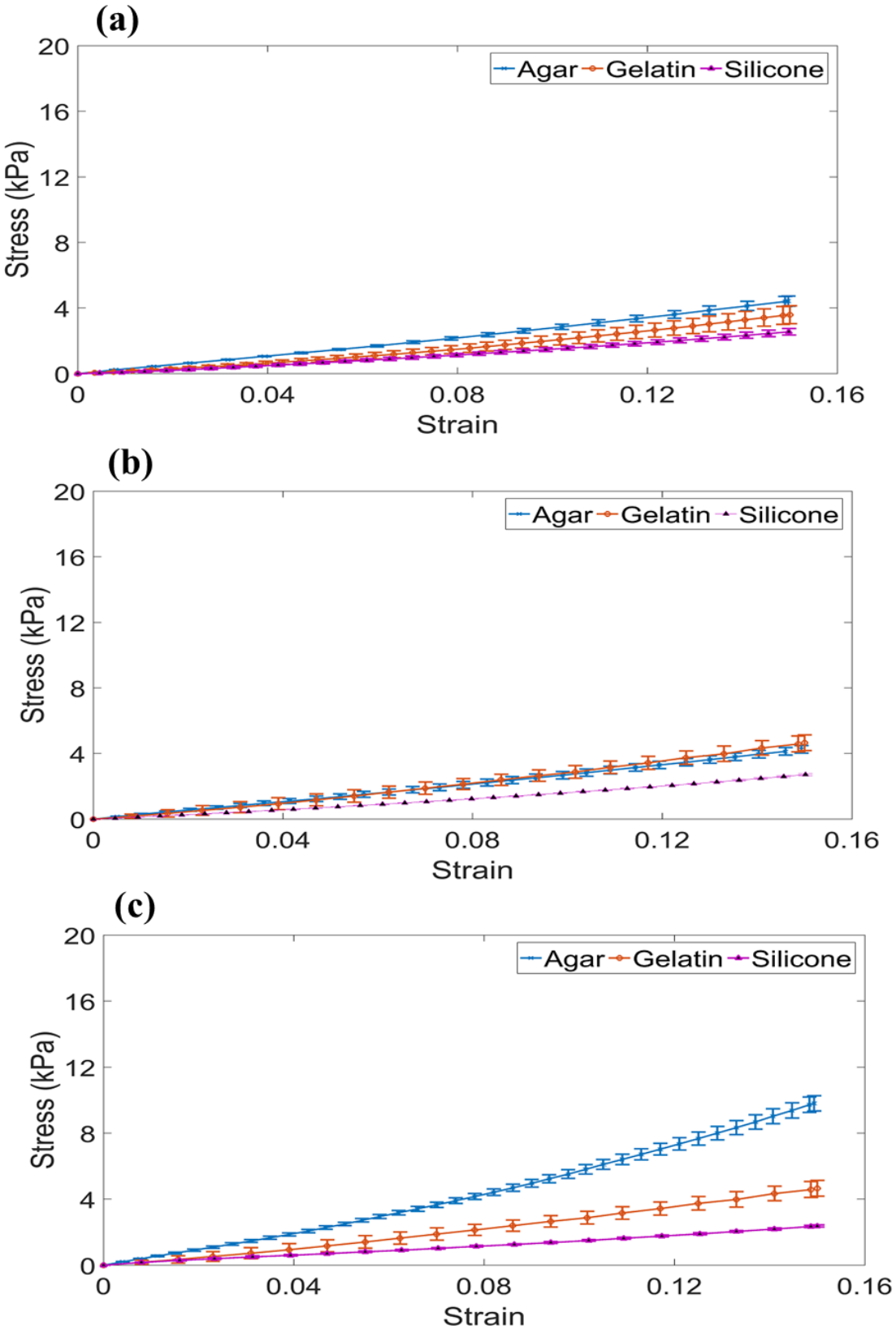

Figure 3.3: Stress-strain behaviour for all three materials for skin sample with: (a) preload 0.05 N (b) preload 0.1 N, and (c) preload 0.2 N

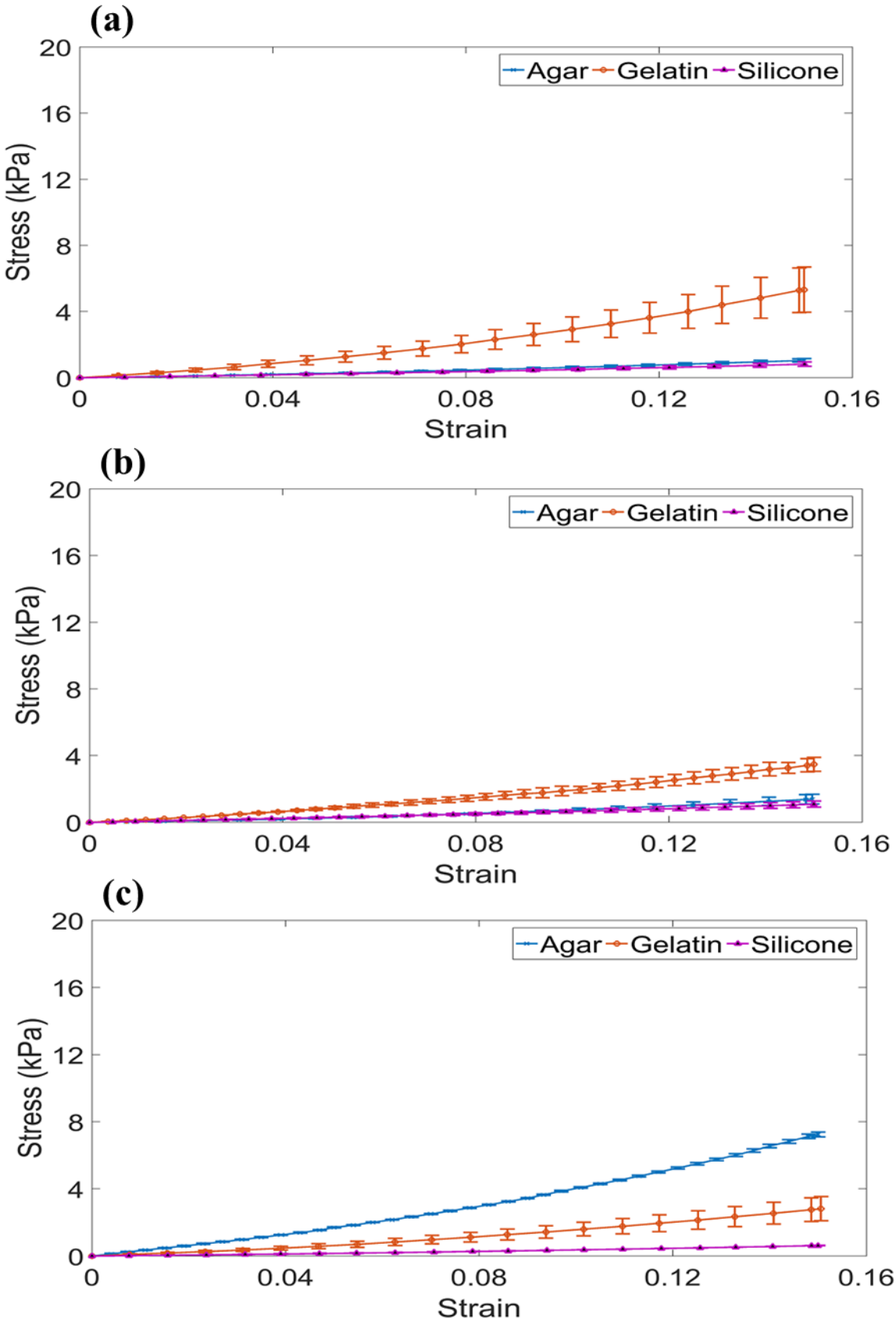

Figure 3.4: Stress-strain behaviour for all three materials for adipose sample with: (a) preload 0.05 N (b) preload 0.1 N, and (c) preload 0.2 N

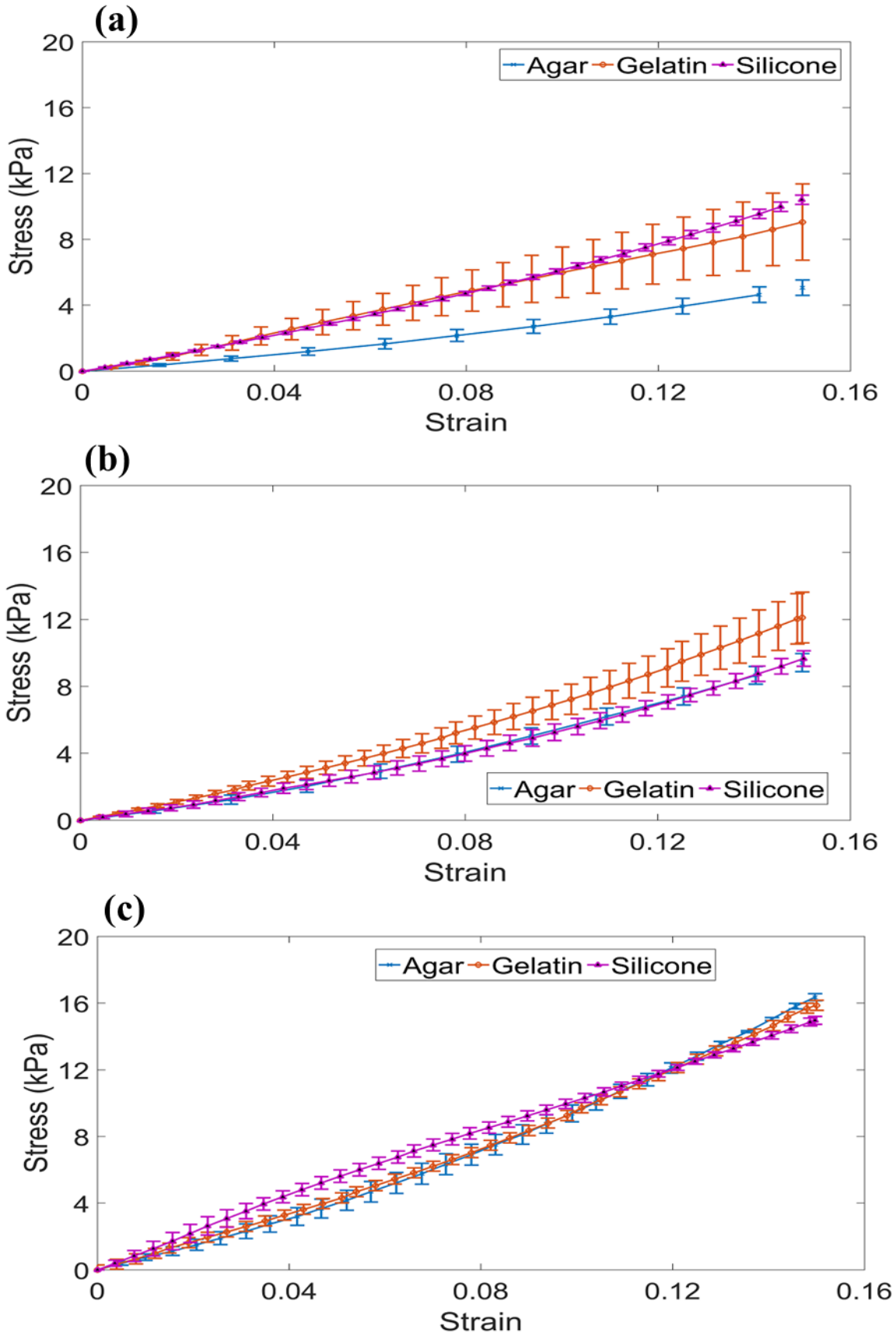

Figure 3.5: Stress-strain behaviour for all three materials for tumour sample with: (a) preload 0.05 N (b) preload 0.1 N, and (c) preload 0.2 N

Table 3.3 shows the static property summary of all three materials. For preloads 0.05 N, 0.1 N, 0.2 N, the adipose to tumour mimicking tissue sample ratio of silicone materials are 1:11, 1:10, and 1:19. For gelatin they are 1:2, 1:3, and 1:5, and for agar they are 1:5, 1:9, and 1:2. The ratios for silicone materials are potentially better than those for gelatin and agar. Because as per literature [225, 248] the elastic modulus ratio of adipose to tumour tissue ranges from 1:5 to 1:15.

Table 3.3: Static property summary for all tests. Data shown as mean ±SD

Elastic Modulus (E) in kPa

Preload (N)	**Agar**			**Gelatin**			**Silicone**		
	Skin	Adipose	Tumour	Skin	Adipose	Tumour	Skin	Adipose	Tumour
0.05	26±1	5±0.4	26±5	17±3	23±5	56±2	14±1	5±0.7	57±1
0.1	27±5	5±0.8	46±7	26±4	18±2	63±7	15±0.3	6±0.6	59±9
0.2	49±3	33±0.2	81±10	28±5	17±3	85±19	15±0.3	6±0.4	112±10

3.3.3 Viscoelastic characterization using DMA

The viscoelastic behaviour of soft tissues can be measured by applying a periodic compression to a uniform thickness and cross sectional cylindrical/disc sample. The complex elastic modulus is defined:

$$E^* = E' + iE'' \tag{3.4}$$

The real part of the complex modulus (E') is called the storage modulus, representing the elastic portion, as it measure the stored energy. The imaginary part (E'') is called the loss modulus, representing the viscous portion, as it measure the amount of dissipated energy. The storage and loss modulii were obtained using a frequency sweep testing method. Storage and

loss modulii together help define the overall stiffness and dissipative properties of the material, dynamically.

The results of frequency sweep tests on the DMA for all three materials are shown in Figures 3.6-3.8 with preloads 0.05 N, 0.1 N, and 0.2 N. These figures show all the measured values of storage modulus and loss modulus by varying the frequency from 0.1-100 Hz for gelatin and silicone, and from 0.1-50 Hz for agar. Tables 3.4 and 3.5 show the storage modulus and loss modulus at 0.1 Hz frequency for all three tested materials.

Figure 3.6 shows the storage and loss modulii of agar, gelatin and silicone skin mimicking tissue samples with preloads of 0.05 N, 0.1 N, and 0.2 N. The storage modulus at 0.1Hz for agar and silicone skin mimicking tissue samples gradually increases with preloads of 0.05 N, 0.1 N, and 0.2 N. Whereas the storage modulus for gelatin skin mimicking tissue sample remains constant at 0.1Hz with all three preloads. It is noted that the storage modulus of gelatin skin mimicking tissue samples remain stable with frequency over the range of 0.1-10 Hz and variable near to 100 Hz for every preload value. The storage modulus remains almost same with frequency from 1-90 Hz for silicone skin mimicking tissue samples, and shows small variability near to 100 Hz for every preload value. In addition, for agar skin mimicking tissue samples, the observed storage modulus gradually increases with frequency from 1-10 Hz and then decreases near 50 Hz.

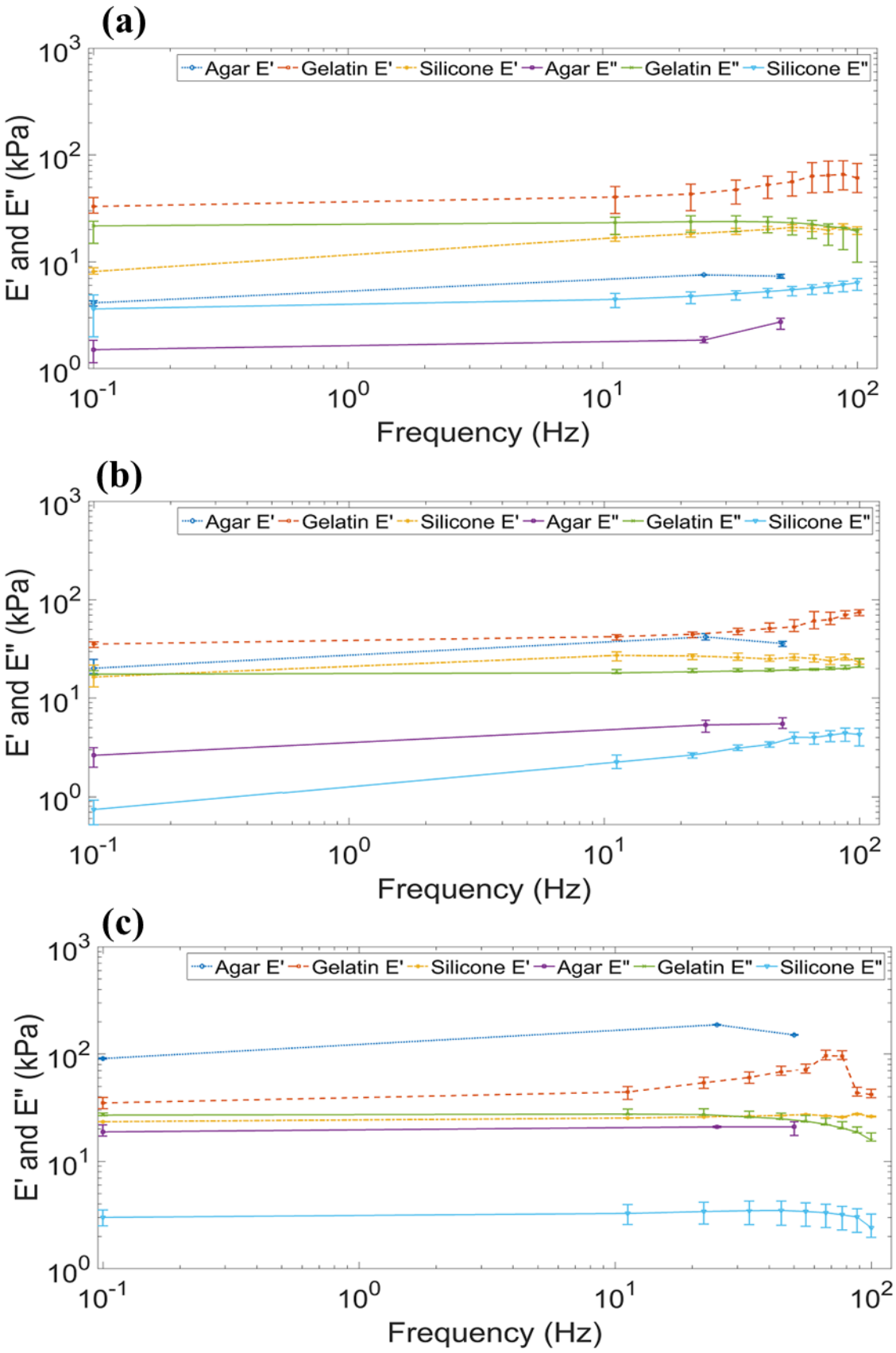

Figure 3.6: Variation of storage and loss modulus for all three materials for skin sample with: (a) preload 0.05 N (b) preload 0.1 N, and (c) preload 0.2 N

Figure 3.7 shows the storage and loss modulii for agar, gelatin and silicone adipose mimicking tissue samples with preloads of 0.05 N, 0.1 N, and 0.2 N. The storage modulus at 0.1Hz for gelatin and silicone adipose mimicking tissue samples remains constant for all three preloads. In contrast, the agar adipose mimicking tissue sample gradually increases with increasing preload. The storage modulus for gelatin and silicone for adipose mimicking tissue samples remains stable with frequency over the range of 0.1-70 Hz with preload 0.05 N, 0.1 N, and 0.2 N. For agar adipose mimicking tissue samples are gradually increase with frequency from 0.1-25 Hz with all three applied preloads.

Figure 3.8 shows the storage and loss modulii for agar, gelatin and silicone tumour mimicking tissue samples with preloads of 0.05 N, 0.1 N, and 0.2 N and shows greater storage modulus for the tumour mimicking tissue samples compared to the skin and adipose mimicking tissue samples for all three materials. In addition, as the sample is more compressed, the storage modulus increases at frequency 0.1Hz. Gelatin material for tumour mimicking tissue samples show stable results with frequency range of 0.1-10 Hz, but become unstable near 100 Hz. For agar, the tumour mimicking tissue sample gradually increases from 0.1-25Hz and decreases near to 50 Hz. There is no noticeable variation in storage modulus for the silicone tumour mimicking tissue samples with frequency.

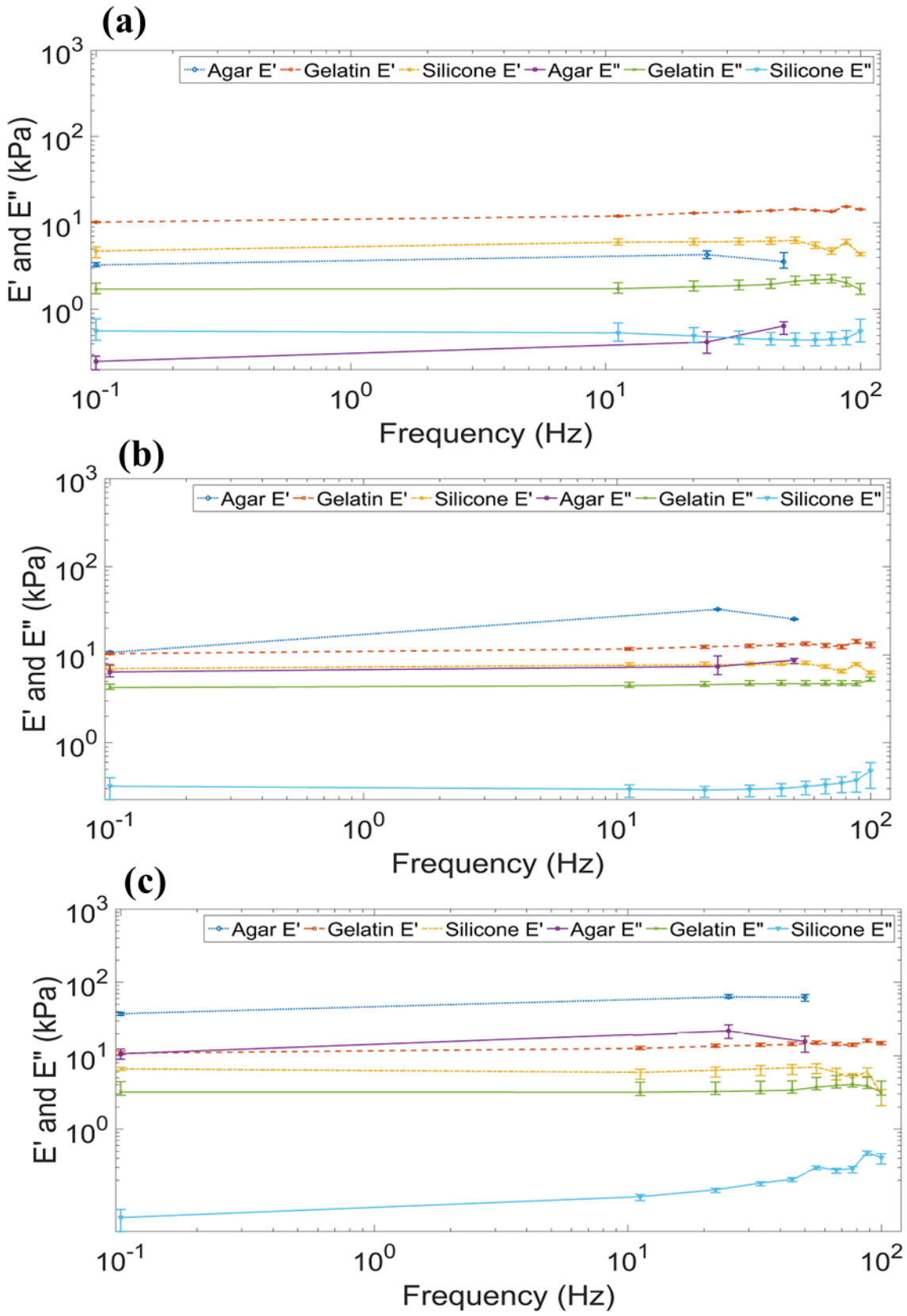

Figure 3.7: Variation of storage and loss modulus for all three materials for adipose sample with: (a) preload 0.05N (b) preload 0.1N, and (c) preload 0.2N

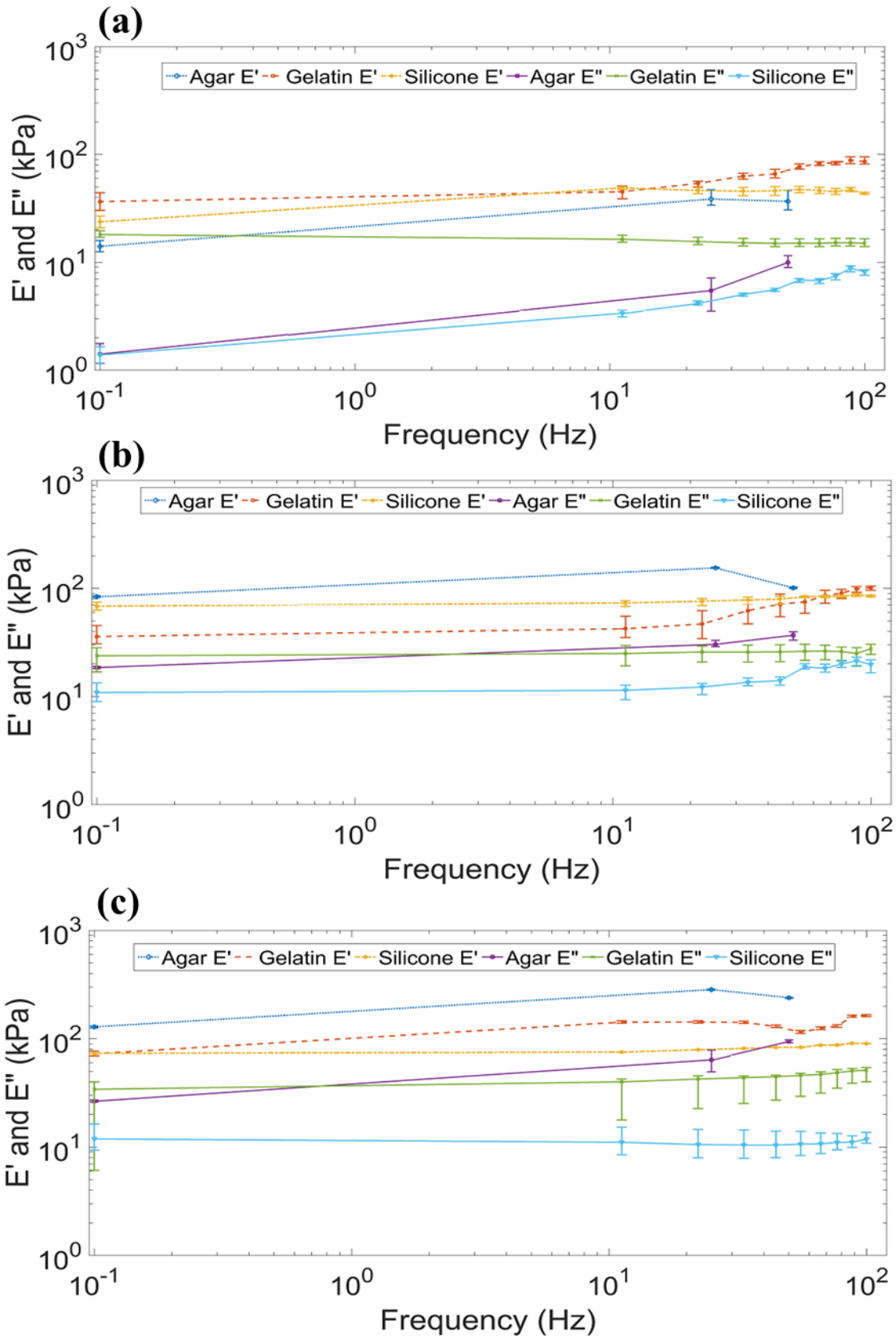

Figure 3.8: Variation of storage and loss modulus for all three materials for tumour sample with: (a) preload 0.05 N (b) preload 0.1 N, and (c) preload 0.2 N

The storage modulus ratios over all three preloads of adipose to tumour mimicking tissue samples for silicone materials are 1:5, 1:11, and 1:12. For gelatin they are 1:3, 1:3, and 1:11. For agar they are 1:4, 1:8, and 1:3. The ratios for silicone materials are better than those for gelatin and agar, due to their values being relatively close to what has been reported in real breast tissues, as summarized in Table 3.6.

Table 3.4: Storage modulus summary for all tests at 0.1Hz. Data presented as mean ±SD

Storage Modulus (E') in kPa

Preload (N)	**Agar**			**Gelatin**			**Silicone**		
	Skin	Adipose	Tumour	Skin	Adipose	Tumour	Skin	Adipose	Tumour
0.05	4±0.2	3±0.1	14±2	32±6	10±0.1	36±7	8±2	5±0.7	24±3
0.1	20±4	10±0.4	83±7	35±2	10±0.2	35±8	16±4	6±0.4	68±5
0.2	91±10	37±2	128±15	35±4	10±0.6	109±9	23±0.01	6±0.3	73±0.08

Table 3.5: Loss modulus summary for all tests at 0.1Hz. Data presented as mean ±SD

Loss Modulus (E'') in kPa

Preload (N)	**Agar**			**Gelatin**			**Silicone**		
	Skin	Adipose	Tumour	Skin	Adipose	Tumour	Skin	Adipose	Tumour
0.05	2±0.3	0.3±0.04	1.4±0.3	22±4	2±0.8	18±0.8	4±1	0.6±0.1	1.4±0.2
0.1	3±0.5	6±1	18±0.4	17±2	4±0.6	24±5	0.7±0.2	0.3±0.08	11±2
0.2	19±3	11±2	26±0.6	27±1	3±1	34±5	3±0.5	0.06±0.02	12±4

It can be noted that storage modulus is always ~20 times larger than the loss modulus for all frequencies. This result is similar to the behaviour of biological tissues [225]. For an agar concentration of 2g (adipose mimicking tissue sample) and 4g (skin mimicking tissue sample) at preloads of 0.05 N, 0.1 N and 0.2N, the loss modulus values are uniformly lower than 30 kPa, which represents low amount of energy damping for agar mimicking tissue

samples, but matches results in [249]. In general, the loss modulus increases with the increase of agar and gelatin concentration. For silicone, the loss modulus of adipose mimicking tissue samples are smaller than in the skin and tumour mimicking tissue samples, which matches expectations and prior reports [184].

Mechanical properties of real breast tissue, as reported in the literature, and mimicking materials with adipose to tumour ratio are summarized in Table 3.6 for comparison. The absolute values of elastic modulus and storage modulus are not very comparable to that of real tissue, because of the different pre-compression and preload values applied in their experimental methods and also different measurement methods [225, 248]. It is obvious that real human breast tissues are more complex and heterogeneous. Thus, it is very hard to achieve the same absolute values. However, the ratio of moduli for adipose to tumour sample in this work compares very well to that of real breast tissue, and this ratio is the key for diagnosis. Hence, absolute values that are close with good matches to ratios will provide a good phantom.

Table 3.6: Storage modulus in kPa summary of real breast tissues from literature and mimicking materials at 0.1 Hz

	Pre-compression/Preload	Adipose	Tumour	Adipose/tumour ratio
Real Breast Tissues [225]	5%	18±7	22±8	1:1
	20%	20±8	291±67	1:15
Real Breast Tissues [248]	3 g	3.25±0.9	16.38±1.5	1:5
Agar	0.05N	3±0.1	14±2	1:5
	0.1N	10±0.4	83±7	1:8
	0.2N	37±2	128±15	1:3
Gelatin	0.05N	10±0.1	36±7	1:3
	0.1N	10±0.2	35±8	1:3
	0.2N	10±0.6	109±9	1:11
Silicone	0.05N	5±0.7	24±3	1:5
	0.1N	6±0.4	68±5	1:11
	0.2N	6±0.3	73±0.08	1:12

According to [225], adipose breast tissue has a constant modulus over the strain range and the elastic modulus of tumour tissues is highly dependent on the level of tissue pre-compression used in the measurement. For example, the elastic modulus of tumour tissue was found to be 5 and 15 times larger than that of normal adipose tissue when applying pre-compression levels of 5% and 20%, respectively. This dependence confirms the nonlinear elastic behaviour often observed in biological tissues [225].

Similarly, the gelatin and silicone adipose mimicking tissue sample data in this study has almost constant storage modulus at all preloads, and tumour mimicking tissue samples were also similarly dependent on the preload. However, the effect of preload on agar mimicking tissue samples is unlike silicone and gelatin. At all agar concentrations (2-6 g) there is a significant variation in storage modulus at 0.1 Hz frequency at all three preloads. In summary, agar materials can be used as tumour tissue phantoms with additional agar concentration to obtain the right material properties and ratios.

Overall, elastic moduli and storage moduli of all three materials in mimicking of skin, adipose and tumour tissue samples is summarized in Tables 3.3 and 3.4. It is notable that for agar and gelatin, the mechanical properties depend on the concentration. Thus, increasing the agar and gelatin concentration increases the stiffness of the sample. This control allows different tissue types to be mimicked based on their different tissue stiffness in vivo.

In gelatin based phantoms, apart from increasing the concentration of gelatin, it is possible that the use of formaldehydes to increase the melting point of the gel. This approach simultaneously increases the resulting material stiffness, as formaldehyde can be used to increase cross-linking among collagen fibres. Gelatin modulus and mechanical properties

depend not only on the dry-weight concentration used in the mixture, but also on the Bloom value of the gelatin used.

Agar mechanical and imaging characteristics can be achieved similar to those of soft tissues. This goal is achieved by adjusting concentration and the amount of liquid solution. Its main limitation is its low toughness, making it fragile during handling. For silicone, the properties are a function of the creation process, such as curing time and the amount of silicone used as a percentage.

The results presented provide guideline ranges for custom tailoring the material properties towards the intended values and/or ratio of tumour to healthy tissue properties, where specific outcomes or formulations depend on the range of factors presented. However, overall, the results show what is possible and how these properties vary across frequencies not typically considered in these phantom materials. All material samples were stored in a controlled environment to avoid dehydration during experiments.

3.3.4 Hyperelastic characterization

The stress strain curve of polymer materials have two regions, an elastic region in the initial portion of the curve and a hyperelastic region where material exhibits more stress for a small increment in strain. After the results and discussion presented, silicone material is selected as a best choice because of its appropriate elastic and viscoelastic properties. The next step is to find hyperelastic parameters by fitting uniaxial compression experimental data for silicone based skin, adipose and tumour mimicking tissue sample into the Neo-Hookean, Mooney Rivlin and Ogden models. The results are shown with mean experimental stress strain data in Figure 3.9 and computed parameters with goodness of fit (R^2) are shown in Table 3.7.

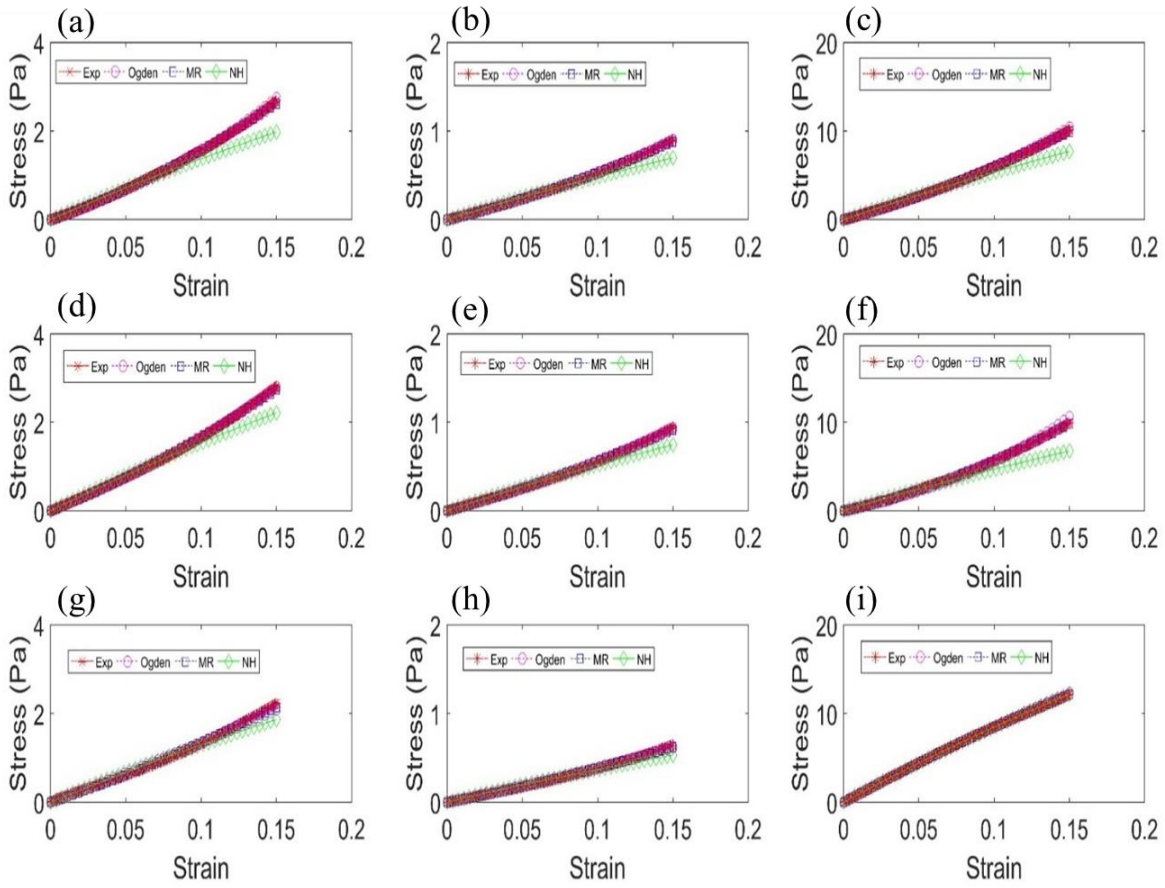

Figure 3.9: Neo-Hookean(NH), Mooney Rivlin(MR), Ogden models are fitted to experimental stress strain data for Silicone (a,d,g) Silicone skin tissue sample preload 0.05, 0.1, 02 N (b,e,h) Silicone adipose tissue sample preload 0.05, 0.1, 02 N (c,f,i) Silicone tumour tissue sample preload 0.05, 0.1, 02 N

Table 3.7: Summary of hyperelastic models for silicone material

Preload	Models	Skin	R^2	Adipose	R^2	Tumour	R^2
0.05 N	**Ogden (kPa)** μ_1	4.11	0.993	1.49	0.998	16.22	0.994
	α_1	11.12		9.61		10.52	
	MR (kPa) C_{10}	12.83	0.998	4.08	0.998	46.78	0.998
	C_{01}	-10.04		-3.41		-39.28	
	NH (kPa) C_{10}	2.51	0.986	0.88	0.992	9.79	0.988
0.1 N	**Ogden (kPa)** μ_1	4.79	0.996	1.62	0.996	13.43	0.989
	α_1	9.17		8.87		13.35	
	MR (kPa) C_{10}	11.95	0.998	4.00	0.998	55.73	0.998
	C_{01}	-9.75		-3.26		-49.74	
	NH (kPa) C_{10}	2.81	0.993	0.94	0.994	8.589	0.974
0.2 N	**Ogden (kPa)** μ_1	4.31	0.998	1.20	0.997	30.78	0.998
	α_1	6.23		7.21		2.33	
	MR (kPa) C_{10}	8.27	0.999	2.49	0.997	14.17	0.999
	C_{01}	-6.38		-1.96		1.50	
	NH (kPa) C_{10}	2.36	0.997	0.67	0.997	15.50	0.998

The Ogden and Mooney Rivlin model appeared to be the most suitable choice for predicting the behaviour of a given silicone composition because of its ability to match experimental data points at small and large strain values. It can be noted that the goodness of fit (R^2) of Neo-Hookean model is less than the other two models, but all are excellent. Since we consider uniaxial isotropic material behaviour predominantly in elastography, the Mooney Rivlin model could be used for fitting the experimental curve of the prepared skin, adipose and tumour mimicking tissue samples.

Overall, this work has established hyperelastic models for characterizing constitutive relations of silicone based samples and computed parameters. These parameters could be used as input in finite element hyperelastic simulation of silicone based breast phantoms and modelling of silicone breast tissue. Hence, they enable better elastographic analysis, as well as enabling better finite element modelling.

3.4 Environmental effects on samples

When agar material samples were stored in a controlled environment at approximately 20 ^{o}C, within a week all samples developed a fungal growth. This growth is due, in part, to the availability of water in the samples.

Gelatin mimicking tissue samples for skin, adipose, and tumour were mixed with different water and oil concentrations to change the elastic modulus and storage modulus values. Gelatin materials show appropriate mechanical properties in terms of stability in the storage modulus with the range of frequencies in DMA testing. However, because of its high water content, relative humidity will effect mechanical properties over time, as evaporation over longer term storage means its mechanical properties change. Thus, such a phantom cannot be used for long term, reuse, and comparison.

Silicone materials are thus more attractive than agar and gelatin because of their stable material properties and fungal resistance. Greater consistency means they can be used for long term testing and reuse. Hence, they could be used for repeated testing over longer periods, so different elastographic systems could be compared with the same ground-truth. Figure 3.10 shows the environmental effects on agar, gelatin, and fungal resistance silicone

samples. In summary, the overall advantages and disadvantages of each material are outlined in Table 3.8.

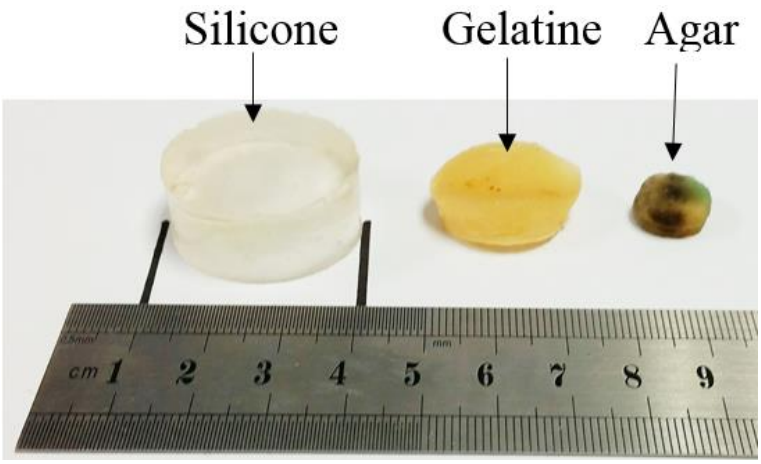

Figure 3.10: Environmental effect on samples with significant fungal growth on agar and gelatin

Table 3.8: Mechanical property summary for all tests

Materials	Advantages	Disadvantages
Agar	Easy to prepare Takes 20min to solidify in open air Ranges of moduli can be achieved by varying agar concentration	Brittle in nature Effected by environmental influences e.g fungus Slides and leaks water during experiments
Gelatin	Inexpensive Ranges of moduli can be achieved by varying gelatin concentration	Effected by environmental influences e.g fungus Take approximately 5 hour to prepare sample and solidify
Silicone	Easy to prepare and cure Good mechanical properties Fungal resistance	Sticky

3.5 Breast shaped silicone phantom fabrication

Symmetric breast shaped silicone phantoms were fabricated using a core and cavity mould. For skin mimicking tissue phantom total amount of 55g of 100% A341 solution has been used. A vacuum chamber was used to remove air bubbles from the silicone. The solution is poured onto the breast shaped cavity and the mould is placed on top of it. This produces a thin and uniform 1 mm thick skin layer. The skin is cured at 60 ^{o}C within an hour.

Once skin layer is cured the core can be removed, a Perspex plate is placed on top of the cavity with a support of two plates. Nylon bolts are attached for ease of handling and clamping during experiment on DIET machine.

For adipose mimicking tissue phantom 192g of A341 and 299g of DC 200 solution has been used and mixed properly. The mixture is then placed inside the vacuum pump to remove bubbles and then poured into the cavity mould. The adipose mimicking tissue phantom material is cured at 60 ^{o}C within two hours. Once the adipose mimicking tissue silicone phantom is cured, the breast shaped phantom can be easily removed from the mould cavity.

For tumour mimicking tissues phantom, 40g of A341 and 60g of LSR-05 was used. Three different sizes of tumour mimicking tissue were fabricated in spherical shapes of 20 mm, 10 mm and 5 mm diameter. Both materials are mixed well and placed inside the vacuum pump to remove bubbles. The mixture is then poured with syringe into the tumour mould and placed inside the oven to cure at 60 ^{o}C for three hours. The tumour mimicking tissue phantom is then suspended from a support in by a wire into the breast cavity to create an inclusion. Figure 3.11 shows the overall procedure to fabricate a phantom.

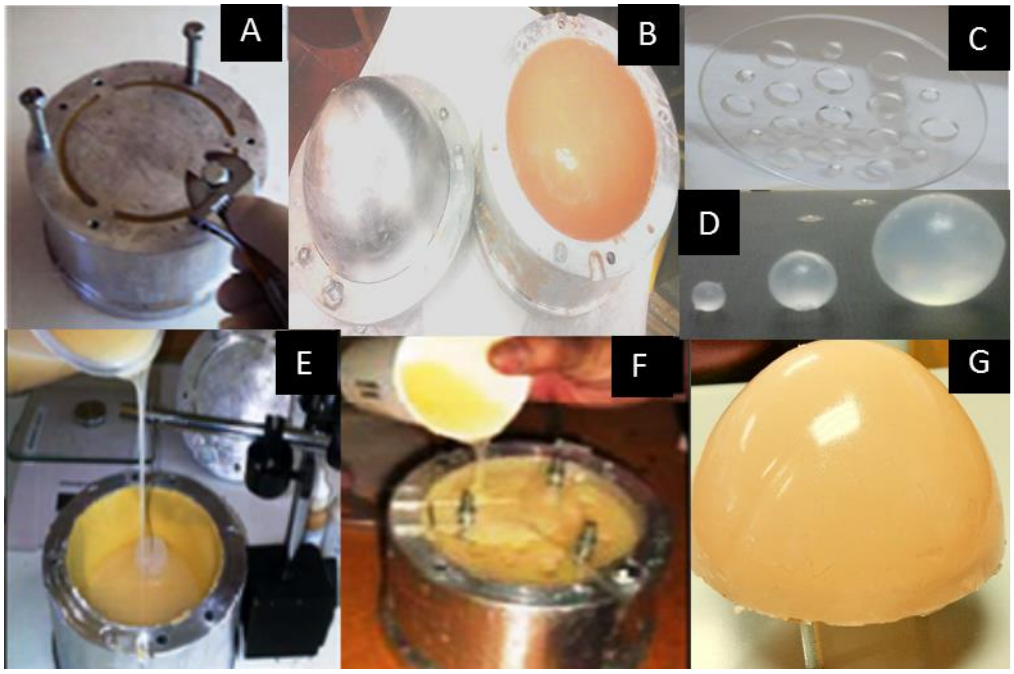

Figure 3.11: Fabrication process of silicone breast shaped phantom: (A) Procedure of core extraction (B) Cured skin layer (C) Perspex plate (D) Tumour with different diameter sizes (E) Placing a tumour with a wire (F) Pouring adipose silicone (G) Fabricated breast shaped phantom

3.6 Summary

Human breast tissues are complex and replicating their mechanical properties in the laboratory can be very challenging. The aim of this chapter was to find the most suitable, commonly available material to mimic breast tissue for use in elastography. In summary, all presented materials are suitable for tissue-mimicking phantoms under different conditions. However, there are various drawbacks of agar regarding its utility in stable homogenous phantoms: (1) Agar is a brittle gel that can fracture with moderate strains; and (2) it exhibits a much more rapidly increasing elastic modulus with preload than normal breast tissues, where, in contrast, agar and gelatin are over 80% water and have a stiffness similar to that of soft tissue. Thus, because of water content in agar and gelatin, they have limited durability due to environmental variations. Therefore, both materials may not be suitable for repeated

application over several days or weeks, limiting their usefulness in creating tissue mimicking phantoms for this application.

Silicone is a soft tissue material with an appropriate elastic modulus ratio of adipose and tumour mimicking tissue sample. It is easy to prepare samples with a range of mechanical properties and it is fungal resistant. Measured elastic moduli for silicone mimicking tissue samples range from 5-112 kPa and storage moduli range from 5-73 kPa for all normal and tumour mimicking tissue samples. The stiffness ratio of adipose to tumour for silicone mimicking tissue samples range from 1:5-1:12 compared with the real human breast tissues range from 1:1-1:15. Additionally, experimental data from uniaxial compression tests of skin, adipose and tumour mimicking tissue samples were obtained to input into finite element commercial software to calibrate hyperelastic model coefficients for given silicone behaviour.

Chapter 4: Finite element modelling and validation procedure of breast shaped phantom

The fabricated breast shaped phantom dimensions and hyper-elastic properties from Chapter 3 were used to construct a biomechanical finite element (FE) model of breast shaped phantoms. An accurate model could be used to more rapidly generate motion data. Such models do not currently exist, but would enhance development of this screening technology. This Chapter presents the development of a finite element model approach to analyse breast shaped silicone phantoms used to mimic cancerous lesions, both with and without stiffer inclusions.

4.1 Introduction

The modelling of biomechanical tissue properties has gained considerable interest in a range of clinical and research applications. Finite element (FE) modelling enables analysis and evaluation of structures and systems for which there are no theoretical models or solutions because of the complexity of the material properties and boundary conditions. Yu-Neifert [250] was one of the first to model breast tissue movement to determine the applicability of holographic interferometry in breast cancer detection. Kita et al. [251] created breast model of deformations under mammographic compression.

In 2000, Azar et al. [252], constructed a finite element model of the breast from MR data to calculate the location of a stiffer inclusion by using imaging data taken without breast

compression. They then compressed the finite element model. This method helped guide a clinician in a breast biopsy to sample the right region of tissue. In 2001, Samani et al. [253] also constructed 3D finite element models of the breast using MRI data to perform mesh convergence studies to assess the accuracy of the model.

Several studies on mechanical properties of the breast have been investigated to evaluate deformation of the breast under external compression [254-257]. In a recent study, image data were collected from ten patients who had undergone mammography screening and MRI screening. The breast models were created from MR images and relationships between compressed breast thickness, breast volume, glandularity, and compression force were provided for use in clinical mammography [258].

In biomedicine, some other recent applications of FE modelling include guiding clinical biopsies [259] and further models of modelling high strain tissue compression [258]. It has also been applied for use with X-ray mammography to localize mammogram identified inclusions [260, 261], as well as registering for X-ray and MR mammography, validating non-rigid registration algorithms [262], and testing reconstruction algorithms for elastography [263]. Hence, FE models have a long history in the broad area of breast cancer screening and medical imaging.

DIET was initially developed and its first potential proof-of-concept using physical silicone phantoms [30, 184, 185]. However, a trial-and-error experimental approach can be time consuming when developing algorithms to analyse surface motions and create diagnostic metrics. This issue is particularly valid when testing new phantom cases is necessary, as an all new phantom must be made. An accurate computational model, able to repeat the

behaviour of these phantoms, would enable in-silico development of analytical diagnostic metrics for DIET without phantoms, as well as for any similar elastography methods for any similar type of phantom. Similarly, successful computational models and methods for simulating this type of physical phantom would be a first step in translation to modelling human breast tissues for similar research and development goals.

Thus, for diagnostic development, a finite element model of these phantoms, if it was able to provide the same motion data as a phantom, would enable far more rapid analysis and diagnostic development. In particular, it is far faster and easier to develop and run a finite element model of a phantom in a given configuration, with/without inclusions, than it is to develop and fabricate the phantom and then to test it physically. However, while finite element methods have been used extensively in areas related to breast cancer, there are no studies on this modelling for use in mimicking the mechanical properties of breast tissue or breast tissue phantoms for elastography. The closest prior work is that of Nielsen et al [261, 264] who model the high strain deformation and compression of breast tissue in mammography.

4.2 DIET experimental data

The DIET system images a range of breast shapes and sizes, so the position of the breast and actuator in each image varies between trials. Spherical coordinates (r,θ,φ) are used to estimate a parametric 3D model of the breast surface from frame images, for each of the $k = 10$ frames imaged over one harmonic cycle of actuation [30, 184, 188]. A grid of reconstructed 3D surface points is then projected onto the breast image. To estimate surface motion of these points, an optical flow algorithm is applied to pairs of frames [188]. Figure 4.1 shows points

on a breast phantom moving in a single loop direction in response to sinusoidal input after k=10 frames in a response cycle. One motion set includes ~15000 points on the surface of each phantom or breast multiplied by 10 measured points per sinusoidal response cycle [188]. While silicone phantom experiments are important in development, they were not intended to perfectly represent the breast. However, the material properties of the silicone used, and their fabrication, are designed to mimic realistic breast tissue properties and overall structure [184, 185] as described in Chapter 3. Silicone with approximately 4 times greater stiffness than that used to mimic healthy tissue [225] is used to represent stiffer lesions or inclusions, as shown in Figure 4.1. Overall, these phantoms capture essential shape, as well as healthy and inclusion material properties, to provide a realistic phantom for development.

Figures 4.1 as per caption under the figure defines the 3 phantoms used in this study, including the no inclusion healthy case. Data from 28 Hz, 30 Hz, and 32 Hz sinusoidal input frequencies with 1 mm amplitude are considered. These are the middle frequencies of DIET machine as described in Chapter 2. In each case, a two Newton (2N) preload is also applied, which ensures full contact between the phantom and the actuator and does not squash the phantom.

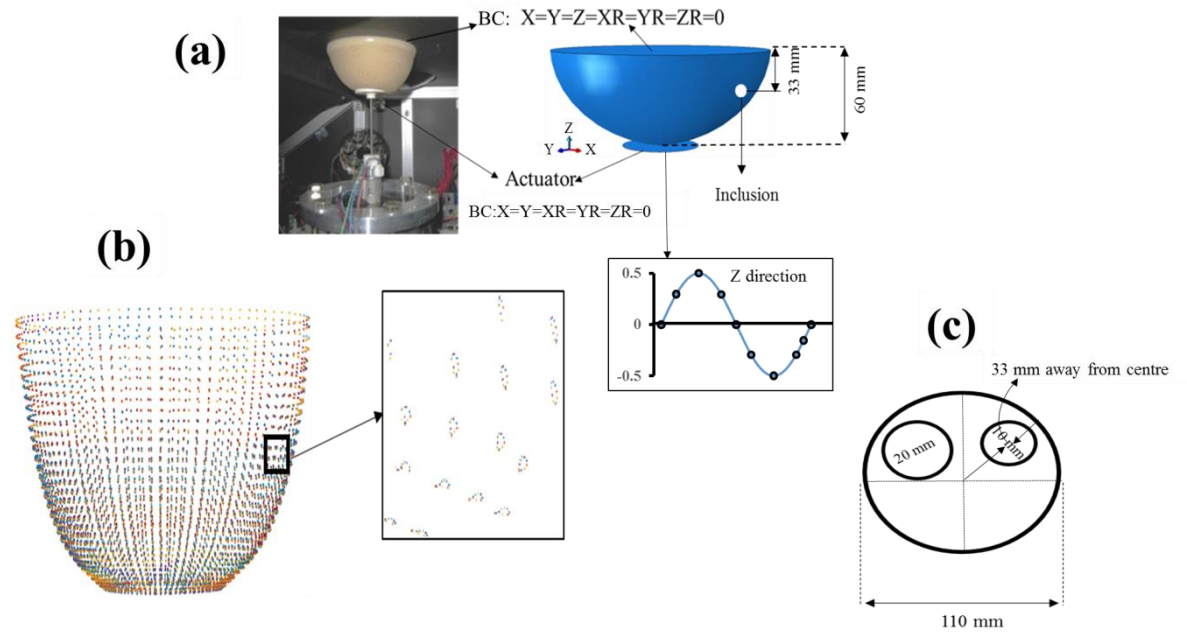

Figure 4.1: A total of three phantoms were constructed, a healthy (no inclusion), with a 10 mm inclusion and a 20 mm inclusion (a) Phantom in the DIET prototype and also shows geometry, dimensions, boundary conditions, and loading direction, the top of the phantom is fixed in all translations and rotations direction X=Y=Z=XR=YR=ZR=0 and also actuator displacement is on Z direction and X and Y translations and all three rotations (XR, YR, ZR) are fixed (b) Points on the breast motion after 10 frames, each frame represents different colour (c) Summary of two phantoms with a position of 20 mm and 10 mm inclusions (top view) – two phantoms were created and in each phantom there were 20 mm and 10 mm inclusion were inserted

4.3 Finite element modelling

FE modelling is implemented in ABAQUS version 6.14 (ABAQUS Inc., Johnston, Rhode Island, United States).

4.3.1 Geometry

The FE model geometry has the same dimensions as the fabricated phantom shown in Figure 4.1. The model assumes a homogenous, isotropic and nonlinear material [259]. For two

phantoms, spheres of 10 mm and 20 mm diameter were created and inserted to mimic an inclusion. Their location is also shown in Figure 4.1.

4.3.2 Boundary conditions and input loading

Boundary conditions represent the initial conditions applied to the model. Fixed boundary conditions are applied to nodes on the chest wall. The second boundary condition is at the actuator. The displacement of the actuator is strictly vertical, and thus, X=Y=XR=YR=ZR=0 for X and Y translations and all three rotations (XR, YR, ZR).

To mimic conditions in the actual DIET system operation, a vertical, static force of 2N is applied as a preload along the actuator z-axis, to ensure contact with the breast is maintained. Note this compressive force on the phantom improves the repeatability of results [265]. A 1 mm peak-to-peak input displacement is then applied on z-axis at 28 Hz, 30 Hz and 32 Hz.

4.3.3 Mesh convergence

3D solid elements were defined in the breast phantom volume, including for the inclusions where necessary. The challenge is defining the finite-element mesh that best mimics the structure of the breast shaped phantom in simulation, while minimizing model size and complexity. Soft breast tissue is assumed to show incompressible behavior [266]. Thus, a 3D free mesh was assembled using quadratic tetrahedral ten-node (C3D10M - Continuum 3Dimensional 10-node Modified)

Elements, as shown in Figure 4.2. These elements are especially attractive for complex models or curved surfaces [267]. Figure 4.2 shows a 10 node tetrahedral element.

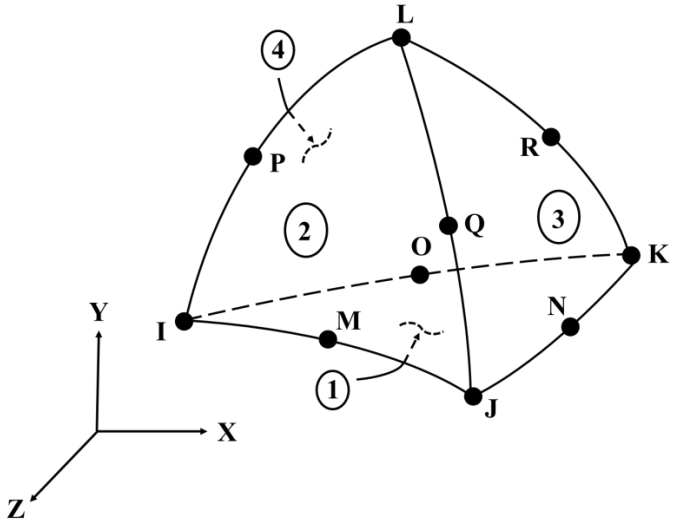

Figure 4.2: Tetrahedral elements, a 10 node quadratic tetrahedral element [268]

DIET experimental results provide phantom surface motion displacement information. Mesh convergence was thus assessed based on these nodal displacements, which is what the model will be judged upon in comparison. The analysis goal is to determine the mesh resolution yielding an accurate (within 5%) prediction of the measured static deformations for the initial loading conditions.

Thus, the modeled displacement of the 2N applied preload was recorded for each node on the surface of the modelled breast phantom. These nodes are expected to compress due to this loading condition. The deformation variation was calculated for each mesh refinement to choose the correct mesh size to validate the breast model. Element size was varied from 2-10 mm. Figure 4.3 and 4.4 show FE models with 2-4 mm elements had similar results lower than the tolerance. Thus, FE models with 4 mm elements were used for further analysis. The resulting model has a total 56611 nodes and 39867 elements, as shown in Figure 4.3.

Mesh 10 mm	No. of Nodes : 4078 No. of Elements : 2615
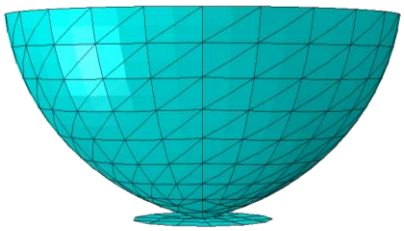	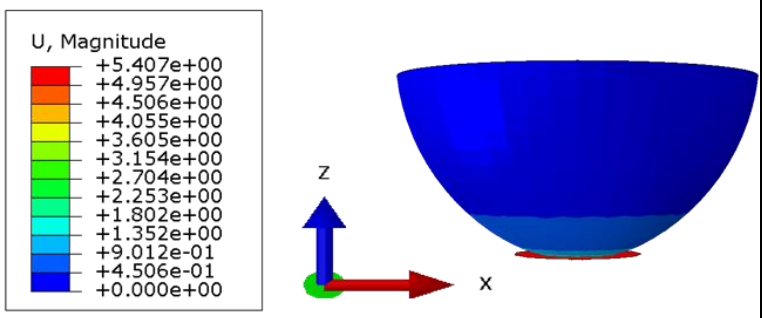
Mesh 8 mm	No. of Nodes : 8015 No. of Elements : 5360
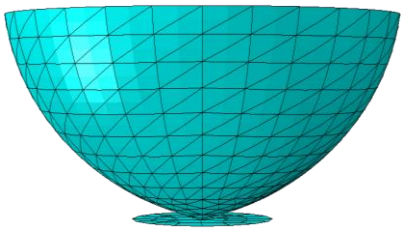	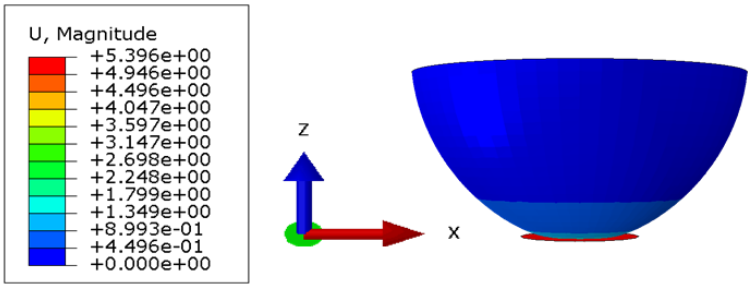

Mesh 6 mm	No. of Nodes : 16333 No. of Elements : 11109
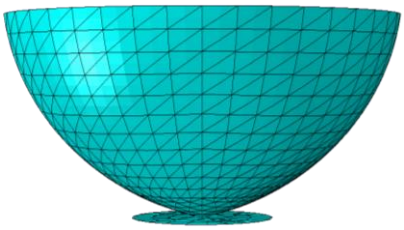	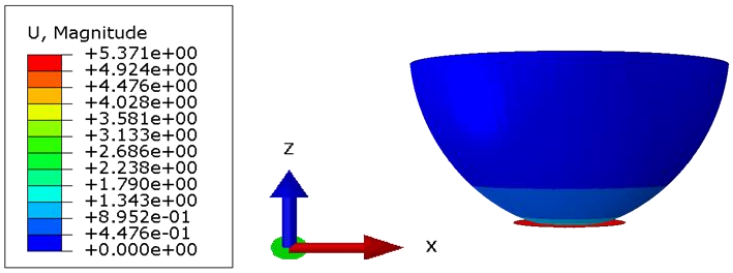
Mesh 4 mm	No. of Nodes : 56611 No. of Elements : 39867
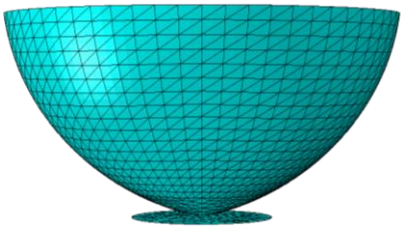	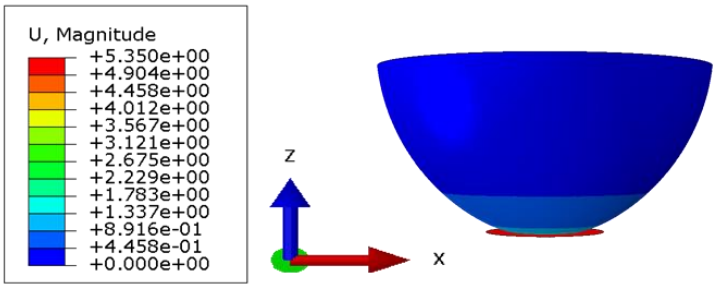

Mesh 2 mm	No. of Nodes : 358978 No. of Elements : 259220
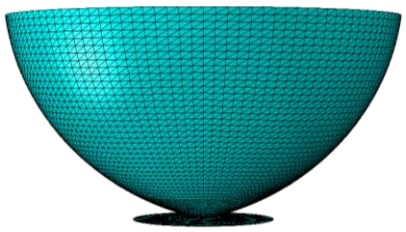	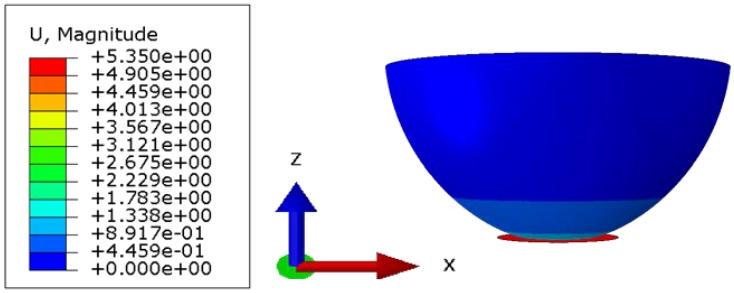

Figure 4.3: Mesh convergence study

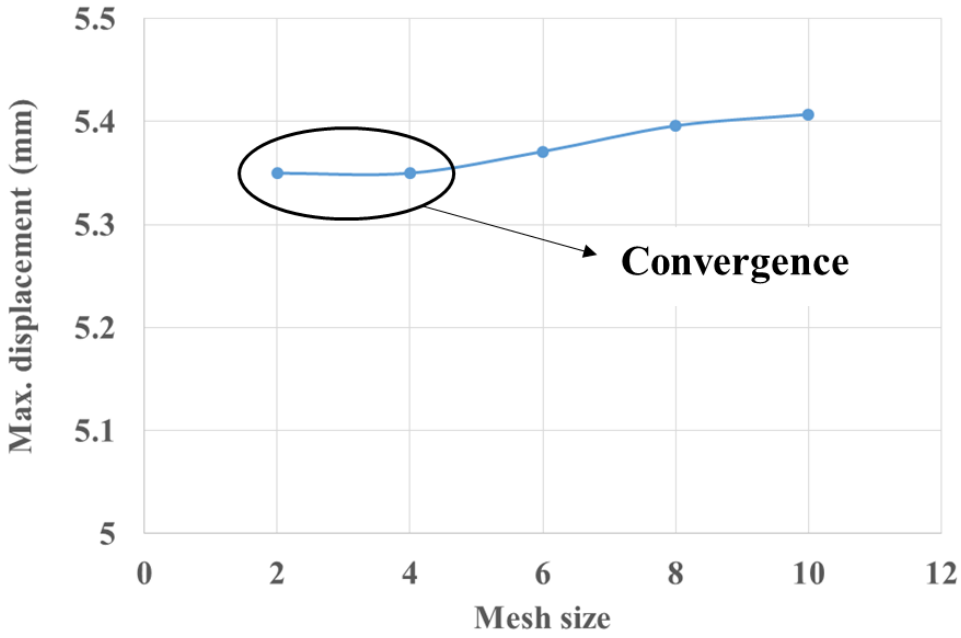

Figure 4.4: A plot of maximum displacement versus mesh size shows the changes in displacement results for the different mesh densities.

4.3.4 Material properties

Each element is assigned material properties corresponding to healthy and stiffer inclusion silicone phantom tissues. Hyper-elastic materials are well adapted to simulate soft tissue deformation. Based on Chapter 3, a Neo-Hookean hyper-elastic model is chosen to simulate these breast phantom tissues [264, 269]. Most biological tissues are also considered isotropic, homogenous, and incompressible. With these assumptions, it is possible to define the mechanical behavior of breast phantom tissue using a single elastic modulus, *E*, with neo-Hookean properties, which is the reduced version of the Mooney Rivlin model [244], with C_{10}= 0.67 kPa for fat tissue and C_{10}= 15.0 kPa for cancerous tissue [185].

4.4 Model validation

In this section, the k = 10 frame radial displacement magnitudes from the sinusoidal response are compared first. These absolute values provide a dynamic size validation per frame of the sinusoidal response. They thus assess whether the overall material properties and model yield the expected magnitude of response. If each frame size is matched well, then the overall properties and model are essentially valid. The overall trend and sign across the frames of these cycles are validated using a cross correlation coefficient. The second step assesses the specific trend and profile of the dynamic response, which is what is processed for diagnostic analysis in DIET. It is thus critical this overall dynamic response shape matches well, even if magnitudes are not perfect. This combined method thus validates first the overall size of response, model structure, and material properties, and second, the dynamic trajectory from frame to frame for more specific validation.

4.4.1 Frame to frame radial displacement magnitude

DIET captures several images over one sinusoidal response cycle at different phase angles (0^o, 36^o, 72^o, 108^o, 144^o, 180^o, 216^o, 252^o, 288^o, 324^o) relative to the input motion, creating k=10 images per cycle. Over a phantom, one motion set includes ~15000 points on the surface multiplied by 10 time or phase points. However, the FE model mesh has 4200 surface points. For validation, the DIET motion set is reduced from ~15000 surface points to the nearest 4200 FE model mesh points, each of which are then compared over the k=10 time points.

Figure 4.5 shows how the frame to frame radial displacement for each of the resulting 4200 points is calculated for each k = 1…10 frame using:

$$\Delta r_l^k = \sqrt{(x_{(l,k-1)} - x_{(l,k)})^2 + (y_{(l,k-1)} - y_{(l,k)})^2 + (z_{(l,k-1)} - z_{(l,k)})^2} \quad (4.1)$$

Where Δr_l^k is the frame to frame radial displacement and $k = 1 \ldots 10$ are number of frames and l = 1…4200 are number of points. The overall average values over all k = 10 frames are also compared:

$$\overline{\Delta r_l} = \frac{1}{10}\sum_{k=1}^{10} \Delta r_l^k \quad (4.2)$$

For the first validation, experimental phantom and model responses are compared at each of these 4200 surface points.

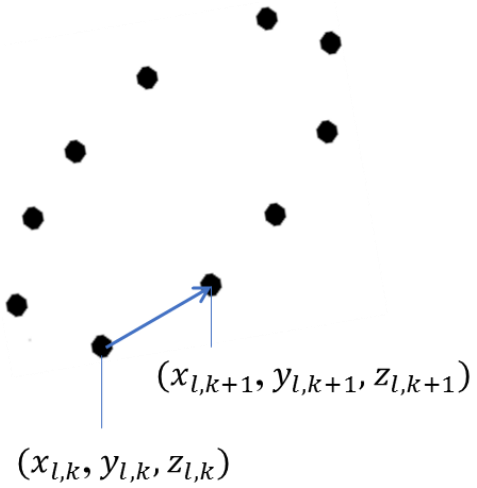

Figure 4.5: Frame to frame displacement for each of the $\boldsymbol{l}$ = 1…4200 surface points

4.4.2 Cross correlation and accuracy of the dynamic trajectory

For the second validation, the cross correlation coefficient is used to validate the similarity of dynamic trajectory across both data sets. All cross correlation coefficients range from -1.0 to +1.0. A correlation coefficient of +/- 1.0 indicates a perfect correlation or inverse correlation between the two variables, and thus both variables increase and decrease together or oppositely, perfectly. A correlation coefficient of 0.0 indicates zero correlation, or no relationship, between the two variables.

The vectors $\overrightarrow{\Delta r_l}$ across all k = 1…10 frames for experiment and FE model are compared, for all l = 1…4200 surface points, where the $\overrightarrow{\Delta r_l}$ vectors are defined for both experiment and FE model from Equation (4.2). Thus, $\overrightarrow{\Delta r_l}$ (exp or FEM) $= [\Delta r_l^1, \Delta r_l^2 \ldots \Delta r_l^{10}]$, where the $\overrightarrow{\Delta r}$ vectors are defined for both experiment and FE model.

The zero lag cross correlation, x of $\overrightarrow{\Delta r_l}$ (exp and FEM) used here is defined:

$$x = \frac{\overrightarrow{\Delta r_l}\,(\exp) \cdot \overrightarrow{\Delta r_l}\,(FEM)}{\|\Delta r_l(\exp)\|\|\Delta r_l(FEM)\|} \tag{4.3}$$

Where $\overrightarrow{\Delta r_l}\ (\exp) \cdot \overrightarrow{\Delta r_l}\ (\mathrm{FEM})$ is the inner or dot product, and $\|\Delta r_l(\exp)\|\|\Delta r_l(FEM)\|$ is the z-norm magnitude of the vector.

4.5 Summary

The geometry of the model is constructed from fabricated phantoms, and its mechanical properties were used from previous Chapter 3. This method allows the breast to capture surface motion at frequency ranges from 16 Hz to 50 Hz. In this chapter, from DIET frequencies range only three middle frequencies 28 Hz, 30 Hz, and 32 Hz are used as inputs to the beast shaped phantom modeled. Mesh convergence studies were performed to ensure that the numerical errors in the approximation were minimized. The analysis results are presented in chapter 5.

Chapter 5: Validation of finite element modelling with DIET experimental data of breast shaped phantom

In this chapter, the FE models from Chapter 4 are simulated and compared to DIET experimental data at three different frequencies, 28 Hz, 30 Hz and 32 Hz. The two described validation procedures; a frame to frame radial displacement magnitude and a cross correlation coefficient methods for over 4000 surface points with total of 10 number of frames on each model a healthy (no inclusion), 10 mm inclusion and 20 mm inclusion from Chapter 4 has been used in this chapter.

5.1 Introduction

This chapter presents the validation of finite element model approach to analyze breast shaped silicone phantoms with and without stiffer inclusions used to mimic cancerous lesions. A novel biomechanical and application-motivated model validation methodology is presented. This method is based on surface displacements of the breast phantom, which are the key to the diagnostic metrics in the DIET concept. In particular, validation focuses on the requirement for this model to capture the dynamic, steady state response at all phases of the sinusoidal response, rather than just matching amplitudes. This approach captures the need for any in silico, model replacement of phantoms to capture the complete behavior of the real system.

5.2 Frame to frame radial displacement magnitude validation

Figures 5.1-5.9 show frame to frame validation results for each of the k = 1 … 10, FE and DIET radial displacement frames(Δr_i^k). The maximum displacement on the color bars was fixed to 0.5 mm matching the positive peak amplitude of the 28 Hz, 30Hz and 32 Hz input sine waves. All figures show larger displacements by the actuator and smaller to zero at the chest wall, as expected, given the boundary conditions.

Figures 5.1-5.3 show the displacement comparison for the healthy phantom at 28 Hz, 30 Hz and 32 Hz, respectively. Because the phantom is homogenous with no inclusion, the displacement is evenly distributed. The displacement near the actuator is high is due to input sine wave was applied on the actuator. Additionally, a fixed boundary condition was applied on the top of chest wall. Therefore, the displacement distribution should be zero at these points.

Figures 5.4-5.6 show the displacements for the 10 mm inclusion phantom. Because the changes in surface displacement are smaller, it is harder to see a difference between the region where the 10 mm inclusion is located and the surrounding tissues. Thus, it cannot be detected in this fashion, although advanced processing does detect it [30].

Similarly, Figures 5.7-5.9 show the displacement comparison for the phantom with a 20 mm inclusion at 28 Hz, 30 Hz and 32 Hz. Tissue stiffness plays an important role for diagnosis of breast cancers in this DIET concept, as inclusions are 4-10 times stiffer than the surrounding breast tissues [270] as discussed in Chapter 3. The tissue displacements are inversely proportional to the stiffness of the tissue, and thus a stiffer region of tissue exhibits smaller displacements than a more compliant region, all else equal [27, 28]. Figures 5.7-5.9 indicates the position of the 20 mm inclusion with a black circle. Again, qualitatively the match is good, but there are small local differences in magnitude due to imperfect match of experimental phantom and model stiffness or damping properties, or other modelling errors. However, the frame to frame magnitudes qualitatively match well. As with Figures 5.4-5.9, the trends and overall qualitative comparison are acceptably clase.

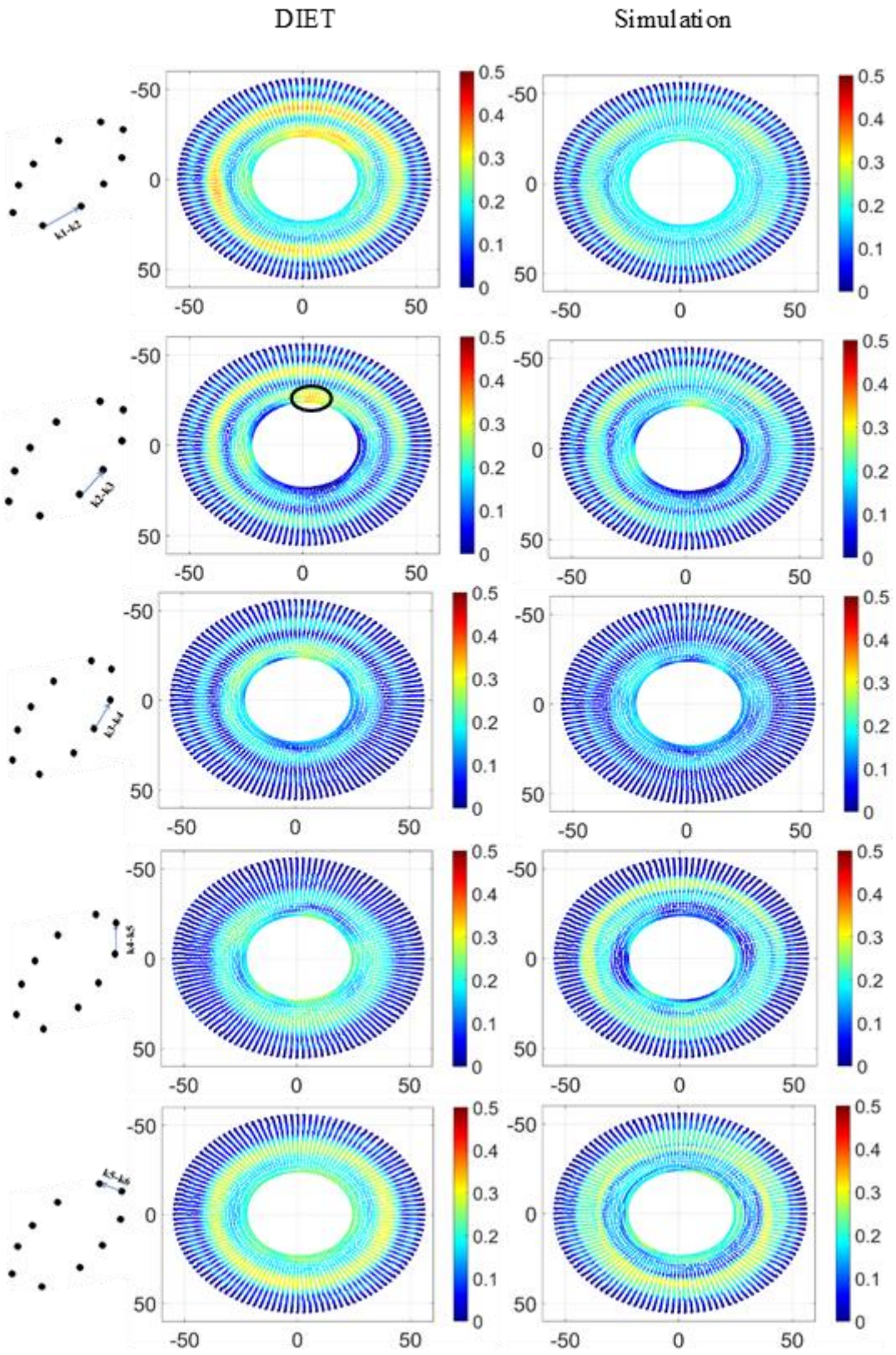
DIET
Simulation
-50
0
50
0.5
0.4
0.3
0.2
0.1
0

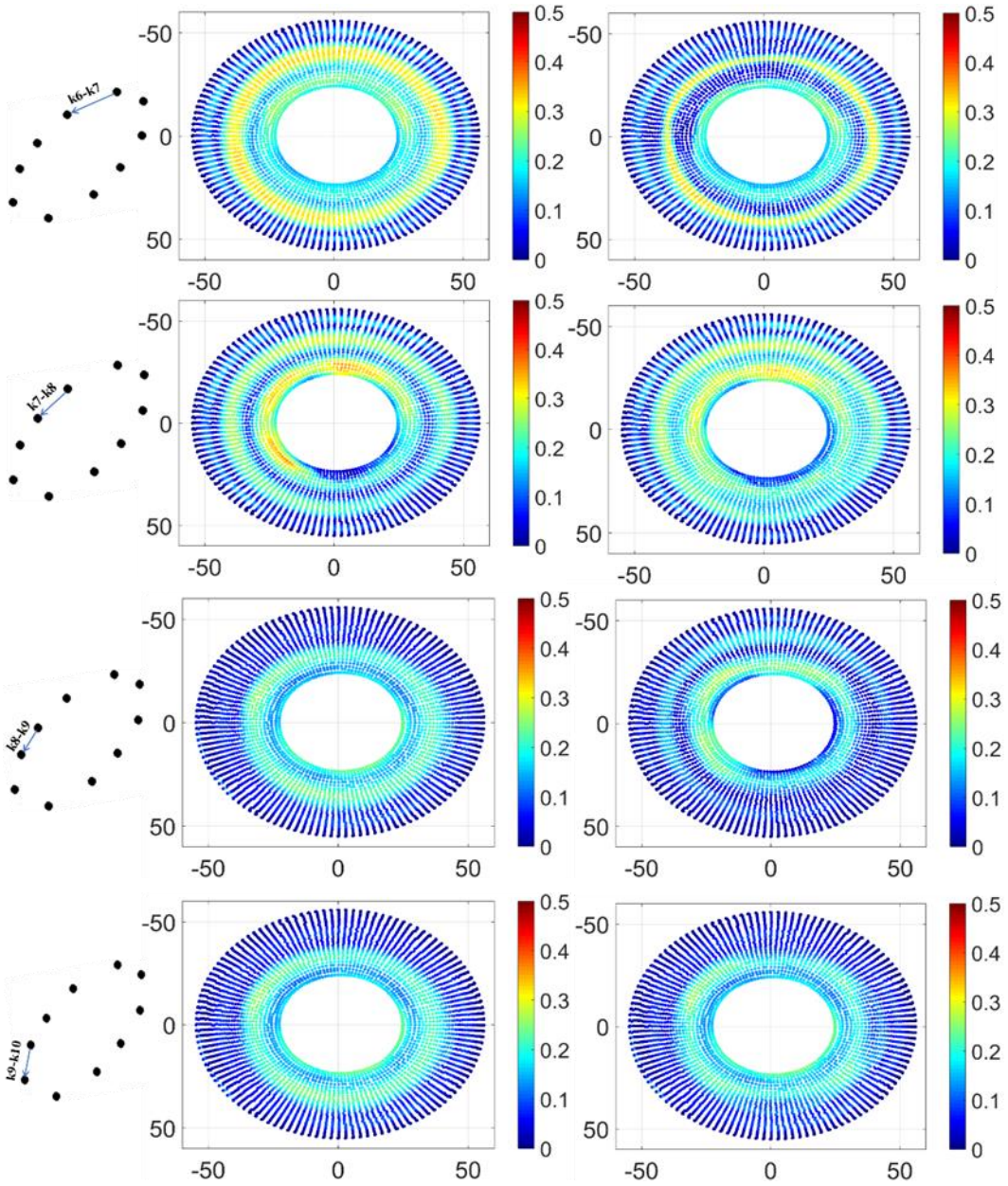

Figure 5.1: Displacement distribution (all units in mm) of healthy phantom at 28 Hz for experimental DIET (left) and FE model (right) for the k=1…10 frames captured (top-bottom) - displacement distribution from frame 2 to 3 near the actutor is uneven, indicated by a black circle, leading to some loss of symmetry

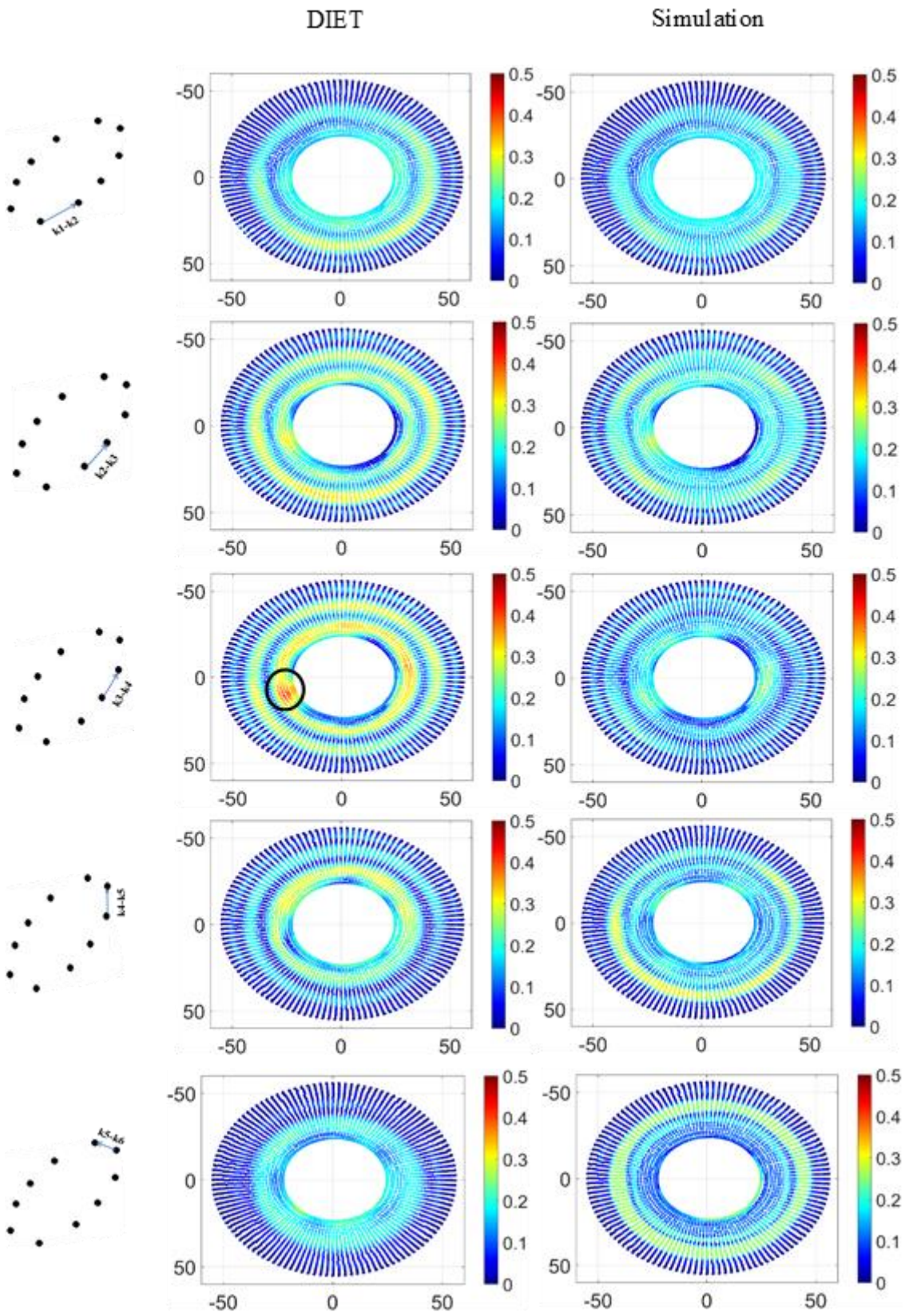
DIET
Simulation
k1-k2
k2-k3
k3-k4
k4-k5
k5-k6
-50
0
50
0.5
0.4
0.3
0.2
0.1
0

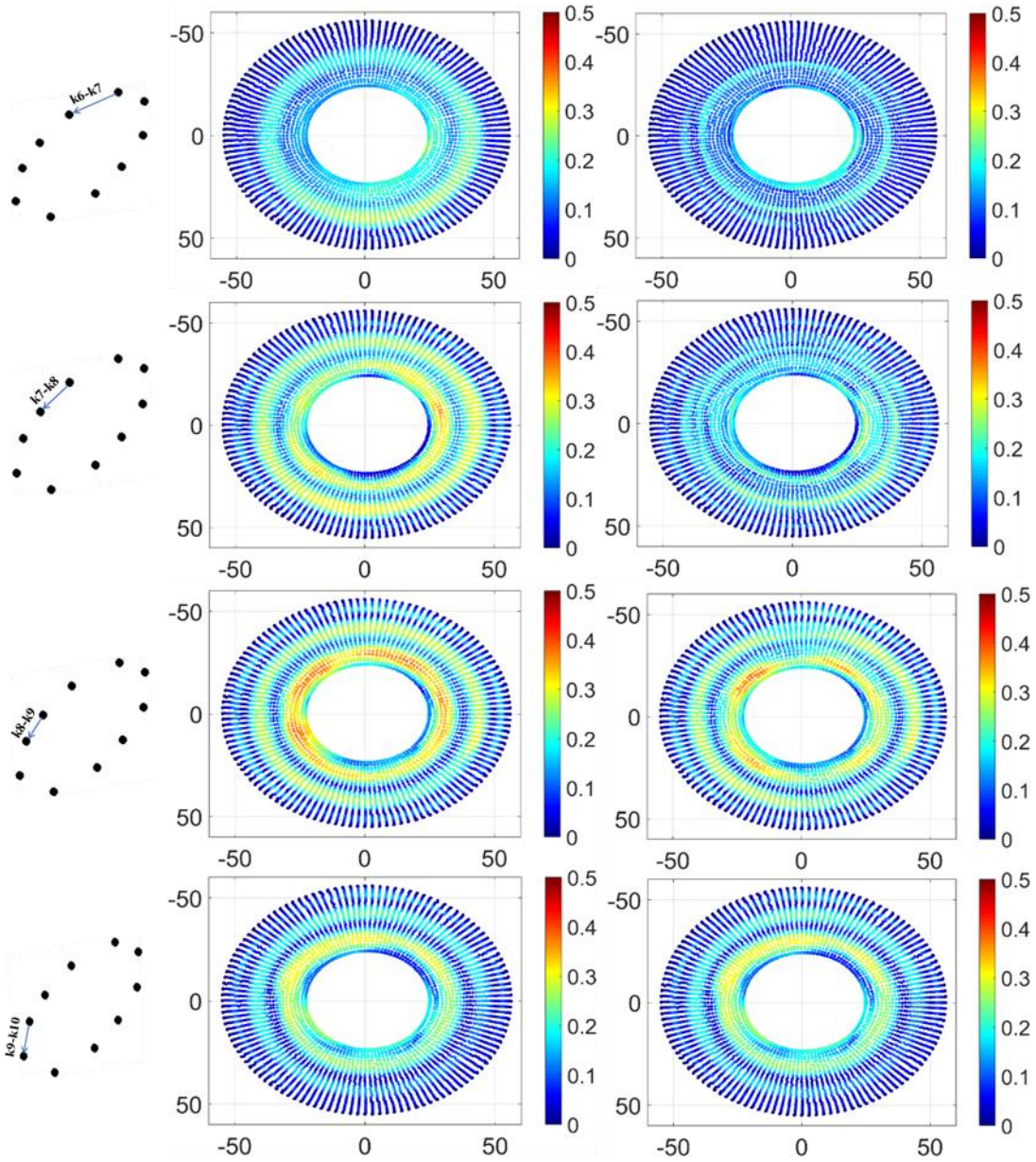

Figure 5.2: Displacement distribution (all units in mm) of healthy phantom at 30 Hz for experimental DIET (left) and FE model (right) for the k=1…10 frames captured (top-bottom) - displacement distribution from frame 3 to 4 near the actutor is uneven, indicated by a black circle, leading to some loss of symmetry

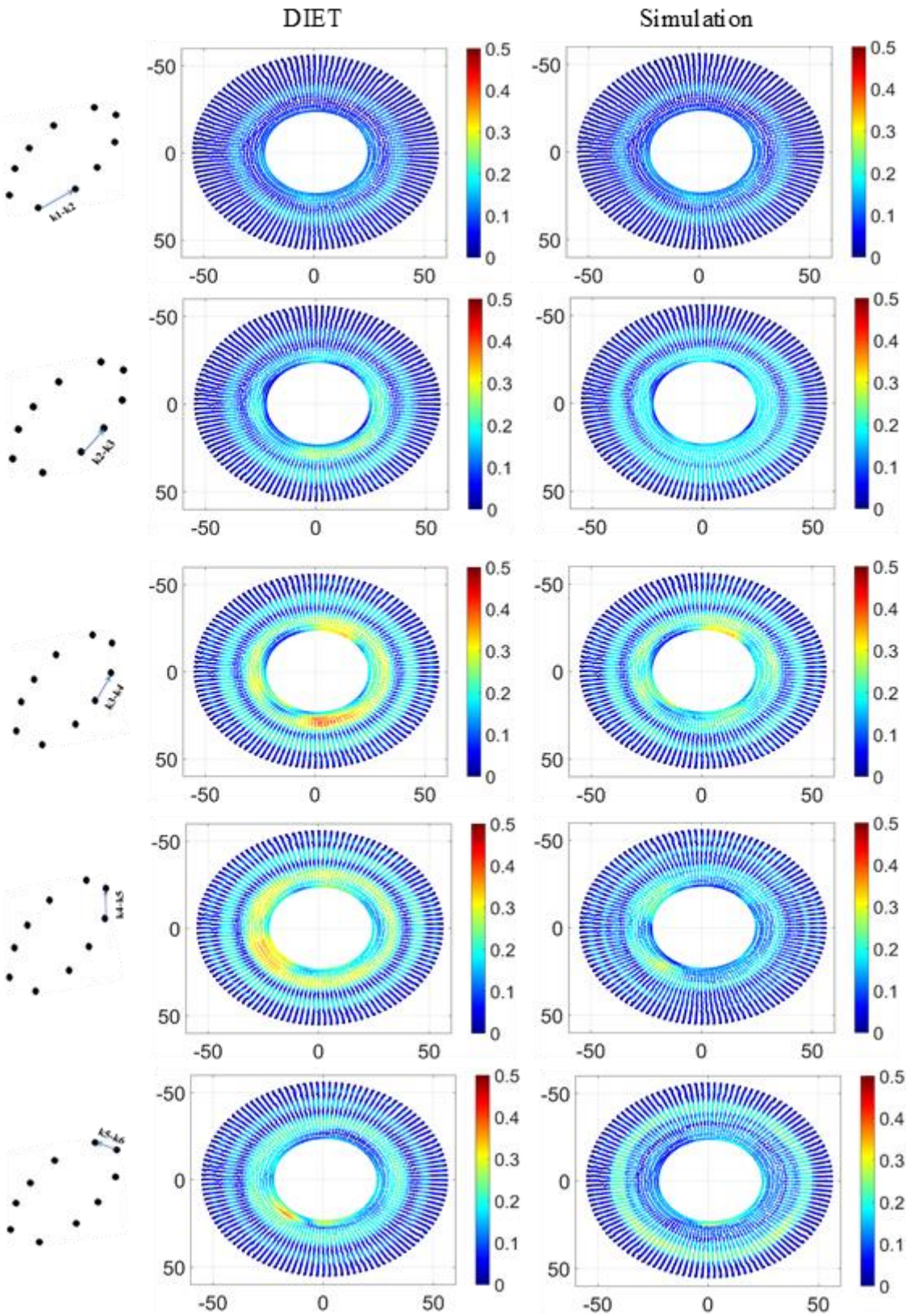
DIET
Simulation
-50
0
50
0.5
0.4
0.3
0.2
0.1
0

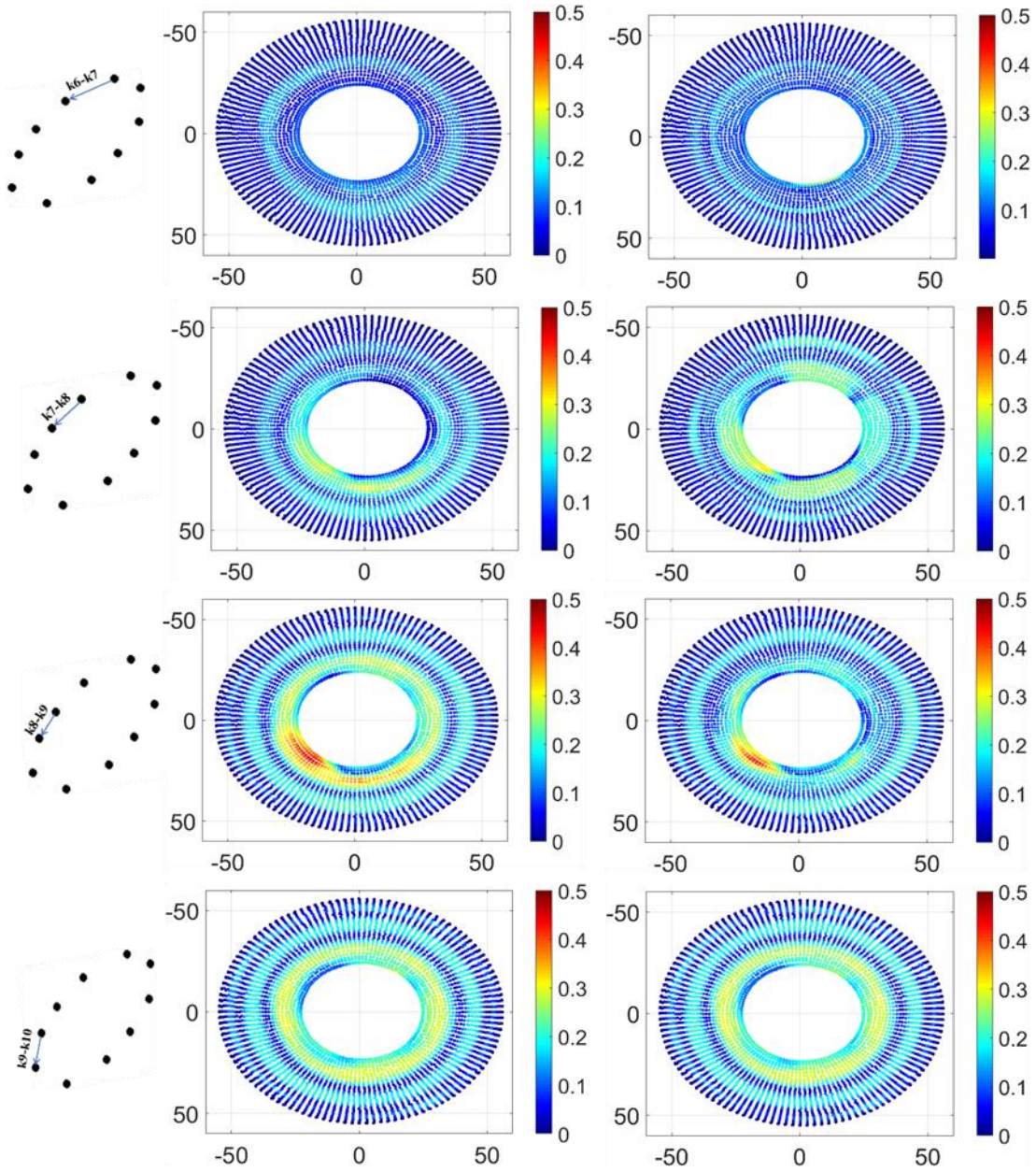

Figure 5.3: Displacement distribution (all units in mm) of healthy phantom at 32 Hz for experimental DIET (left) and FE model (right) for the k=1…10 frames captured (top-bottom)

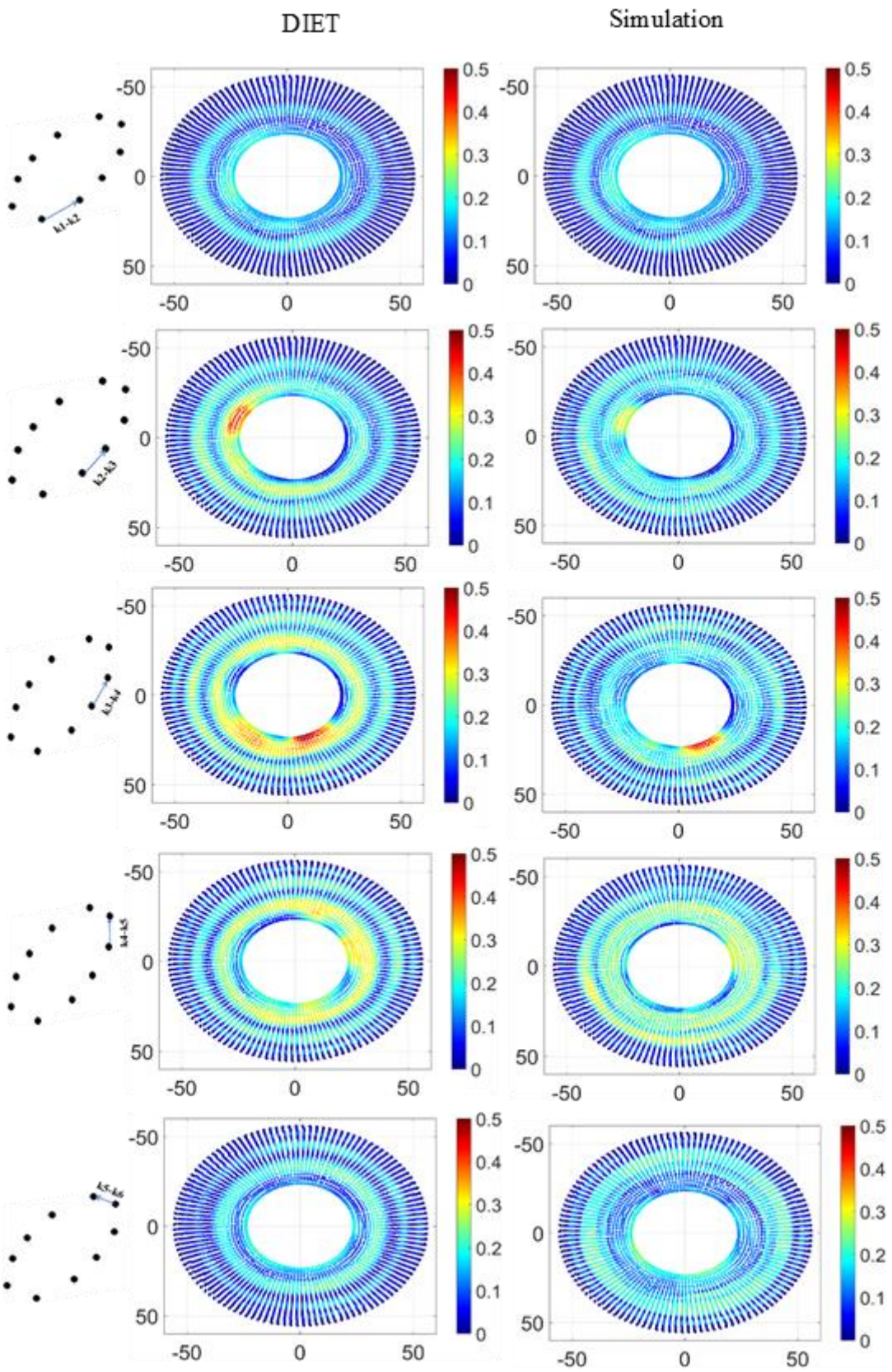
DIET
Simulation
k1-k2
k2-k3
k3-k4
k4-k5
k5-k6
-50
0
50
0.5
0.4
0.3
0.2
0.1
0

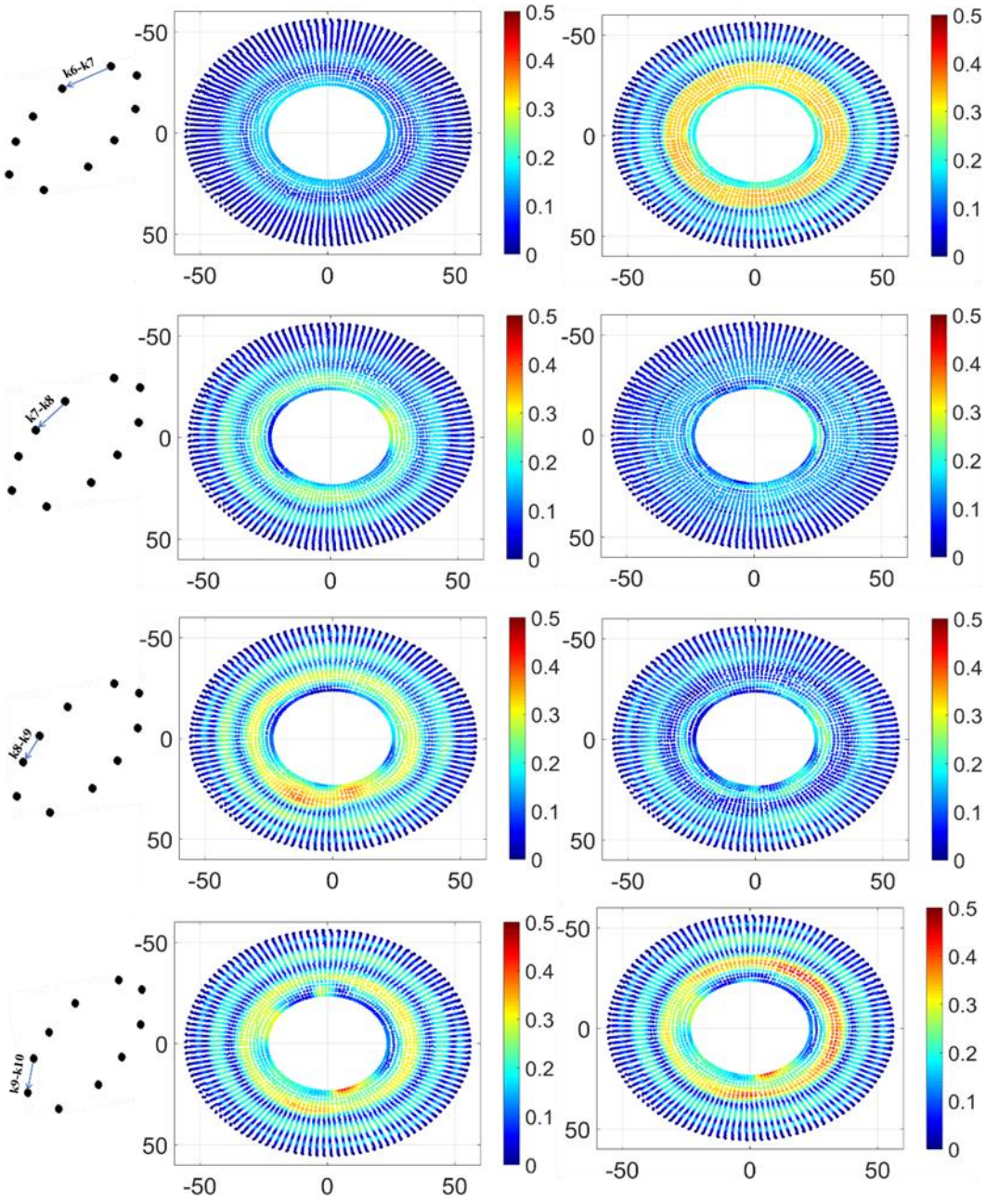

Figure 5.4: Displacement distribution (all units in mm) of 10 mm inclusion phantom at 28 Hz for experimental DIET (left) and FE model (right) for the k=1…10 frames captured (top-bottom)

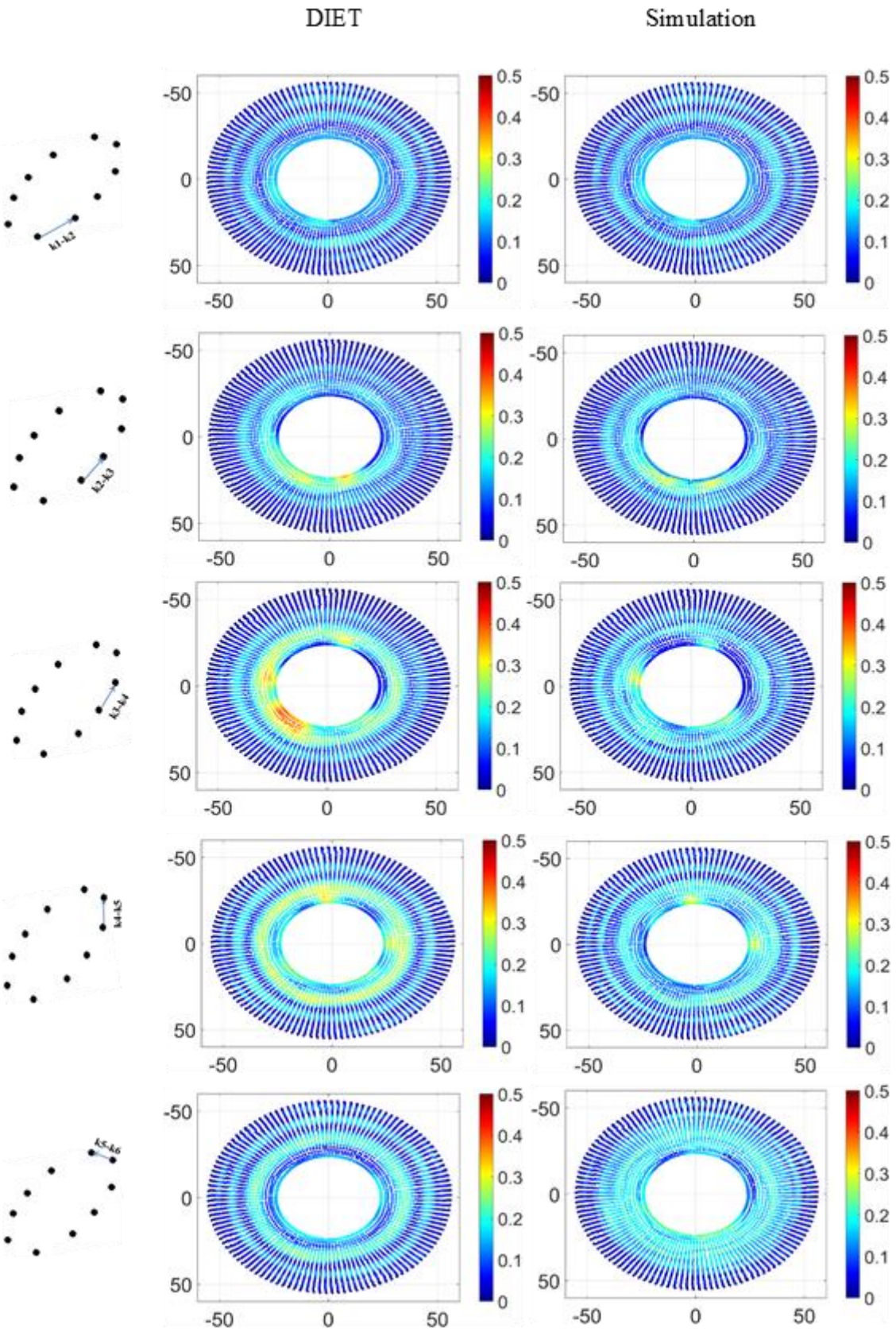
DIET
Simulation
k1-k2
k2-k3
k3-k4
k4-k5
k5-k6
-50
0
50
0.5
0.4
0.3
0.2
0.1
0

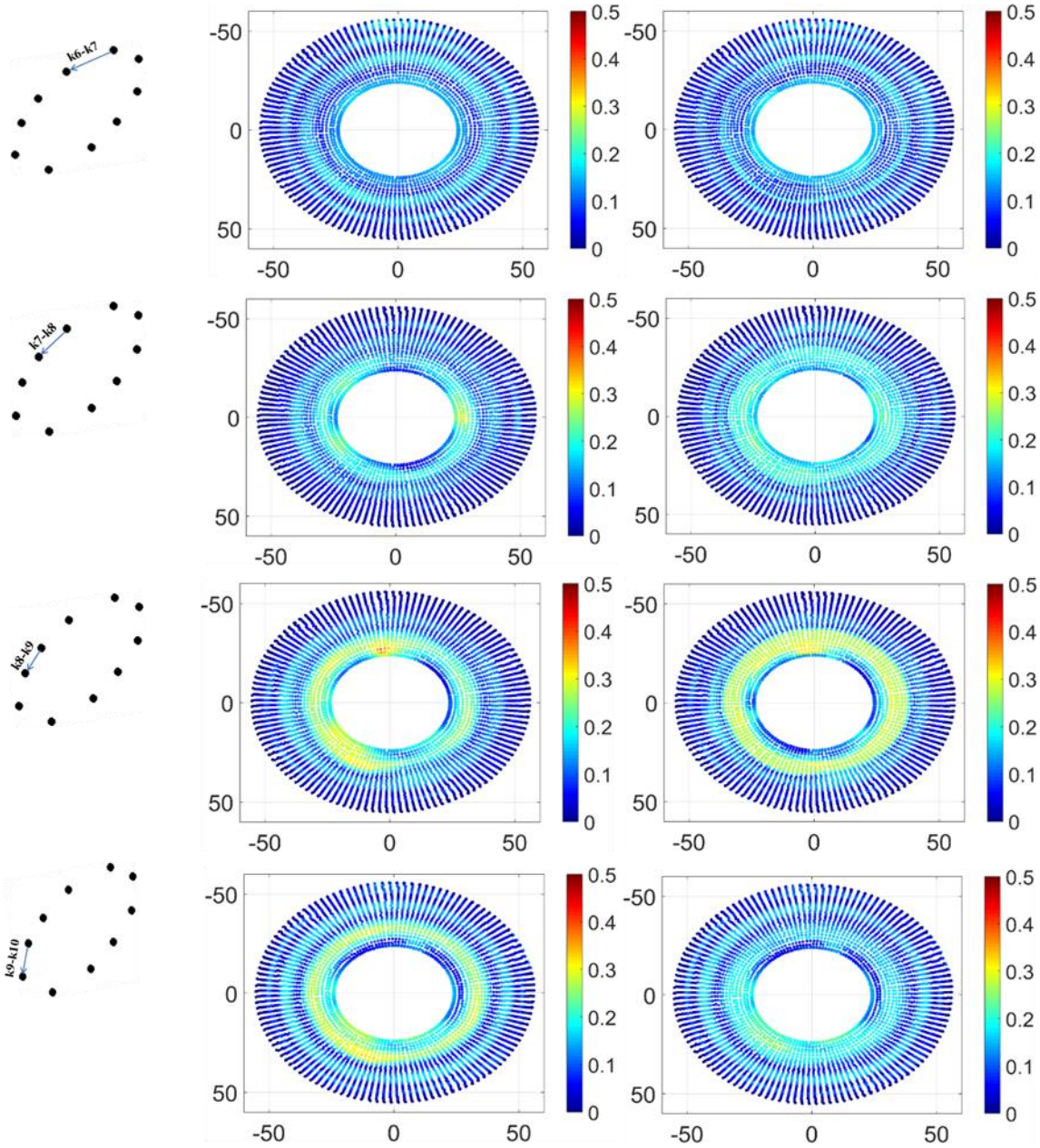

Figure 5.5: Displacement distribution (all units in mm) of 10 mm inclusion phantom at 30 Hz for experimental DIET (left) and FE model (right) for the k=1…10 frames captured (top-bottom)

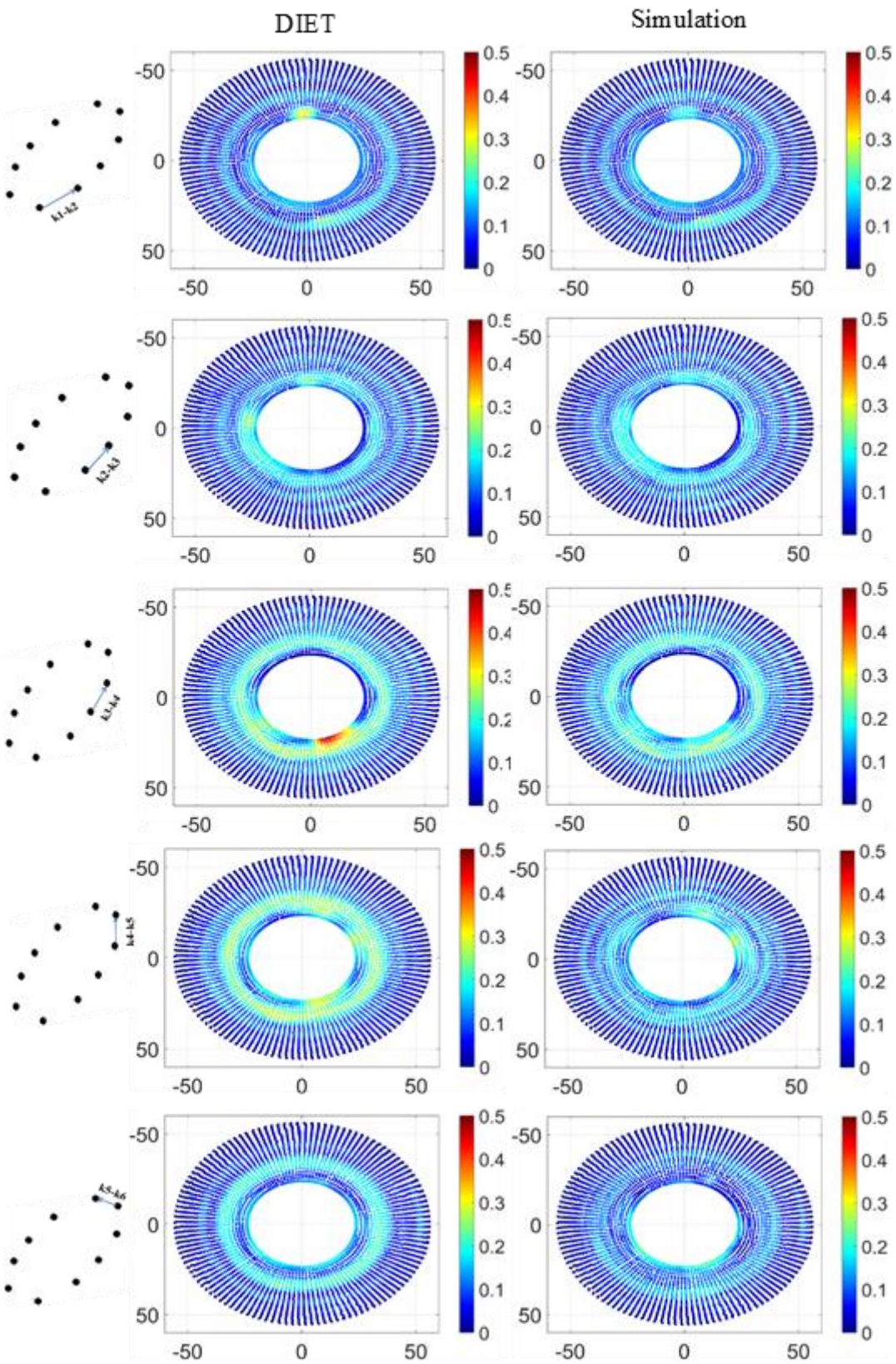
DIET
Simulation
-50
0
50
0.5
0.4
0.3
0.2
0.1
0

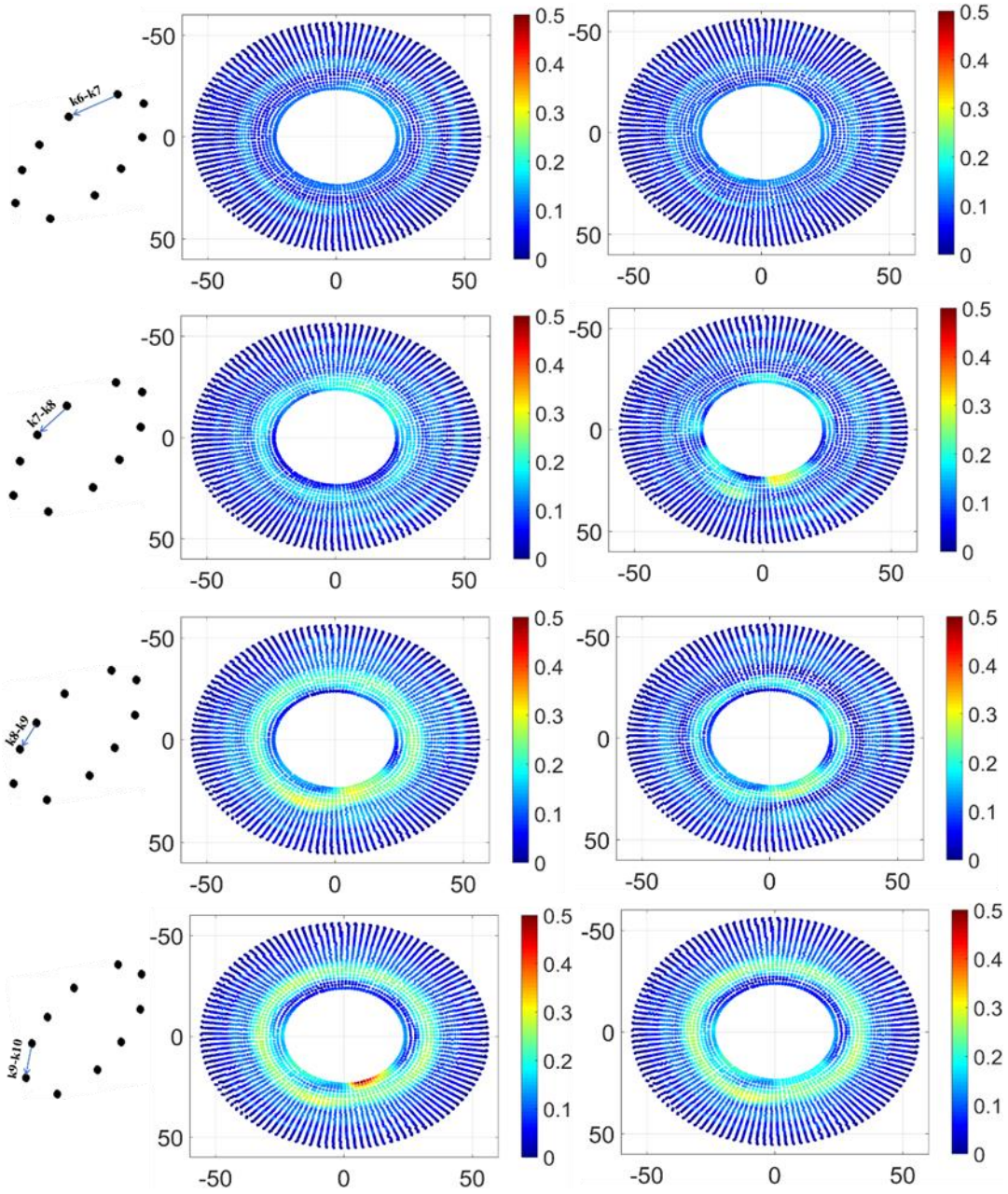

Figure 5.6: Displacement distribution (all units in mm) of 10 mm inclusion phantom at 32 Hz for experimental DIET (left) and FE model (right) for the k=1…10 frames captured (top-bottom)

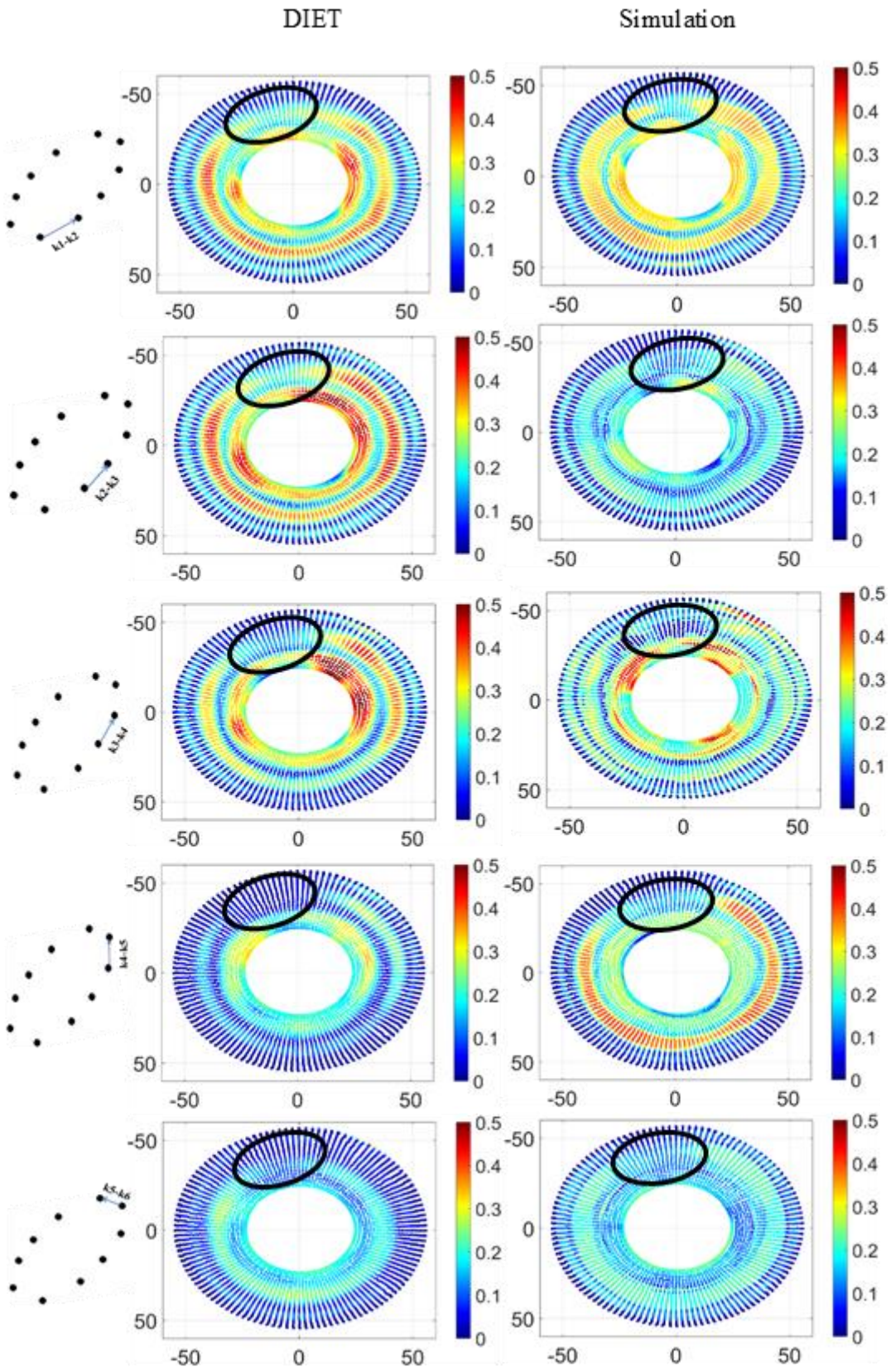
DIET
Simulation
k1-k2
k2-k3
k3-k4
k4-k5
k5-k6
-50
0
50
0.5
0.4
0.3
0.2
0.1
0

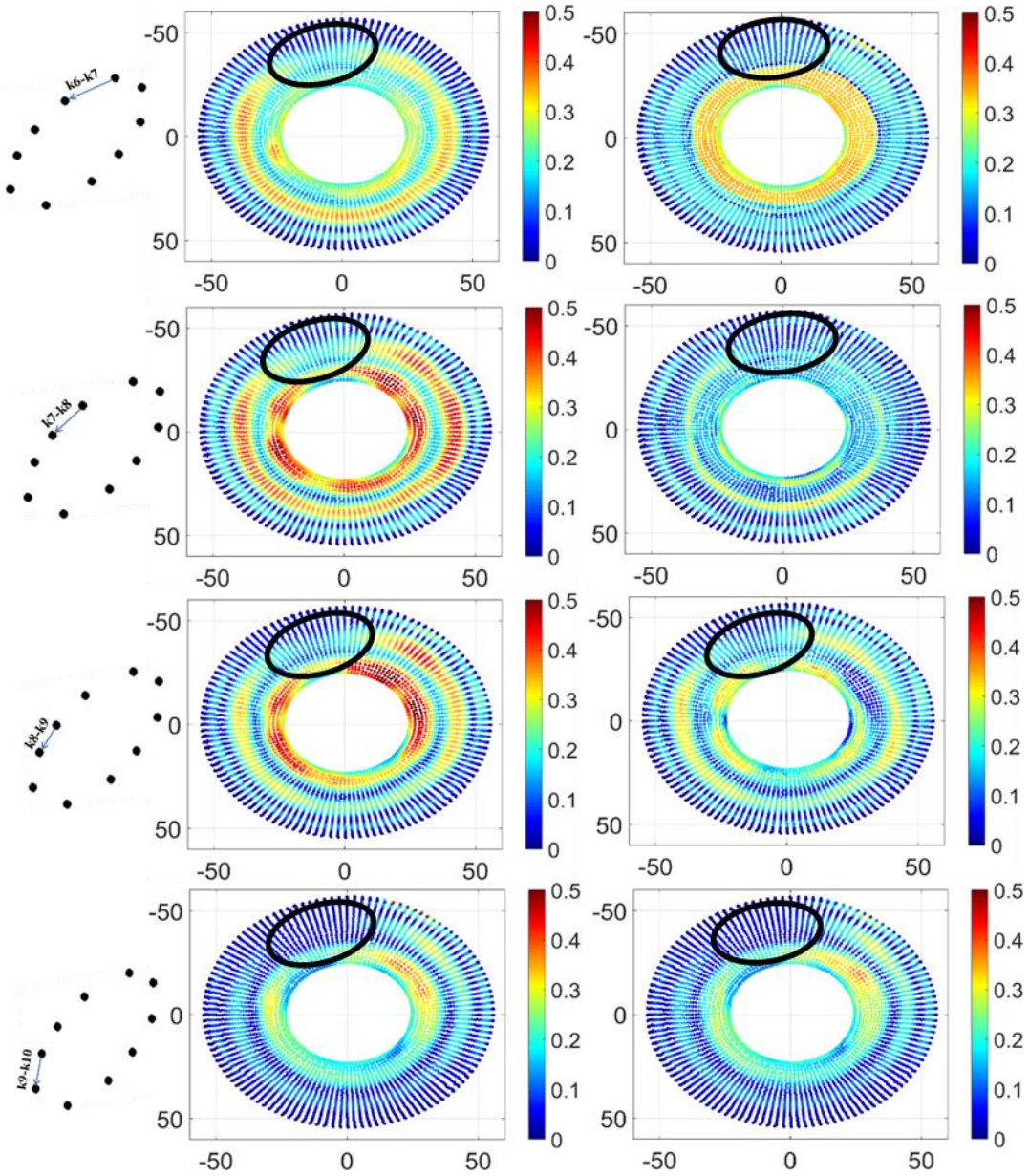

Figure 5.7: Displacement distribution (all units in mm) of 20 mm inclusion phantom at 28 Hz for experimental DIET (left) and FE model (right) for the k=1…10 frames captured (top-bottom) position of 20 mm inclusion indicated with a black circle

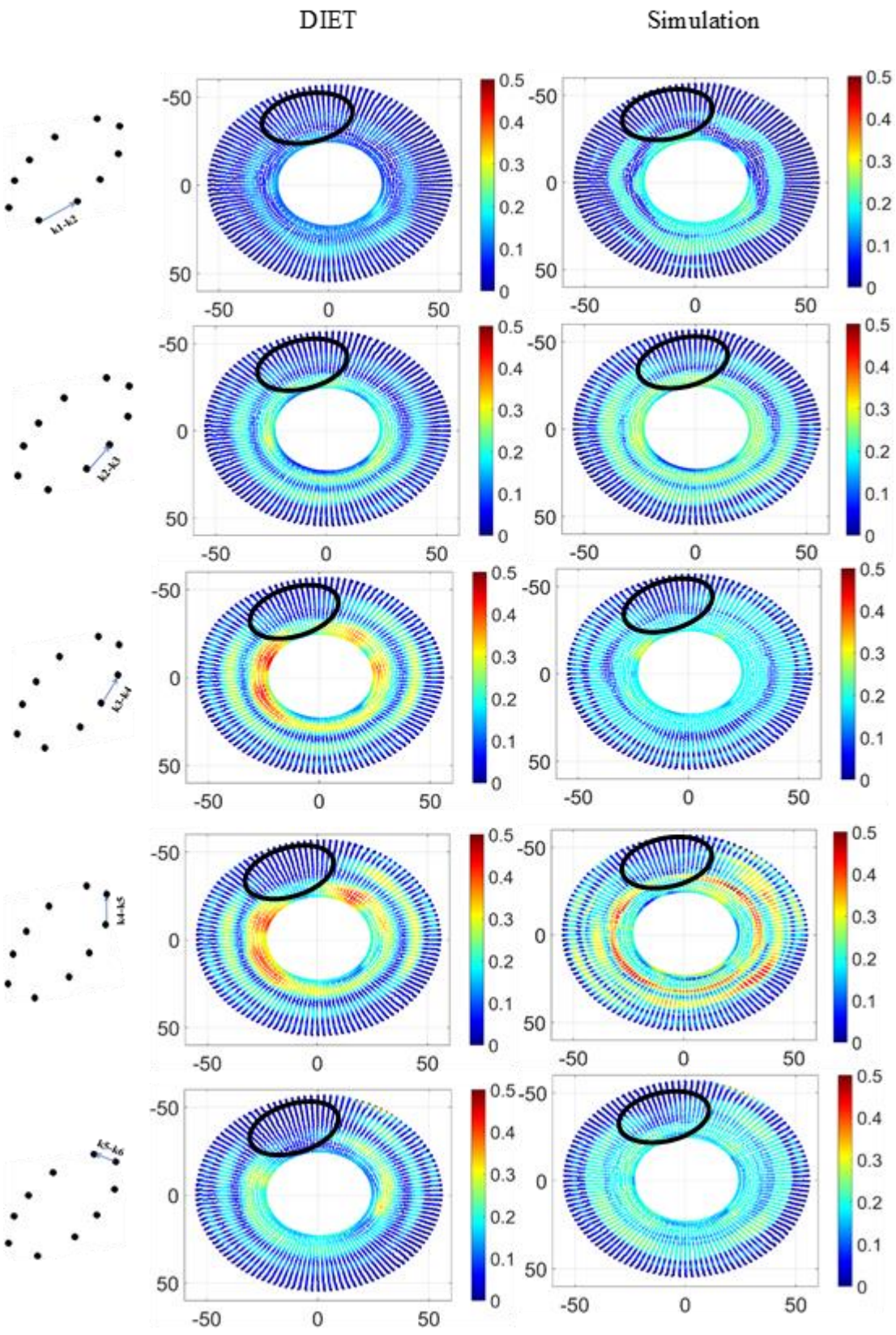
DIET
Simulation
k1-k2
k2-k3
k3-k4
k4-k5
k5-k6
-50
0
50
0.5
0.4
0.3
0.2
0.1
0

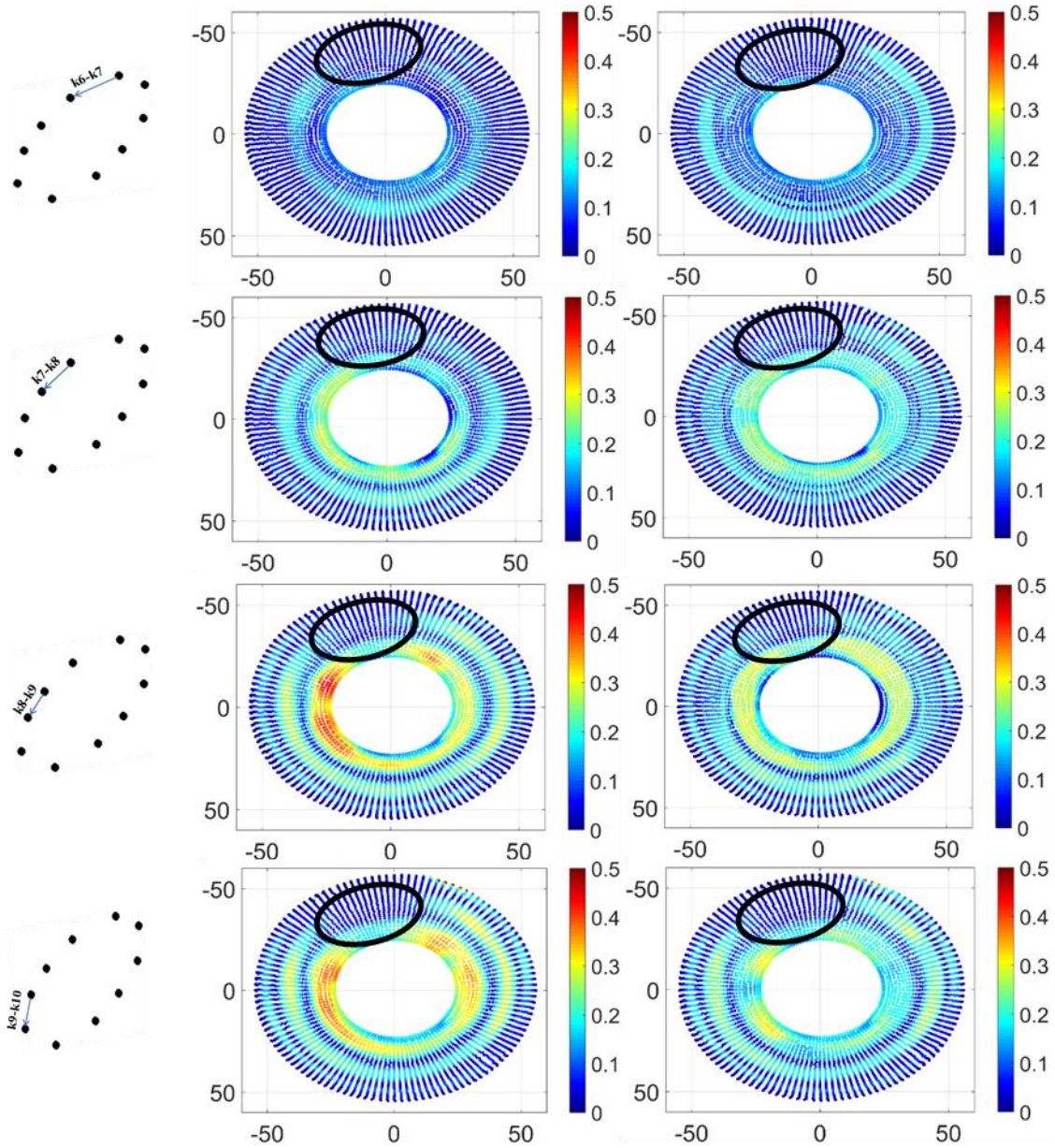

Figure 5.8: Displacement distribution (all units in mm) of 20 mm inclusion phantom at 30 Hz for experimental DIET (left) and FE model (right) for the k=1…10 frames captured (top-bottom) position of 20 mm inclusion indicated with a black circle

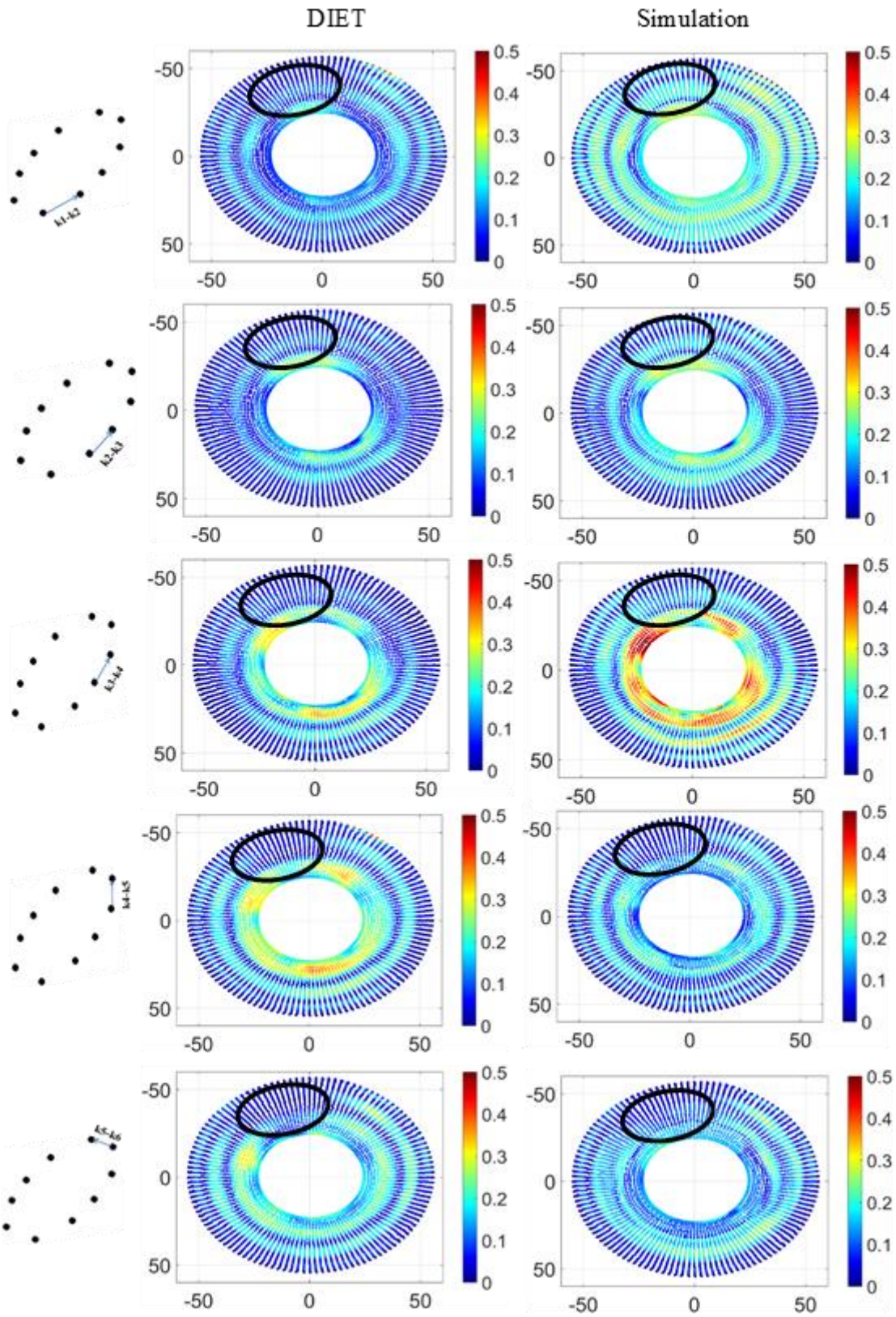
DIET
Simulation
k1-k2
k2-k3
k3-k4
k4-k5
k5-k6
-50
0
50
0.5
0.4
0.3
0.2
0.1
0

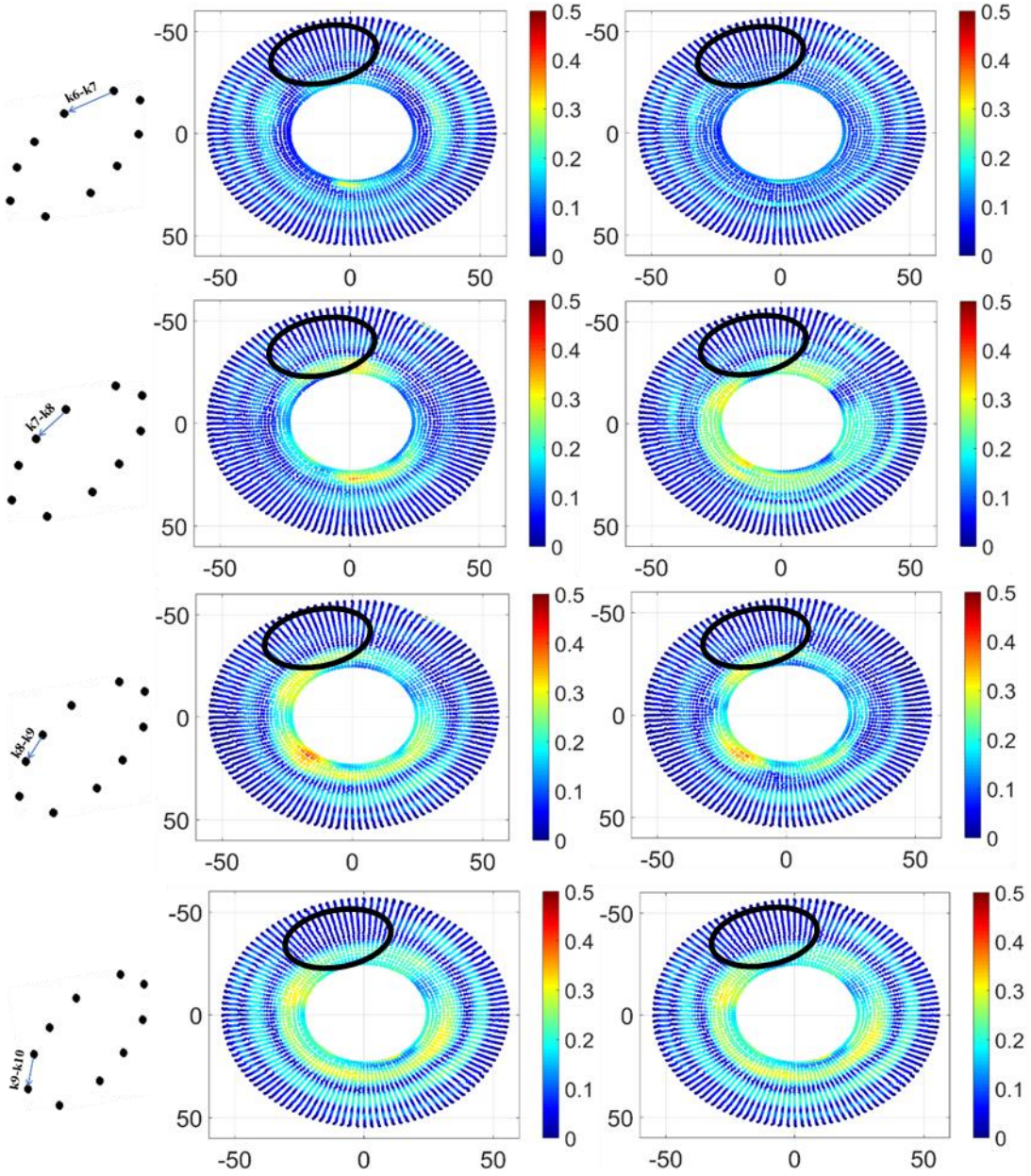

Figure 5.9: Displacement distribution (all units in mm) of 20 mm inclusion phantom at 32 Hz for experimental DIET (left) and FE model (right) for the k=1…10 frames captured (top-bottom) position of 20 mm inclusion indicated with a black circle

Figures 5.10-5.12 show the average radial displacement at 28 Hz, 30 Hz and 32 Hz of each node on the phantom surface ($\overline{\Delta r_l}$) to locate the 10 mm and 20 mm inclusion with a black circle. The average radial displacement reduces with the increasing frequency enabling the location of inclusions. Figures 5.10-5.12 show a stronger overall match between DIET

experimental and FE model results, as well as in motion amplitudes (average radial displacement), where all k= 1…10 frames are considered.

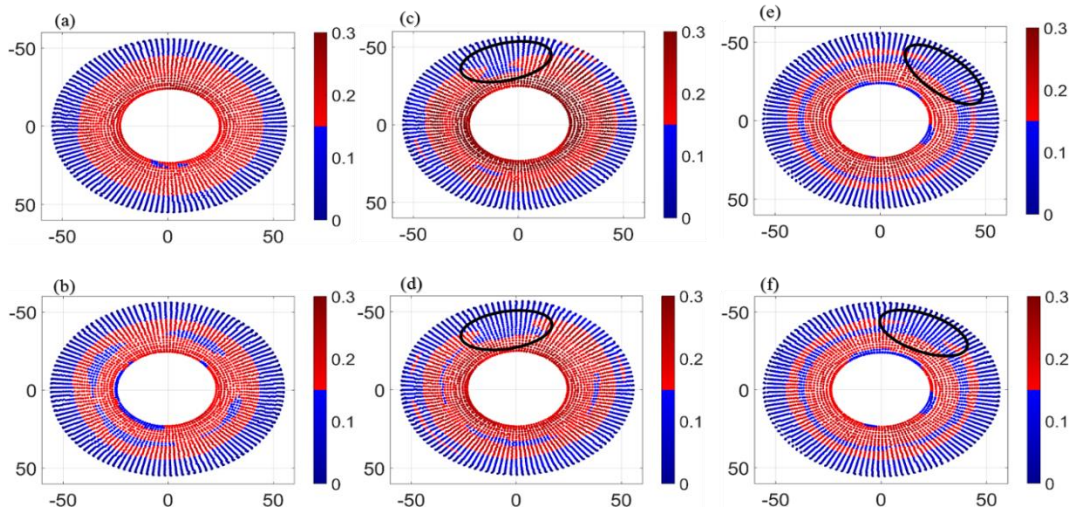

Figure 5.10: Average radial displacement distribution (all units in mm) for 28 Hz frequency (a) DIET Healthy phantom, (b) Finite element analysis (FEA) Healthy phantom, (c) DIET 20 mm inclusion position indicated with a black circle, (d) FEA 20 mm inclusion position indicated with a black circle, (e) DIET 10 mm inclusion position indicated with a black circle and (f) FEA 10 mm inclusion position indicated with a black circle

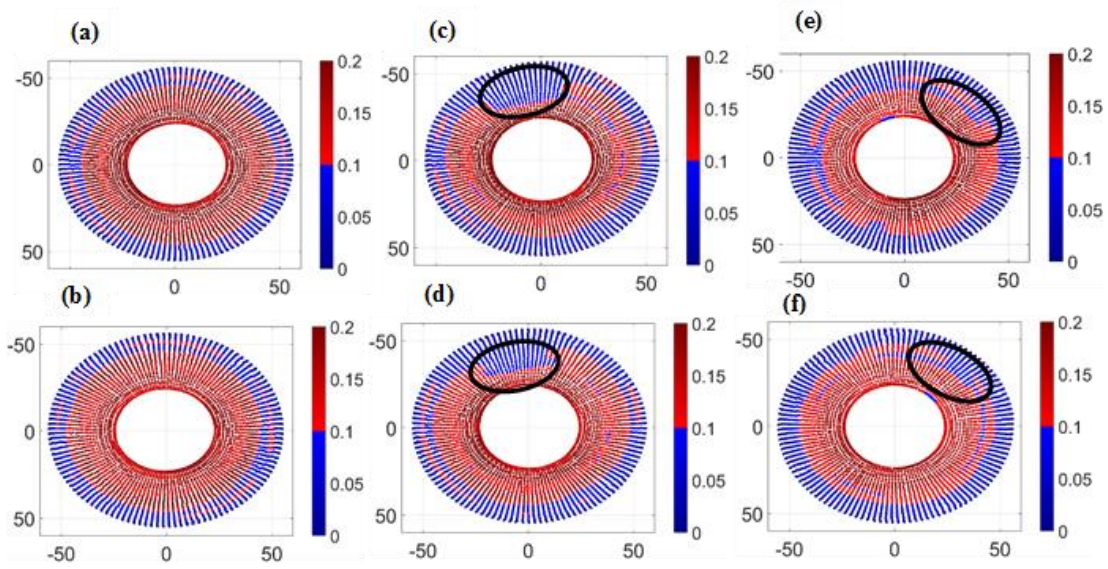

Figure 5.11: Average radial displacement distribution (all units in mm) for 30 Hz frequency (a) DIET Healthy phantom, (b) Finite element analysis (FEA) Healthy phantom, (c) DIET 20 mm inclusion position indicated with a black circle, (d) FEA 20 mm inclusion position indicated with a black circle, (e) DIET 10 mm inclusion position indicated with a black circle and (f) FEA 10 mm inclusion position indicated with a black circle

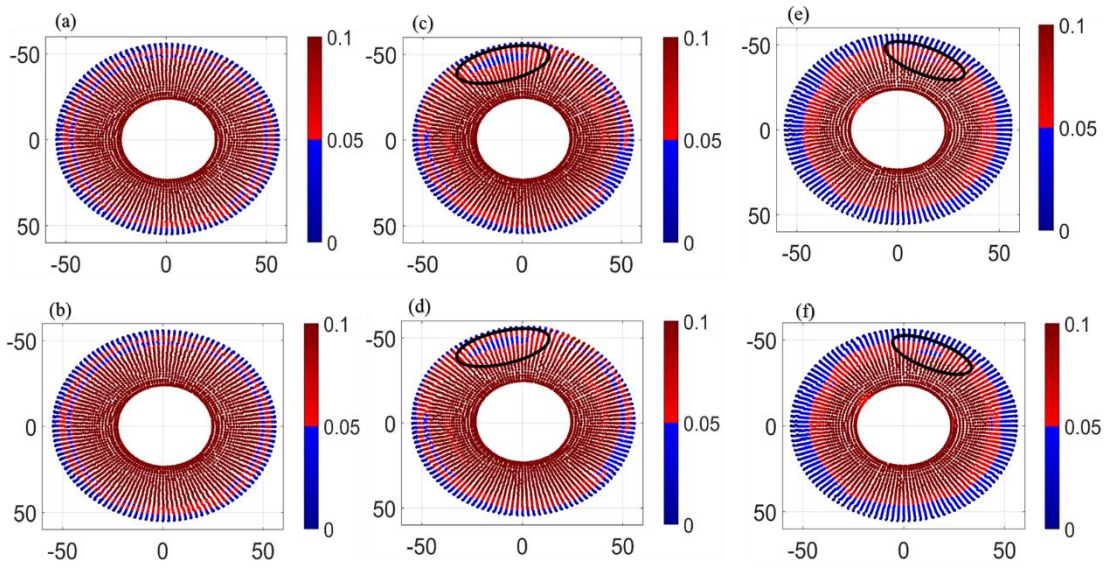

Figure 5.12: Average radial displacement distribution (all units in mm) for 32 Hz frequency (a) DIET Healthy phantom, (b) Finite element analysis (FEA) Healthy phantom, (c) DIET 20 mm inclusion position indicated with a black circle, (d) FEA 20 mm inclusion position indicated with a black circle, (e) DIET 10 mm inclusion position indicated with a black circle and (f) FEA 10 mm inclusion position indicated with a black circle

5.3 Accuracy of dynamic trajectory using cross correlation coefficient

The cross correlation coefficient for all 4200 surface points over all 10 frames at each frequency were calculated to analyse discrepancies in the trajectory of the dynamic response between FEA and DIET experimental results. It measures the degree to which both data sets vary in the same direction, or oppositely. It is thus a strong validation for DIET, which uses dynamic response over all frames as a diagnostic.

The resulting cumulative distribution functions for each phantom at 28 Hz, 30 Hz and 32 Hz of these values is shown in Figures 5.13-5.15. Tables 5.1-5.3 summarize these results. Over all frequencies more than 90% of points have a cross correlation coefficient, $x \geq 0.9$, indicating very good correlation at every frequency. Lower values are likely due to the

existence of many local effects not taken into account by the more homogenous finite element modelling. Finally, 99-100 % of values have > 0.8 which is still a very good correlation result.

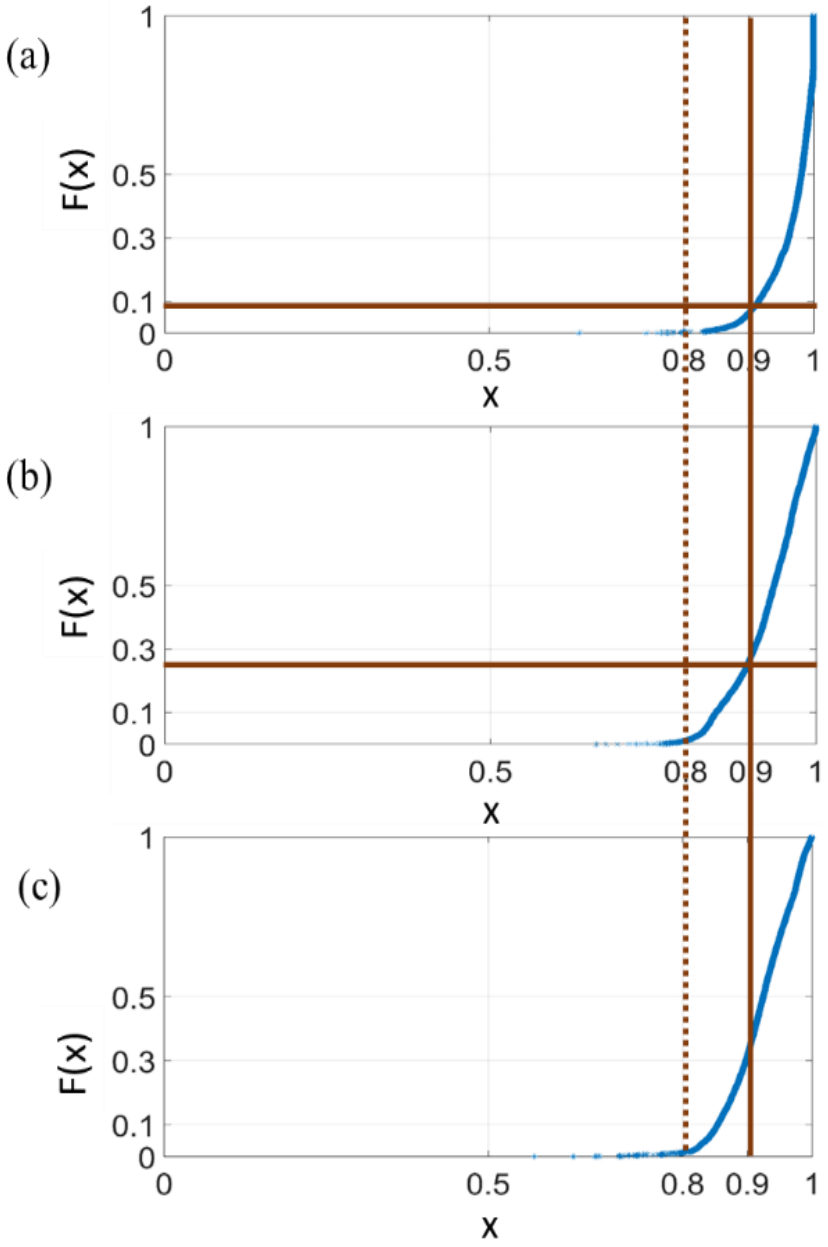

Figure 5.13: Empirical distribution (F(x)) of cross correlation coefficient (x) of all points at 28 Hz for: a) Healthy Phantom; b) 10 mm inclusion; and c) 20 mm inclusion. The solid lines show the x = 0.90 value and quantify its likelihood. The dashed line shows the location for , $\boldsymbol{x}$ = 0.80 with ~99-100 % of the values having , $\boldsymbol{x}$ ≥0.80

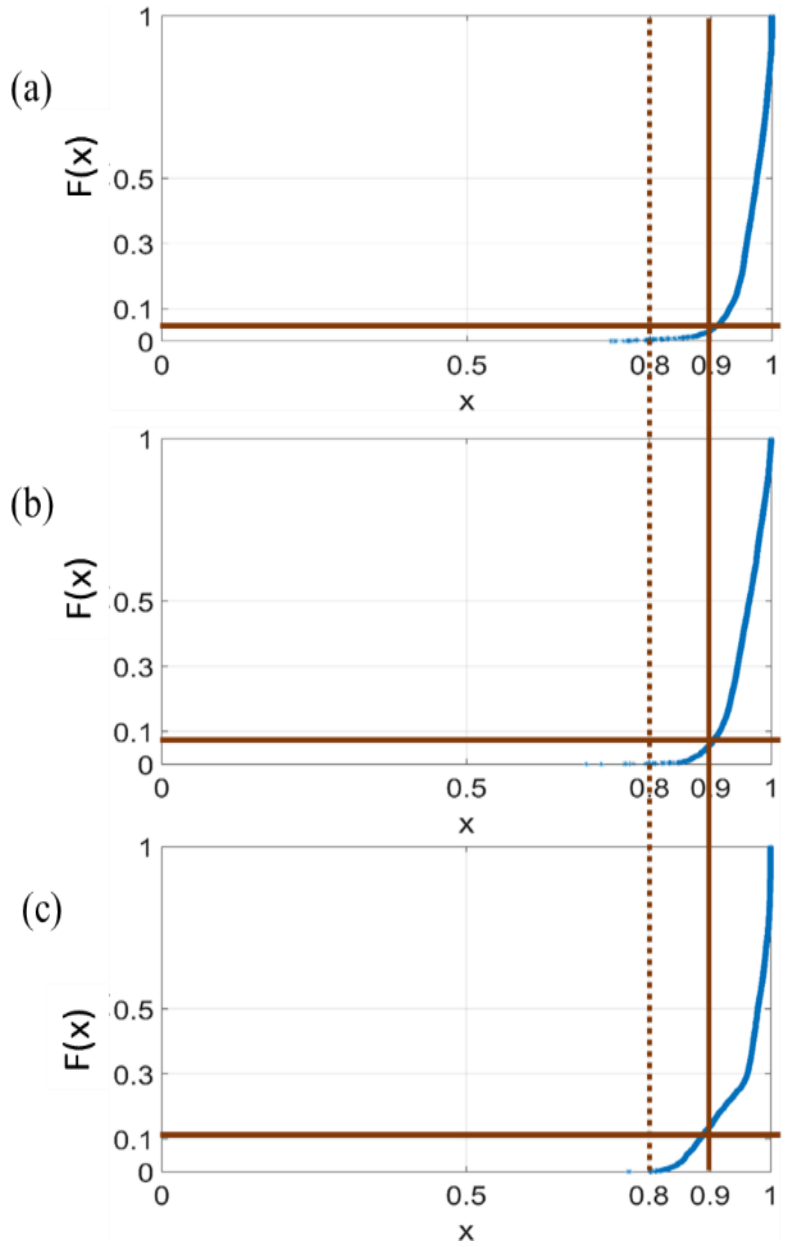

Figure 5.14: Empirical distribution (F(x)) of cross correlation coefficient (x) of all points at 30 Hz for: a) Healthy Phantom; b) 10 mm inclusion; and c) 20 mm inclusion. The solid lines show the x = 0.90 value and quantify its likelihood. The dashed line shows the location for , $\boldsymbol{x}$ = 0.80 with ~99-100 % of the values having , $\boldsymbol{x}$ ≥0.80

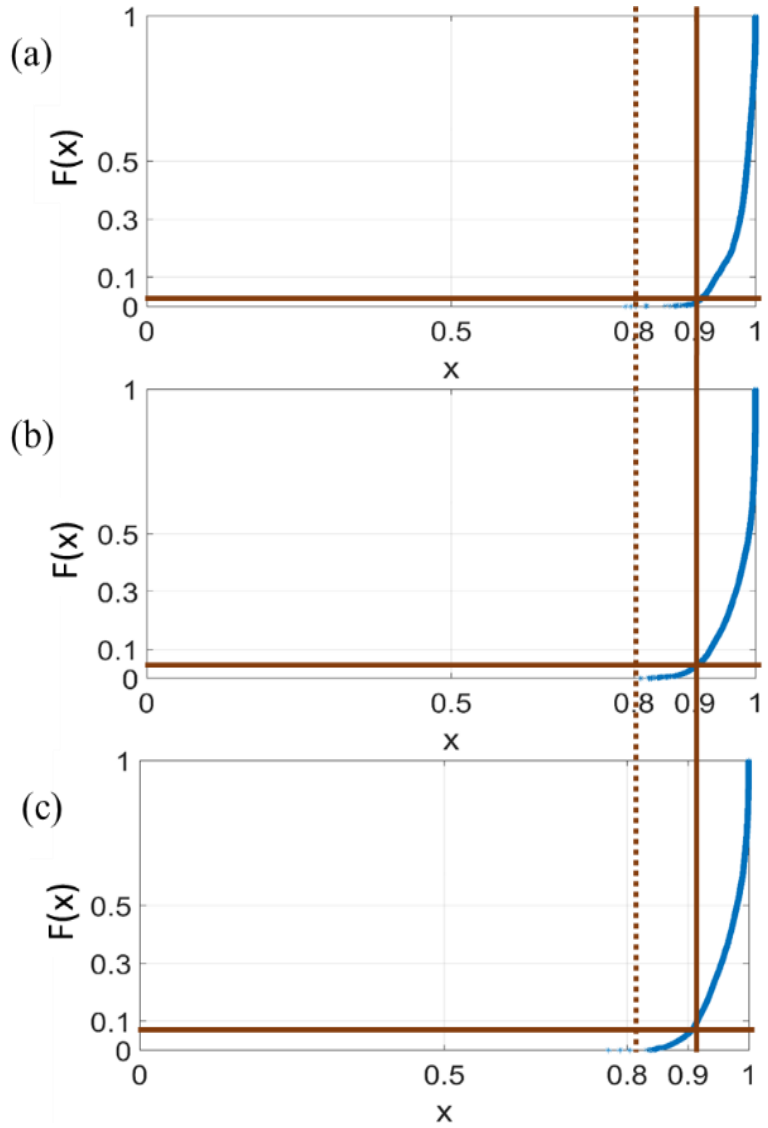

Figure 5.15: Empirical distribution (F(x)) of cross correlation coefficient (x) of all points at 32 Hz for: a) Healthy Phantom; b) 10 mm inclusion; and c) 20 mm inclusion. The solid lines show the x = 0.90 value and quantify its likelihood. The dashed line shows the location for , $\boldsymbol{x}$ = 0.80 with ~99-100 % of the values having , $\boldsymbol{x}$ ≥0.80

Table 5.1: Summary of Cross Correlation coefficients at 28 Hz

Range of cross correlation coefficient	**Number of data points**		
	Healthy	**10 mm Inclusion**	**20 mm Inclusion**
0.9-1.0	3939/4200 (93.78%)	3049/4200 (72.59%)	2874/4200 (68.42%)
0.8-0.9	249/4200 (5.92%)	1099/4200 (26.16%)	1269/4200 (30.21%)
0.7-0.8	11/4200 (0.26%)	49/4200 (1.16%)	50/4200 (1.19%)
<0.7	1/4200 (0.02%)	3/4200 (0.07%)	7/4200 (0.16%)

Table 5.2: Summary of Cross Correlation coefficients at 30 Hz

Range of cross correlation coefficient	**Number of data points**		
	Healthy	**10 mm Inclusion**	**20 mm Inclusion**
0.9-1.0	4055/4200 (96.54%)	3950/4200 (94.04%)	3619/4200 (86.16%)
0.8-0.9	124/4200 (2.95%)	242/4200 (5.76%)	579/4200 (13.78%)
0.7-0.8	21/4200 (0.50%)	7/4200 (0.16%)	2/4200 (0.04%)
<0.7	0/4200 (0.00%)	1/4200 (0.02%)	0/4200 (0.00%)

Table 5.3: Summary of Cross Correlation coefficients at 32 Hz

Range of cross correlation coefficient	**Number of data points**		
	Healthy	**10 mm Inclusion**	**20 mm Inclusion**
0.9-1.0	4152/4200 (98.85%)	4045/4200 (96.30%)	3964/4200 (94.38%)
0.8-0.9	46/4200 (1.09%)	155/4200 (3.69%)	234/4200 (5.57%)
0.7-0.8	2/4200 (0.04%)	0/4200 (0.00%)	2/4200 (0.04%)
<0.7	0/4200 (0.00%)	0/4200 (0.00%)	0/4200 (0.00%)

5.4 Discussion

The overall results in Figures 5.1-5.9 matched well. For the healthy phantom in Figures 5.1-5.3 for frequency 28 Hz, 30 Hz and 32 Hz the displacement is expected to be evenly distributed due to its homogenous, symmetric fabrication. However, the displacement distribution from frame 2 to 3 in Figure 5.1 and from frame 3 to 4 in Figure 5.2 near the actuator are uneven, indicated by a black circle, leading to some loss of symmetry which may be due to off-center application of the 2N preload, or an inhomogeneous part of the phantom. This effect is also seen in Figures 5.4-5.9 in other frames for the 10 mm and 20 mm inclusion phantoms. These local differences are evident but otherwise, the overall match between DIET experiments and the FE model is qualitatively good.

Figures 5.10-5.12 result provides further strong qualitative validation, but does not provide a specific numerical level for that correlation in matching values. Nor does it provide the necessary trend validation showing how the dynamic response that provides these values in Figures 5.1-5.9 and 5.10-5.12 are, or are not, similar. This last criterion requires the cross correlation coefficient value, and quantifies this level of validation explicitly as assessed by the frame to frame trend over the entire dynamic response.

The cross correlation values in Figures 5.13-5.15 and Tables 5.1-5.3 are very high. Thus, while small errors in material properties may cause motion magnitude differences, as seen in Figures 5.1-5.9, the overall dynamic response is well matched. Hence, the trajectory across all k = 1…10 frames appears valid, which is the key aspect in DIET diagnostics, as the changes to this trajectory, in the presence of stiffer inclusions, is the focal point of the diagnostic approach. Hence, trajectory matching over all k = 1…10 frames is critical to successfully using this FE model, or any similar model, in place of phantom experiments

given qualitatively good frame to frame magnitude matches. Especially, when considering variation in tissue density and stiffness can vary very significantly across women.

One primary reason of lower values between 0.8-0.9 of the cross correlation coefficient is DIET measurement error. Each node on the surface of the breast follows a loop of 10 points, and there is measurement error on every single point, which can degrade perfect correlation. This error is in the order of 6%, down to 2-3 μm [188], and is thus larger for nodes with smaller motions, such as near the chest wall. In addition, the small local discrepancies in Figures 5.1-5.9 will yield much lower cross correlation coefficients.

In addition, the experimental input sine wave is not always perfect, whereas the FE model input is ideal. This issue is another possible cause for the differences seen, particularly in Figures 5.1-5.9. Overall, these limitations are mitigated by the strong results in Figures 5.13-5.15, which are central to demonstrating the utility of these models to replace experimental phantom tests in surface motion analysis and diagnostics metric development.

Overall, these results demonstrate the FEA modelling approach presented can predict surface motion of these silicone breast phantoms to high correlation levels (over 0.90). The results in Figures 5.13-5.15 show it captures the changes necessary for developing diagnostic metrics and analyses from the FE model independent of exact tissue stiffness, which varies between women. The homogenous healthy phantom shows slightly better validation than the 10 mm and 20 mm inclusion cases at 28 Hz, 30 Hz and 32 Hz. However, certain assumptions regarding the finite element modelling, such as excluding skin, gravity and body mass may also have produced some differences particularly in magnitude of response, as seen in the results of Figures 5.1-5.9.

A further limitation is the cancerous lesions mimicked within the FE modelled breast phantoms were connected to healthy tissues without the ability to slide past one another, a perfect connection with perfect, as modelled stress-strain transfer. Real lesions are strongly connected to tissues but, as in the phantoms modelled here, it is important to note that there may be some form of spring or other relationship defining how they connect and transfer stress and strain due to the way they are manufactured.

In this case, the results were strong enough to ensure a good model match. However, going forward, it will be necessary to investigate the effect on displacement from imposing slip boundary conditions between cancerous tissues and healthy tissues. Such improvements could improve the modeled phantoms, as well as better reflect the actual physiology, as well.

Another limitation is the Neo-Hookean hyper-elastic model chosen to simulate these breast phantom tissues in this study. The phantoms are relatively homogeneous supporting this assumption. However, real breasts will be more heterogeneous even across similar tissue types. Thus, going forward, it would be interesting to assess more detailed mechanics models, such as the Ogden and Mooney Rivlin models, to investigate their effect on surface displacement distributions, and if they can provide a more detailed model in those cases.

A final limitation of this study is the lack of comparison to other studies. The only research in the area of DIET in general has been by the authors group, as it is still a unique approach. In particular, while elastography is a growing field in general, primarily via ultrasound and MRI data [172, 173, 180], this mechanical approach in DIET is unique at this time to the best of the authors' knowledge. In particular, the phantoms normally used for development and research in wave based imaging modalities, such as ultrasound, MRI or mammography, are

normally defined by their properties in relation to these modalities and input waves (acoustic and radio frequency electromagnetic). In this case, the phantoms are for DIET defined by their mechanical properties relative to breast tissues [184, 185], which is distinctly unique from the properties normally considered. Thus, the study presented lacks prior comparisons to the best of our knowledge.

5.5 Summary

The results show an efficient FE breast model for silicone phantoms covering healthy and inclusion cases that provides predictions of the frame to frame displacement distribution under dynamic loading conditions based on high correlation values with only small differences in magnitude. These differences are due to a range of un-modelled effects. Any inconsistency between finite element model and DIET experimental data can be improved by reducing experimental errors, as well as improving the material properties used in the model. However, the modelling approach presented can be generalized to other similar cases, and for these biomedical tissue phantoms it captures all the key dynamics necessary to use them in place of experimental phantom tests in the analysis of surface motions based on the correlation results presented comparing experimental and model results. Thus, it creates a foundation for subsequent development and optimization of DIET diagnostics metrics.

Chapter 6: Laser Doppler vibrometer validation of an optical flow motion tracking algorithm

In this chapter, breast-shaped fabricated phantoms from Chapter 3 are used with laser Doppler vibrometry to validate the optical flow (OF) motion measuring algorithm used in digital imaged elasto-tomography (DIET).

6.1 Introduction

Laser Doppler vibrometers (LDVs) are devices used to measure the instantaneous velocity or displacement of vibrating surfaces. A displacement measurement can provide useful information for medical applications, and can be particularly useful for DIET. The laser vibrometer provides a remote, non-contact measurement. Laser measurement is considered one of the most promising three-dimensional measurement methods, due to it is high resolution and non-destructive non-contact modality. Biomedical applications of this measurement, such as 3D scanning, include anatomical reconstruction [271], orthodontic treatment planning [272], cranial deformation research [273], cartilage morphology studies [274], anthropometric data collection [275].

There are typically three types of laser vibrometer, single point laser vibrometers, scanning laser, and 3-dimensional scanning lasers. Single point laser vibrometers measure the velocity or displacement of a single point on an object surface. Scanning systems can measure vibrations on a grid of points on an object surface. The 3 dimensional scanning systems can

measure 3D vibration of a planar or non-planar surface [276]. In this chapter, a single point laser Doppler vibrometer used for horizontal measurements.

There are also several limitations to laser vibrometry. Line of sight requirements make measurements demanding, especially on complicated 3D geometries, such as a breast. Measurement quality also depends upon surface quality, particularly if a laser beam strikes an optically rough surface, such as skin, where the laser wavelength (633 nm for the red HeNe laser) is on the scale of surface roughness. Reflective tape is thus a commonly used surface treatment in laser vibrometer measurements to maximise the return light intensity [277].

Overall, it is not a suitable replacement for OF, but would be useful to validate measured motions obtained from OF. In this chapter, a single point laser Doppler vibrometer system made by Polytech (North America, USA) is used to validate horizontal out-of-plane measurements calculated using OF for a series of breast-shaped phantoms.

6.2 Materials and methods

6.2.1 Sample preparation

Retro-reflective tape is a commonly used surface treatment in laser vibrometer measurements to maximize the return light intensity. Because the silicone surface is oily and tape absorbs oil, to ensure that the reflective surface are free of dirt and oil which can reduce the effective reflectance of the surface therefore, different sizes of glass beads and ARDROX were used to test the laser intensity and received signal. Glass beads with mesh size of 100 um with reflective index ND>1.97 were found to maximise the return light intensity. These materials are shown in Figure 6.1.

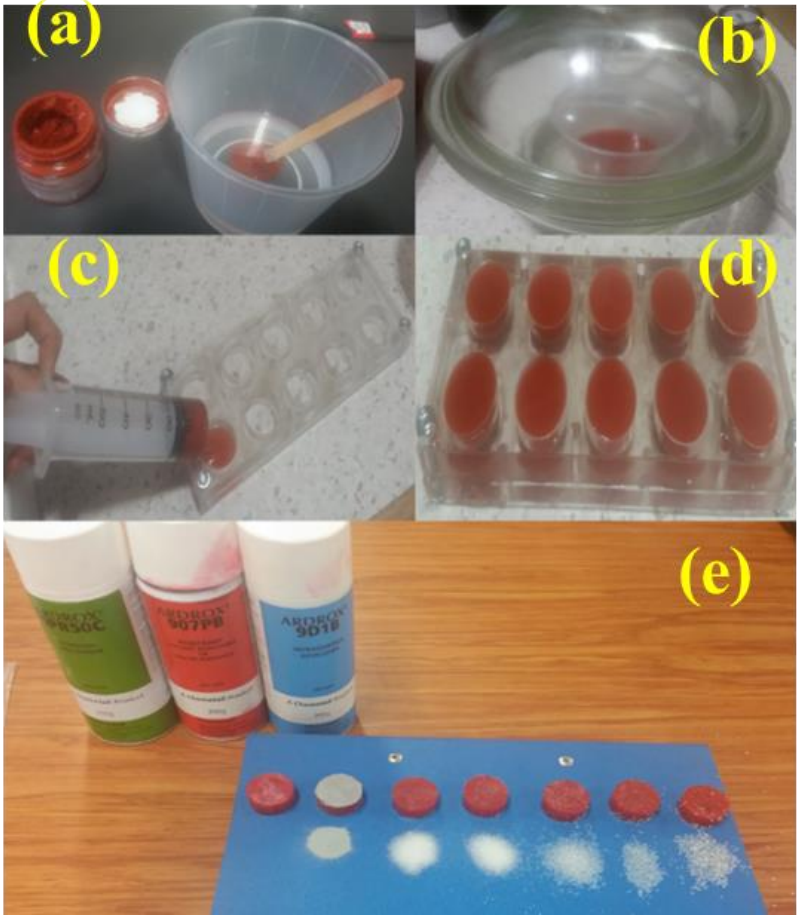

Figure 6.1: (a) Mixing silicone pigment with silicone oil; (b) Removing bubbles from silicone; (c) Pouring exact amount of silicone liquid; (d) Samples fabricated under 50 ^{o}C; (d) Reflective glass beads size varies from 500 to 100 um and ARDROX

Three silicone based homogenous breast shaped phantoms were created as per Chapter 3. One was homogenous and 'healthy', and the remaining two had a 10 mm and a 20 mm inclusions to simulate tumors. Phantom dimensions and fabrication procedures were followed from published reports [185] and Chapter 3. There are these three test validation cases.

6.2.2 Experimental set-up

A schematic of the measurement hardware for the experiment is shown in Figures 6.2 - 6.4. A Polytech (North America, USA) laser Doppler vibrometer system was used. The laser Doppler vibrometer system consists of the OFV-5000 controller and the OFV-512 sensor

head using a low-power (class 2) Helium Neon laser. The vibrometer controller delivers signals and power to the sensor head, and processes the return signals. Interference of the measurement and reference beams occurs in the sensor head, and results in a fringe pattern from which frequency and phase difference signals are determined. These signals are sent to the controller where they are decoded.

With a range of actual DIET screening manufacture boundaries, a new prototype DIET was built to simulate DIET as shown in Figures 6.3 and 6.4. In prototype DIET a D.C motor 9700 RPM is attached. When the specified voltage is supplied to a motor, it rotates the output shaft at some speed. The maximum 12 volts can be applied to get 161 Hz with no load. In this experiment only 16 Hz to 40 Hz were required as input frequency.

In actual DIET screening experiments, a two Newton (2N) preload is applied, which ensures full contact between the phantom and the actuator and does not squash the phantom. In prototype DIET 5 shims of 1 mm thick were placed to apply preload as 2N. This 5 mm displacement preload was selected from Chapter 4 finite element modelling. Steady state mechanical, sinusoidal input oscillations of 16Hz, 24Hz, 32Hz, and 40Hz of low amplitude, 1 mm peak to peak, is applied to the phantom tip, while hanging pendulous [28, 30, 185]. Horizontal out of plane displacements of the phantom surface were measured using laser Doppler vibrometer. The experiments were carried out on top of a vibration isolation table to avoid unnecessary surrounding vibration. The summary of measured points on the phantom surface is shown in Figure 6.5.

Each phantom was equally divided into 4 quadrants and 9 surface points were recorded on each section. Therefore, 36 surface points were recorded for each phantom. These 36 points are also shown in Figure 6.5.

To ensure reliability, each phantom was tested twice and the average of the resulting peak magnitude displacement were calculated for each phantom and point. As the surface points were marked on each phantom, the laser beam was directed on the same position and verified by eye. Comparisons of surface points serves to validate the accuracy of the DIET surface point OF measurement algorithm [188].

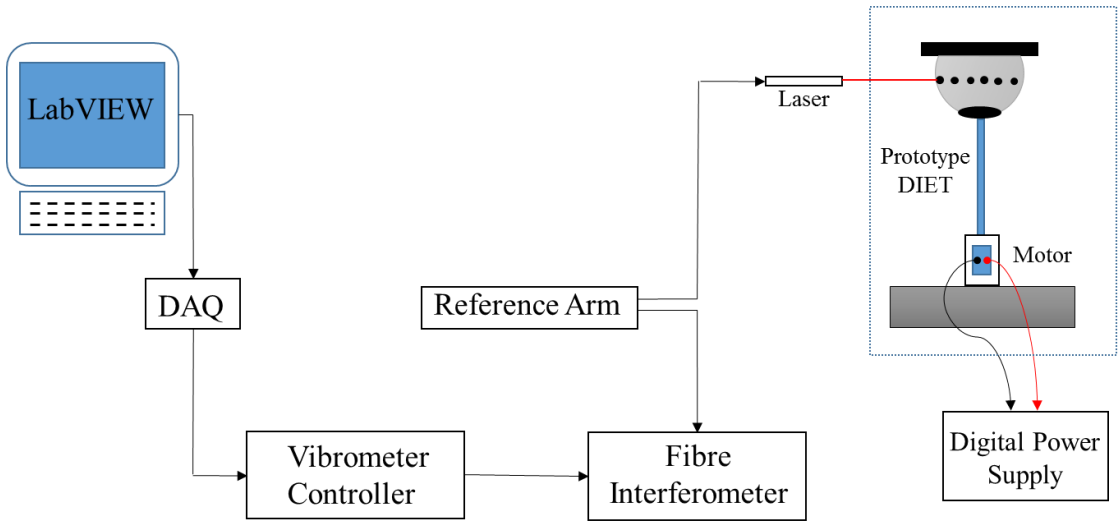

Figure 6.2: Experimental Set-up

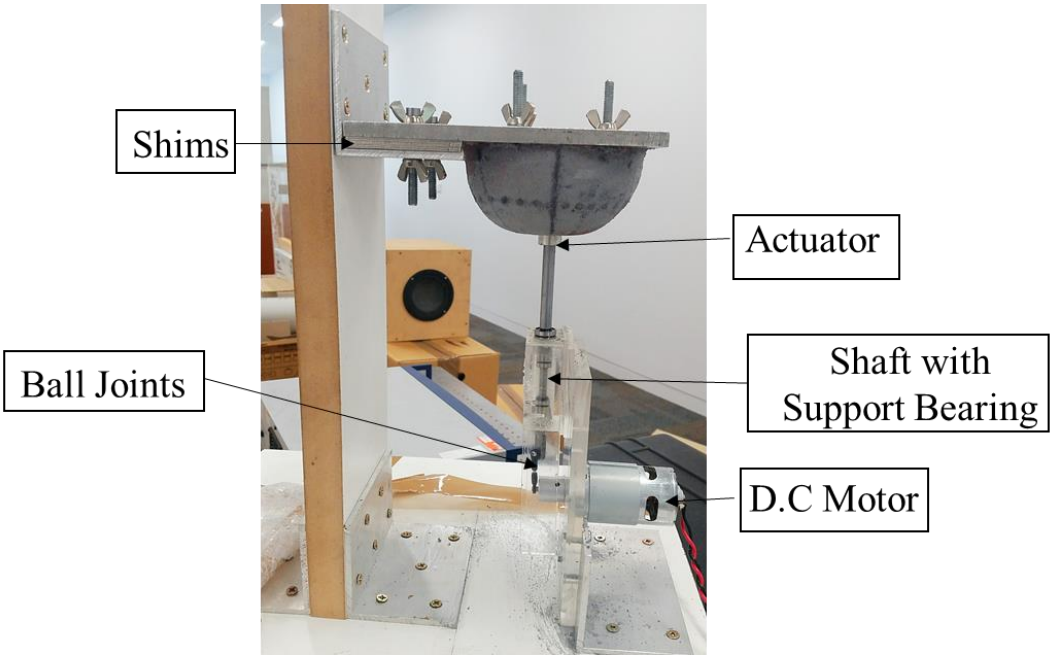

Figure 6.3: Prototype DIET

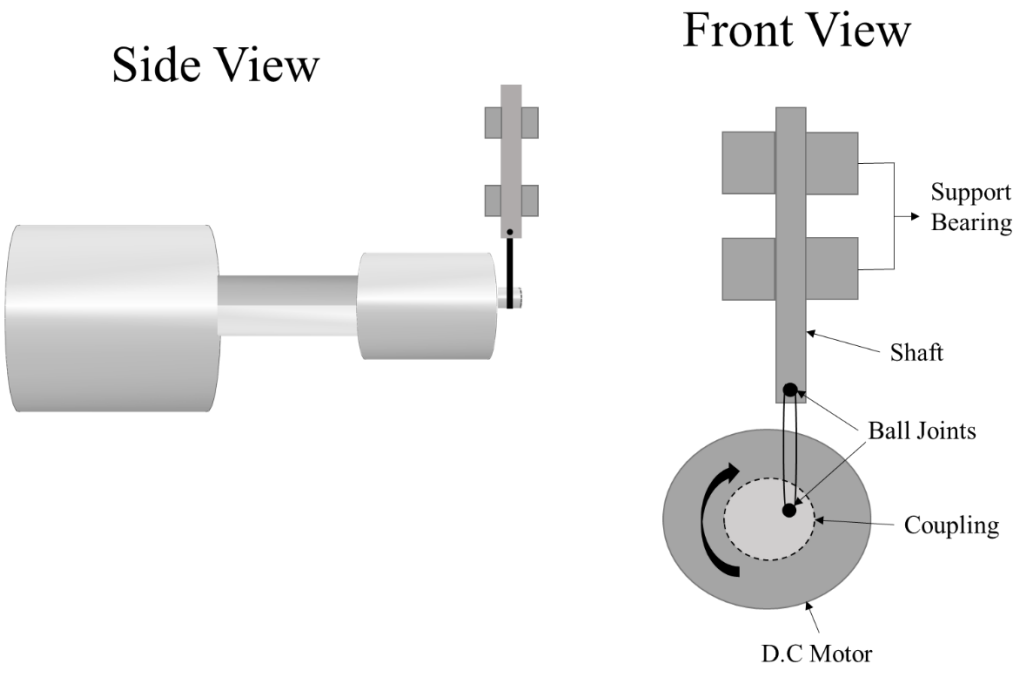

Figure 6.4: Schematic diagram of motor

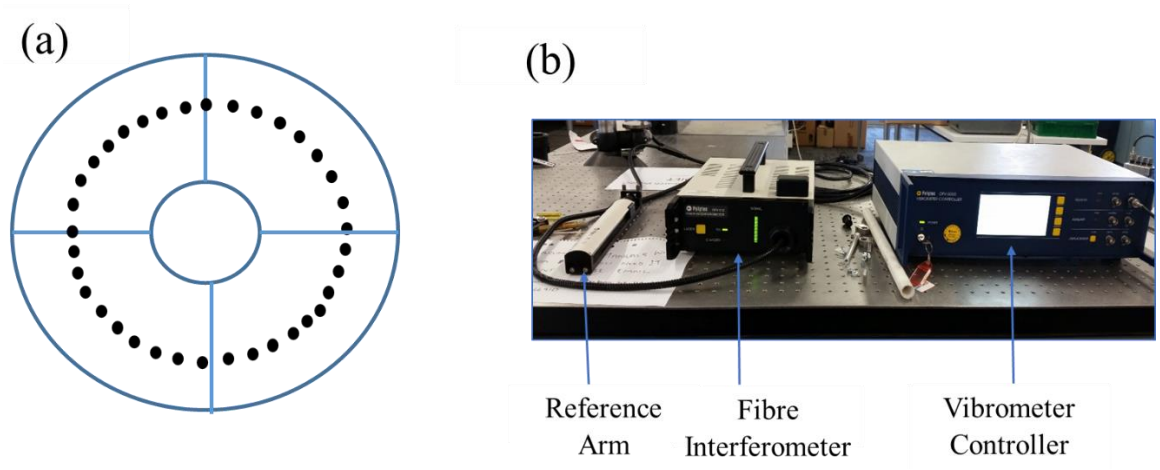

Figure 6.5: (a) Top view of phantom - summary of marked surface points on the breast shaped healthy, with a 20 mm and a 10 mm inclusions phantom for displacement measurement; (b) laser Doppler vibrometer equipment.

6.2.3 Optical flow validation

In this section, positive peak magnitudes of horizontal displacement from the sinusoidal response captured by OF are compared to those assessed by laser doppler. Horizontal displacements of multiple surface points on the breast shaped phantoms are measured from single point laser Doppler vibrometer. These peak horizontal displacement values are compared to validate the DIET OF derived experimental data. The position of surface points on the phantom surface for the three phantom cases tested are also explained in Figure 4.1 in Chapter 4, as well as in Figure 6.5.

6.3 Results and discussion

6.3.1 Validation of DIET OF algorithm

Figure 6.6 shows LDV measured displacement at 16 Hz input frequency for a single section, which includes N=9 surface points on the healthy, no inclusion phantom. Figures 6.7 and 6.8 show the surface positive peak horizontal displacement at frequencies of 16 Hz, 24 Hz, 32

Hz, and 40 Hz on the 3 breast shaped phantoms for the LDV and DIET experimental data, respectively.

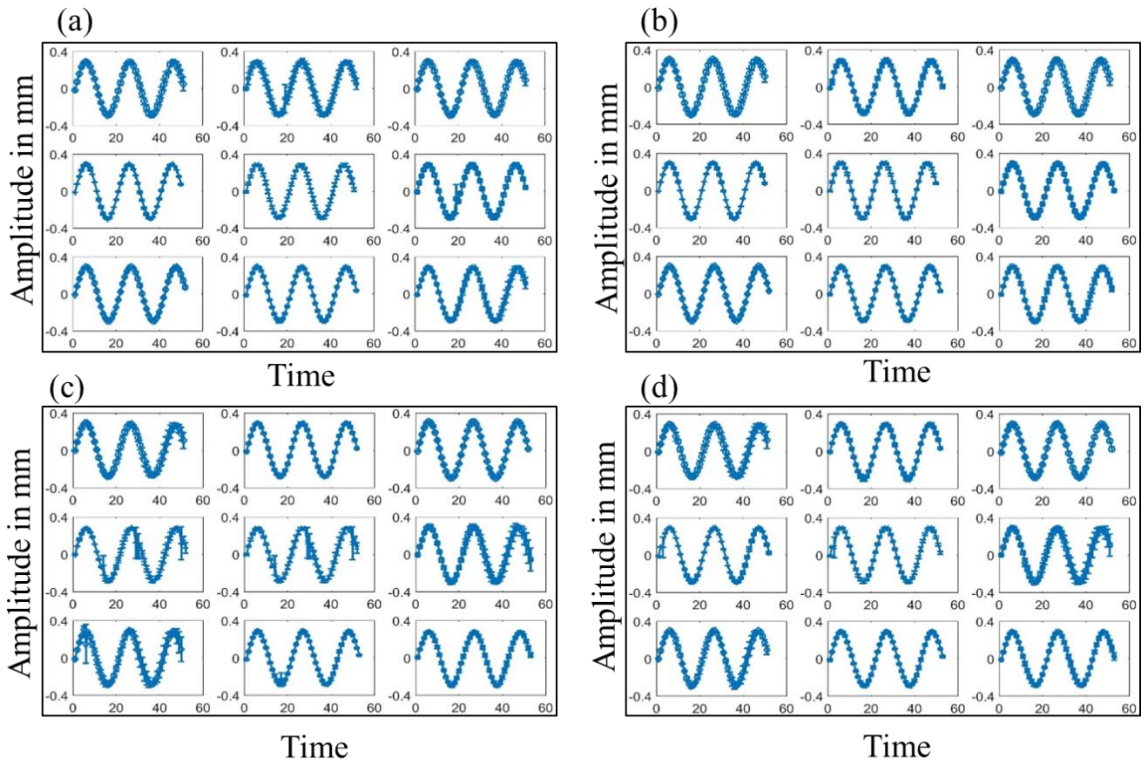

Figure 6.6: Laser Doppler vibrometer data for each quadrant with excitation amplitude of 1mm peak to peak on a healthy phantom surface at 16 Hz sinusoidal excitation, (a) 9 points of section 1; (b) 9 points of section 2; (c) 9 points of section 3; (d) 9 points of section 4.

The healthy breast phantom is homogenous and the peak positive horizontal displacement measured from the homogenous healthy phantom are assumed to be the same on all sides. In Figure 6.7, it can be noticed that the positive peak of horizontal displacement of this healthy phantom for each frequency is almost equal in all sides, as expected. Any fluctuation in points may be due to misalignment between the phantom surface and the laser beam, as the direction of the laser beam is manually changed to investigate each point on the phantom surface, a main limitation of using a single point laser Doppler vibrometer, as any variability

in positioning introduces a systemic bias. It may also be due to small in-homogeneities in the experimental phantom.

It has been well recognised that inclusions are 4-10 times stiffer than the surrounding breast tissues [270] as described in Chapter 3 as well. The tissue displacements are inversely proportional to the stiffness of the tissue. Thus, a stiffer region of tissue exhibits smaller displacements than a more compliant region [27, 28]. The dashed circle shows the peak value of horizontal displacement near the inclusions are smaller than the rest of the sides. However, the peak displacement magnitude of non-stiffer inclusion regions for both 10 mm and 20 mm inclusion phantoms match well with the magnitude of peak displacement of healthy phantom, as expected.

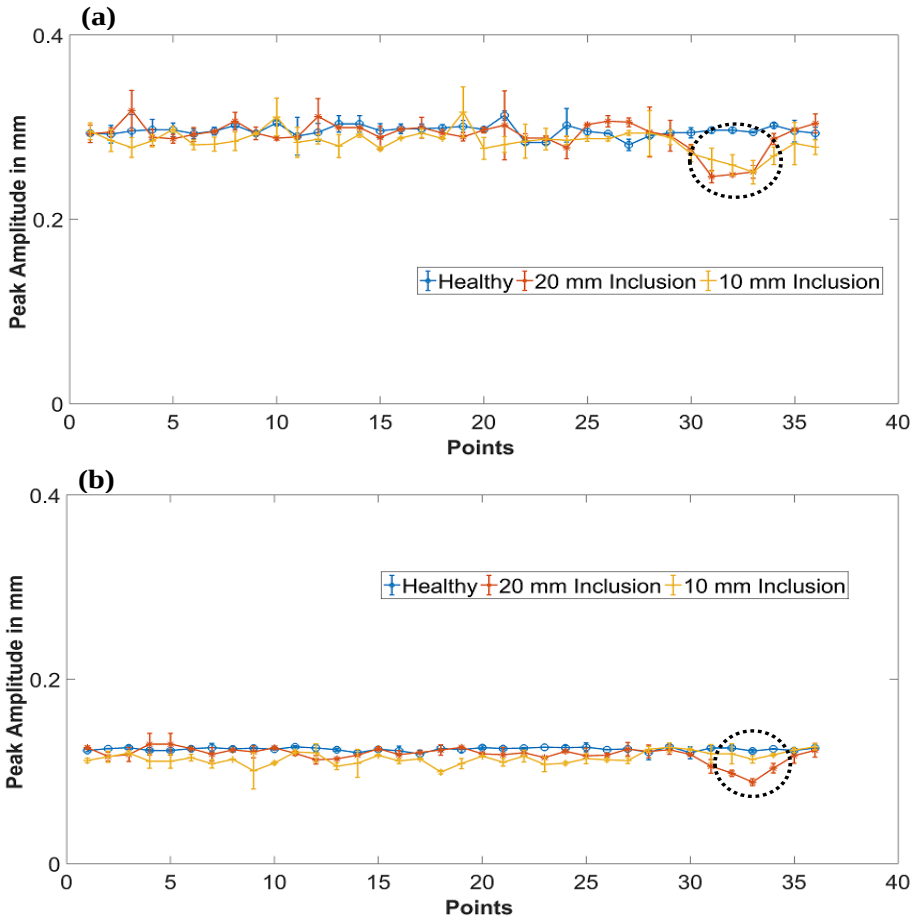

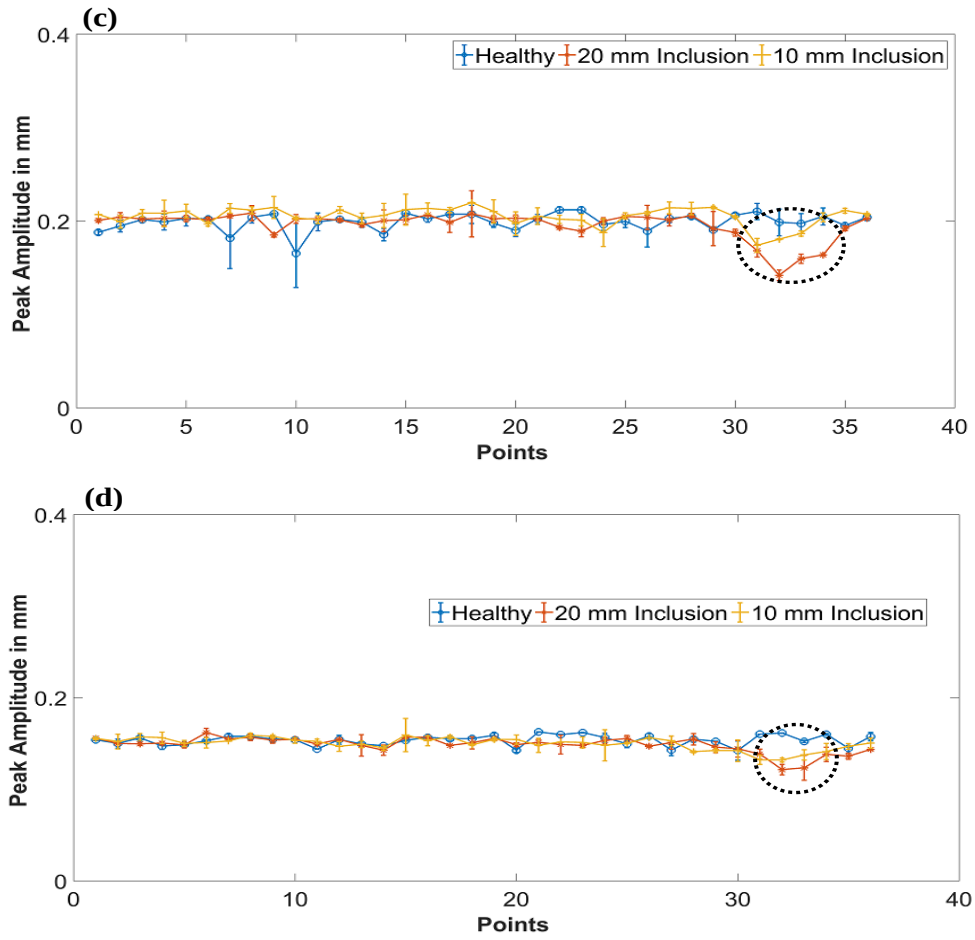

Figure 6.7: Laser Doppler vibrometer data - excitation amplitudes of 1mm peak to peak on phantom surface (a) 16 Hz excitation; (b) 24 Hz excitation; (c) 32 Hz excitation; (d) 40 Hz excitation

Similarly, Figure 6.8 shows the peak horizontal displacement values of DIET OF calculated experimental motion data for all three phantoms. It is clear the laser Doppler vibrometer data are less variable than DIET experimental data. This difference occurs because the laser sensitivity/resolution is high compared to the DIET OF reconstruction procedure.

In addition, DIET OF experimental motion data measured in 3D, whereas the laser Doppler vibrometer data are measured in 2D. Finally, the position of the DIET OF data points is not exactly the same as the laser points, which could introduce small differences.

The peak horizontal displacement values of the DIET OF for the healthy phantom are almost equal in all frequencies, which shows the phantom is homogenous and is an expected result. For phantoms with inclusions, the displacement near the inclusion is smaller than the surrounding tissues.

The peak horizontal displacement values difference for the 20 mm inclusion is bigger than the 10 mm inclusion. Thus, the peak magnitude displacement near the 20 mm inclusion is much smaller than for the 10 mm inclusion phantom and region, but the difference was larger than seen with the laser Doppler vibrometer.

Figure 6.9 compares separate DIET OF and laser doppler experimental data for each actuation input frequency and phantom. Table 6.1 shows the percentage calculated error range for all 36 surface points between laser doppler and DIET OF for all three phantom cases. The percentage error decreases with increasing frequency. Peak amplitude also decreases with the increasing of frequency. Almost all errors are less than 8 %, which is very good agreement, and 90 % of errors are less than 5 %.

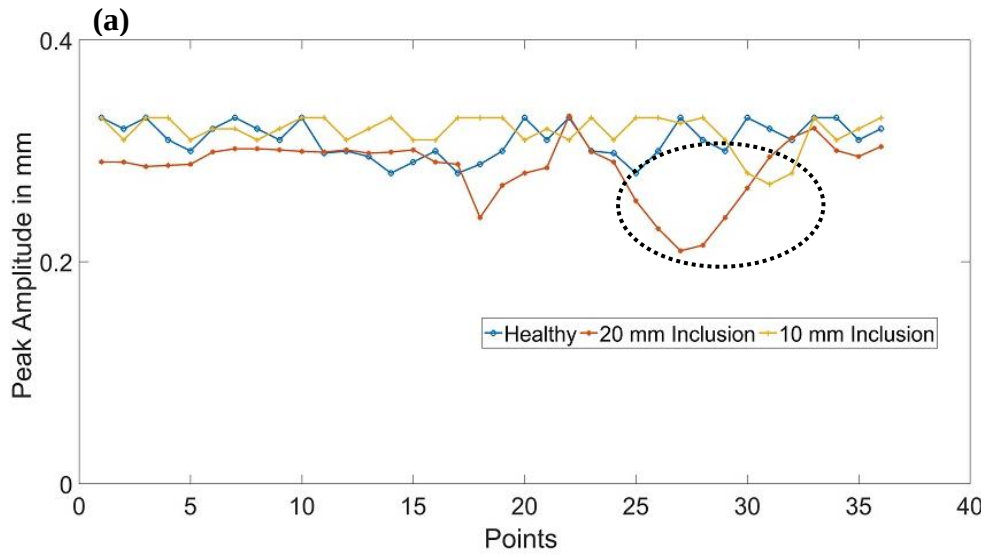

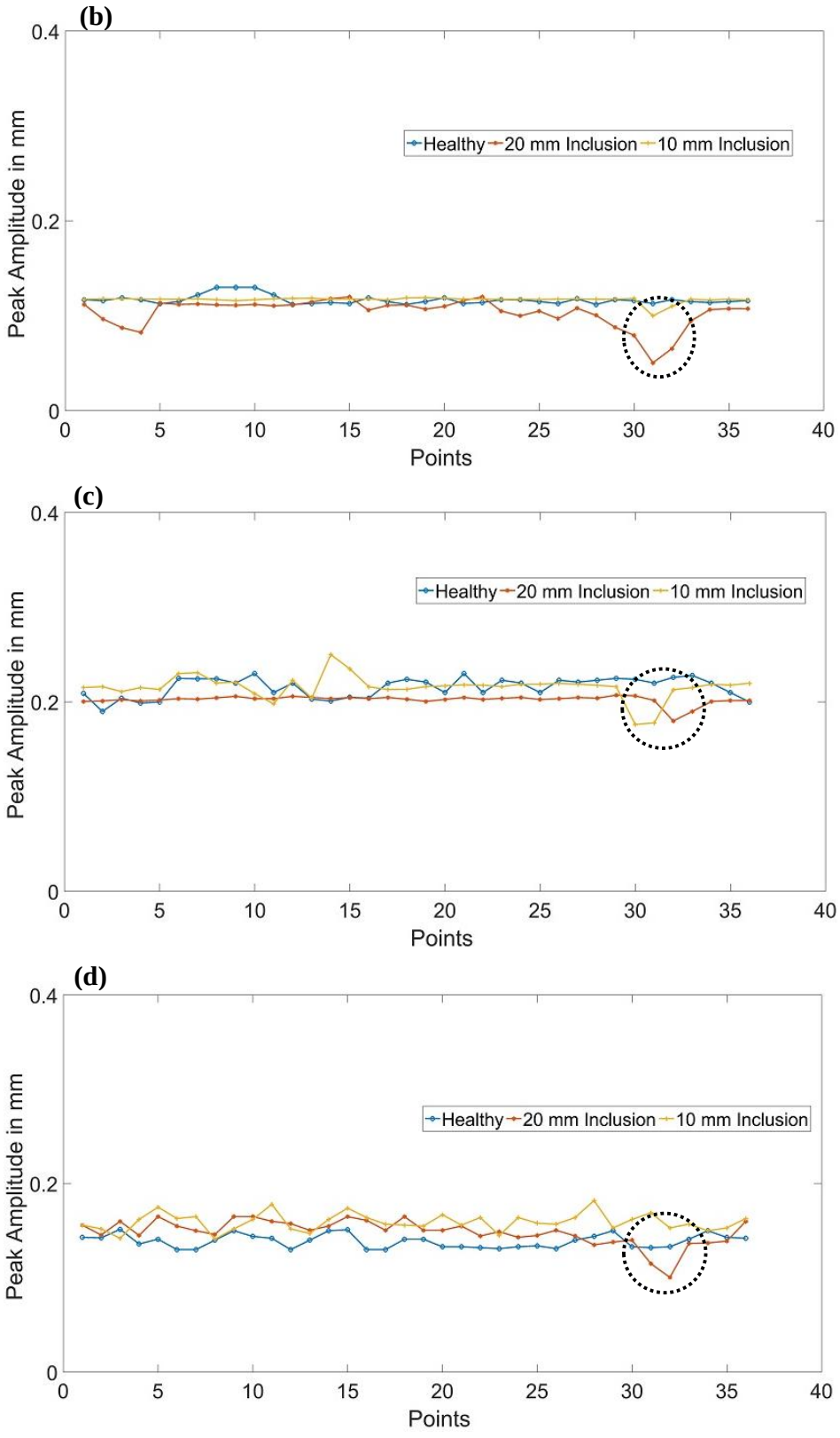

Figure 6.8: DIET OF experimental data - excitation amplitudes of 1mm peak to peak on phantom surface (a) 16 Hz excitation; (b) 24 Hz excitation; (c) 32 Hz excitation; (d) 40 Hz excitation

(a)

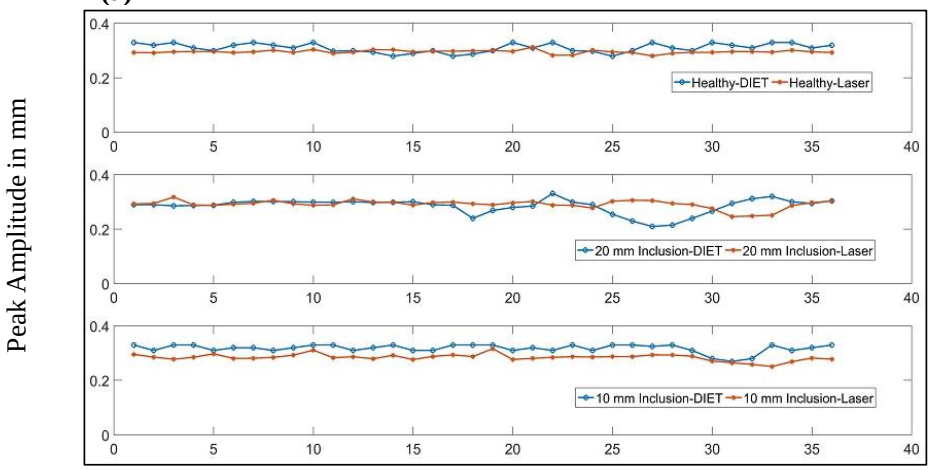
Peak Amplitude in mm
Healthy-DIET
Healthy-Laser
20 mm Inclusion-DIET
20 mm Inclusion-Laser
10 mm Inclusion-DIET
10 mm Inclusion-Laser
Points

(b)

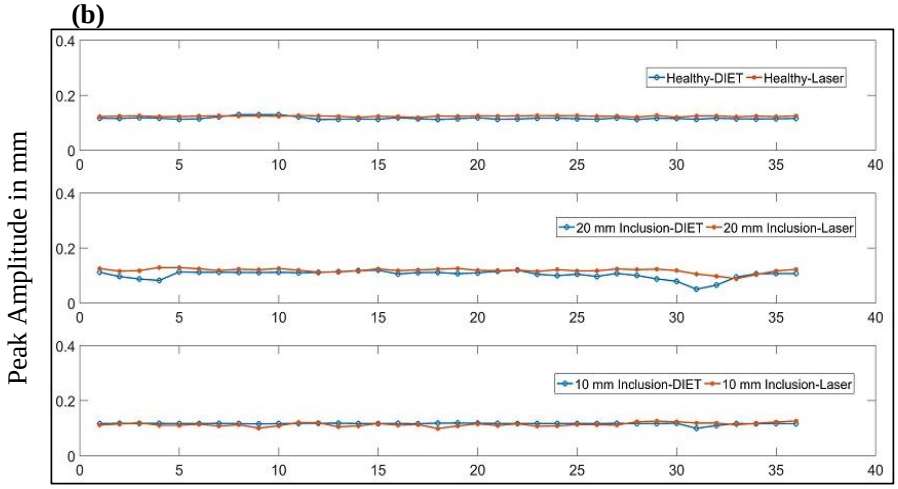
Peak Amplitude in mm
Healthy-DIET
Healthy-Laser
20 mm Inclusion-DIET
20 mm Inclusion-Laser
10 mm Inclusion-DIET
10 mm Inclusion-Laser
Points

(c)

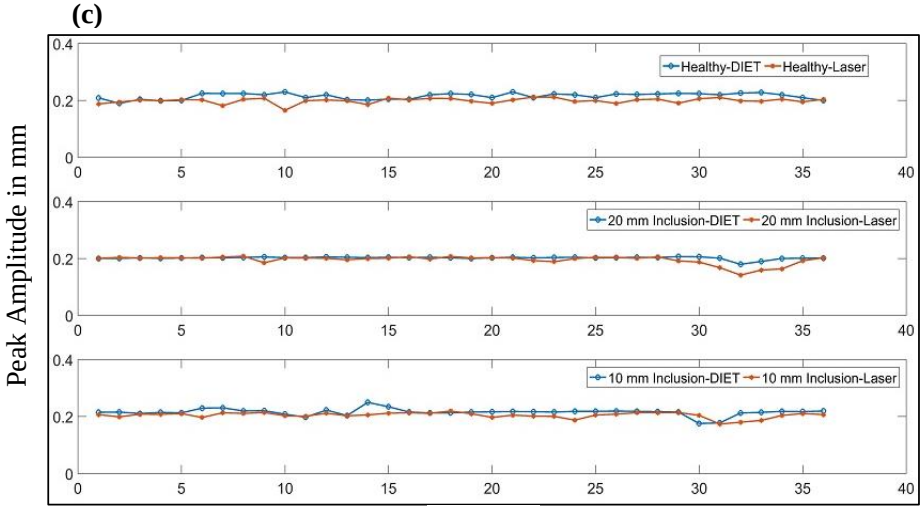
Peak Amplitude in mm
Healthy-DIET
Healthy-Laser
20 mm Inclusion-DIET
20 mm Inclusion-Laser
10 mm Inclusion-DIET
10 mm Inclusion-Laser
Points

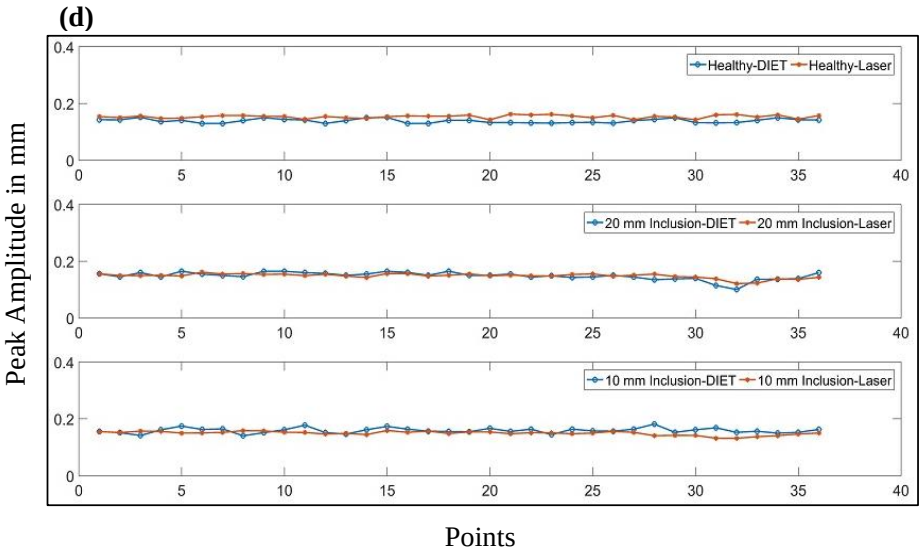

Figure 6.9: Peak amplitude of DIET and laser Doppler vibrometer experimental data (a) 16 Hz excitation; (b) 24 Hz excitation; (c) 32 Hz excitation; (d) 40 Hz excitation

Table 6.1: Summary of absolute errors between LDV and DIET OF overall input frequencies

Range of absolute error in %			
Frequency	Healthy	20 mm Inclusion	10 mm Inclusion
16 Hz	0.0 - 4.6	0.0 – 7.8	0.0 – 7.8
24 Hz	0.0 – 5.4	0.0 – 6.9	0.0 – 4.9
32 Hz	0.0 – 1.6	0.0 – 4.1	0.0 – 1.9
40 Hz	0.0 – 4.2	0.0 – 4.2	0.0 – 2.7

Overall, these results show the DIET OF measurement can accurately capture surface motion of these silicone phantoms, as validated by the laser Doppler vibrometer. However, there are several limitations using a laser Doppler vibrometer that may play a role. One of the main limitations is the difficulty of realizing perfect alignment between the investigated target and laser beam. In addition, there is always environmental noise, but this noise is very small for this laser Doppler vibrometer. In all cases, the error appears very consistent with no apparent bias. Hence, the OF method can be conducted to provide lower error motion with resolution in order of 20 μm, 50 μm, 10 μm, and 20 μm for 16 Hz, 24 Hz, 32 Hz and 40 Hz, respectively.

6.4 Summary

The results of the laser Doppler validation of DIET OF indicate that the method works well. The overall average absolute error for 16 Hz, 24 Hz, 32 Hz, and 40 Hz are 20 μm, 50 μm, 10 μm, and 20 μm respectively, which indicates that the OF method has good resolution. In addition, 90% of errors between LDV and DIET OF data are < 5 %, and this shows that DIET OF tracks points very well. Overall, the OF method is thus validated against a gold standard and its level of resolution quantified. Knowledge of both of these metrics is necessary to develop optimal breast cancer diagnostics from OF measured DIET motion data.

Chapter 7: Finite element modelling for different sizes of inclusions at different positions

In this chapter the same finite element (FE) modelling and data analysis procedure from Chapters 4 and 5 were used to model phantoms with stiffer 10 mm and 20 mm inclusions at different positions using input actuation frequencies of 16 Hz, 24 Hz, 32 Hz and 40 Hz. The goal is to create an initial test of how well phantom inclusions might represent their stiffer presence on surface motion, but using a validated FE model.

7.1 Introduction

Due to the good validation of the finite element (FE) modelling of DIET experimental phantom data described in Chapters 4 and 5, these models and methods were used to model phantoms with the same inclusion sizes but at different locations. The same hyper-elastic properties and phantom dimensions from Chapter 3 were used in modelling. The more specific goal is to assess and quantify the robustness and sensitivity of potential surface motion diagnostics to inclusion location, particularly to depth. It is thus an initial application using FE models in place of extensive experimental series.

7.2 Finite element modelling

A total of 6 breast shaped phantoms were modelled with the same overall geometry and dimensions, loading, material properties and boundary conditions used in Chapter 4. Two different sizes of stiffer inclusion with 10 mm and 20 mm diameters were placed at three

different positions. Input actuation frequencies of 16 Hz, 24 Hz, 32 Hz and 40 Hz were used. The three inclusion locations are described in Figure 7.1. All of them can be located in an (X, Z) plane, Figure 7.2 shows the inclusion locations in further detail on an (X, Z) plane slice. For simplicity only locations A, B, and C will be used for reference.

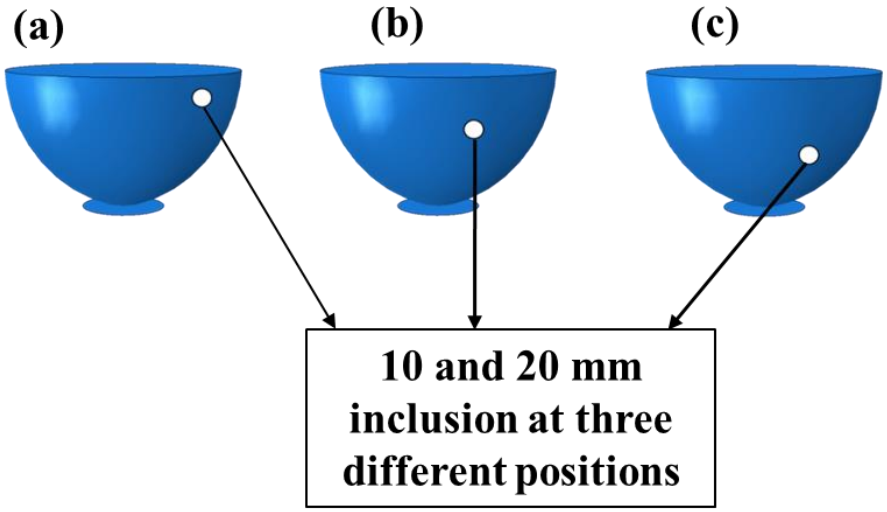

Figure 7.1: Three phantoms configurations were each modelled with two different sizes of inclusions at positions: (a) (X, Y, Z) = (35, 0, -13); (b) (X, Y, Z) = (12, 0, -23); and (c) (X, Y, Z) = (15, 10, -43) yielding 6 phantoms in total

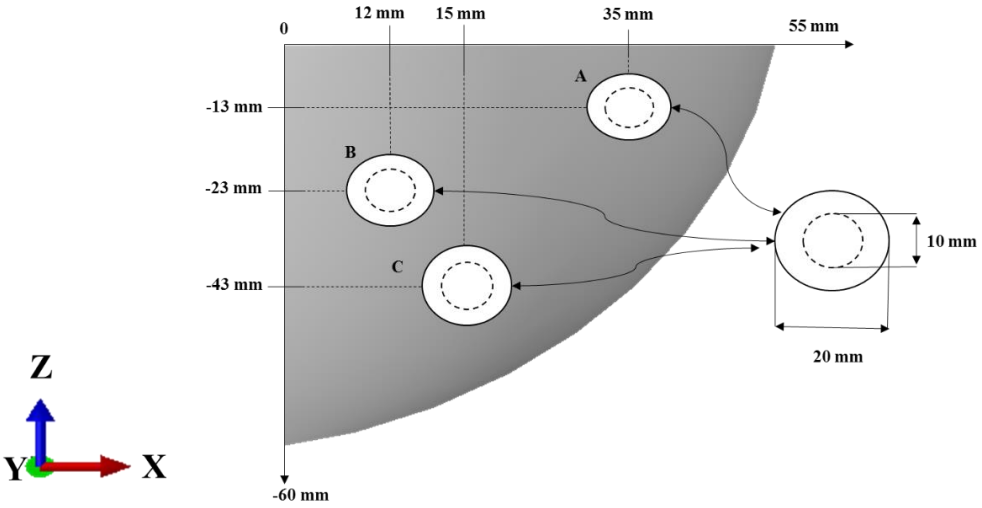

Figure 7.2: (X, Z) planar slice showing three locations of inclusions: Each of the 6 phantoms with 20 mm and 10 mm inclusions at positions (X, Z) = (35, -13) mm, (12, -23) mm, and (15, -43) mm. The actuator is at (X, Z) = (0, -60) mm. The chest wall is along (X, Z) = (0, 0) to (0, 55) mm

Similar to Chapter 4, a 3D free mesh was assembled using quadratic tetrahedral ten-node C3D10M (Continuum 3Dimensional 10-node Modified) elements using ABAQUS version 6.14 (ABAQUS Inc., Johnston, Rhode Island, United States). To avoid small gaps between the phantom surface nodes, a mesh size of 1 mm was used in these models. There were approximately 69000 surface nodes on each phantom model.

7.3 Model analysis

The overall average radial displacement values over all k = 10 frames with l = 1…69000 surface points are compared using Equation 4.2, repeated here:

$$\overline{\Delta r_l} = \frac{1}{10}\sum_{k=1}^{10} \Delta r_l^k \tag{7.1}$$

Where l, k and $\overline{\Delta r_l}$ are as defined in Chapter 4, Equation 4.1

7.4 Results and discussion

Figures 7.3-7.8 show the average radial displacement for 16 Hz, 24 Hz, 32 Hz and 40 Hz sinusoidal input actuation for each node on the phantom surface ($\overline{\Delta r_l}$). The 10 mm and 20 mm inclusions are located with a black dotted circle. The average radial displacement reduces with increasing input actuation frequency. Thus, the maximum displacement on the color bars was fixed to 0.3 mm for 16 Hz and 24 Hz and 0.1 mm for 32 Hz and 40 Hz. All figures show larger displacements nearer to the actuator and smaller to zero displacement at the chest wall, as expected.

Figure 7.3 locates the 10 mm stiffer inclusion near to the chest wall where it was inserted.

Displacement at the phantom surface is inversely proportional to the inclusion stiffness and because inclusions have higher stiffness than healthy tissues, smaller motion can locate an inclusion. The 10 mm stiffer inclusion is small and inserted near to the phantom surface in this region, and thus a small region is effected with smaller average radial displacement near the inclusion.

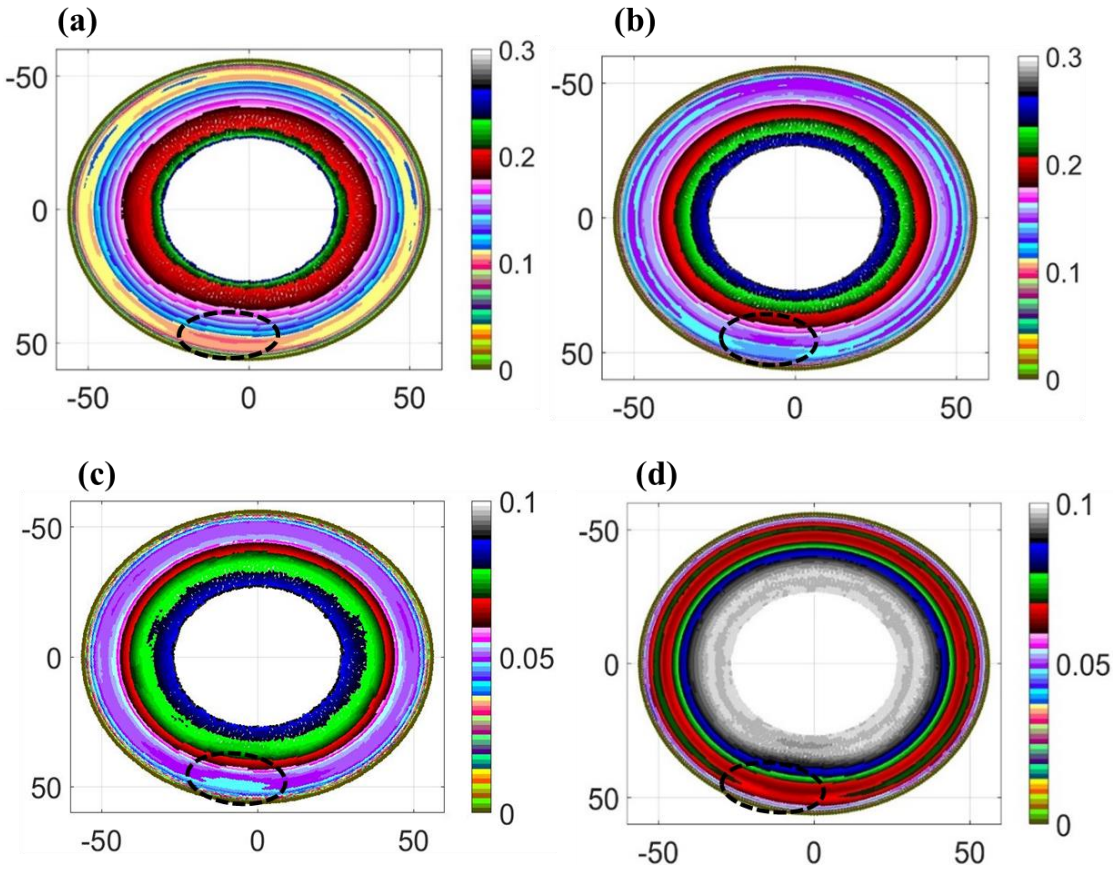

Figure 7.3: Location A: Average radial displacement distribution (all units in mm) for a 10 mm inclusion located with a dotted black circle at frequencies of: (a) 16 Hz; (b) 24 Hz; (c) 32 Hz; and (d) 40 Hz

Figure 7.4 shows results for a 10 mm inclusion located 12 mm from the centre of the phantom at location B. It is difficult to locate the inclusion from the top view of the phantom. However, Figure 7.4 (c) shows the small differences in radial average displacement between the stiffer inclusion region and healthy tissues at 24 Hz of frequency. Thus, the deeper

inclusion with smaller, 10 mm diameter can be found, despite the difficulty of this location [27].

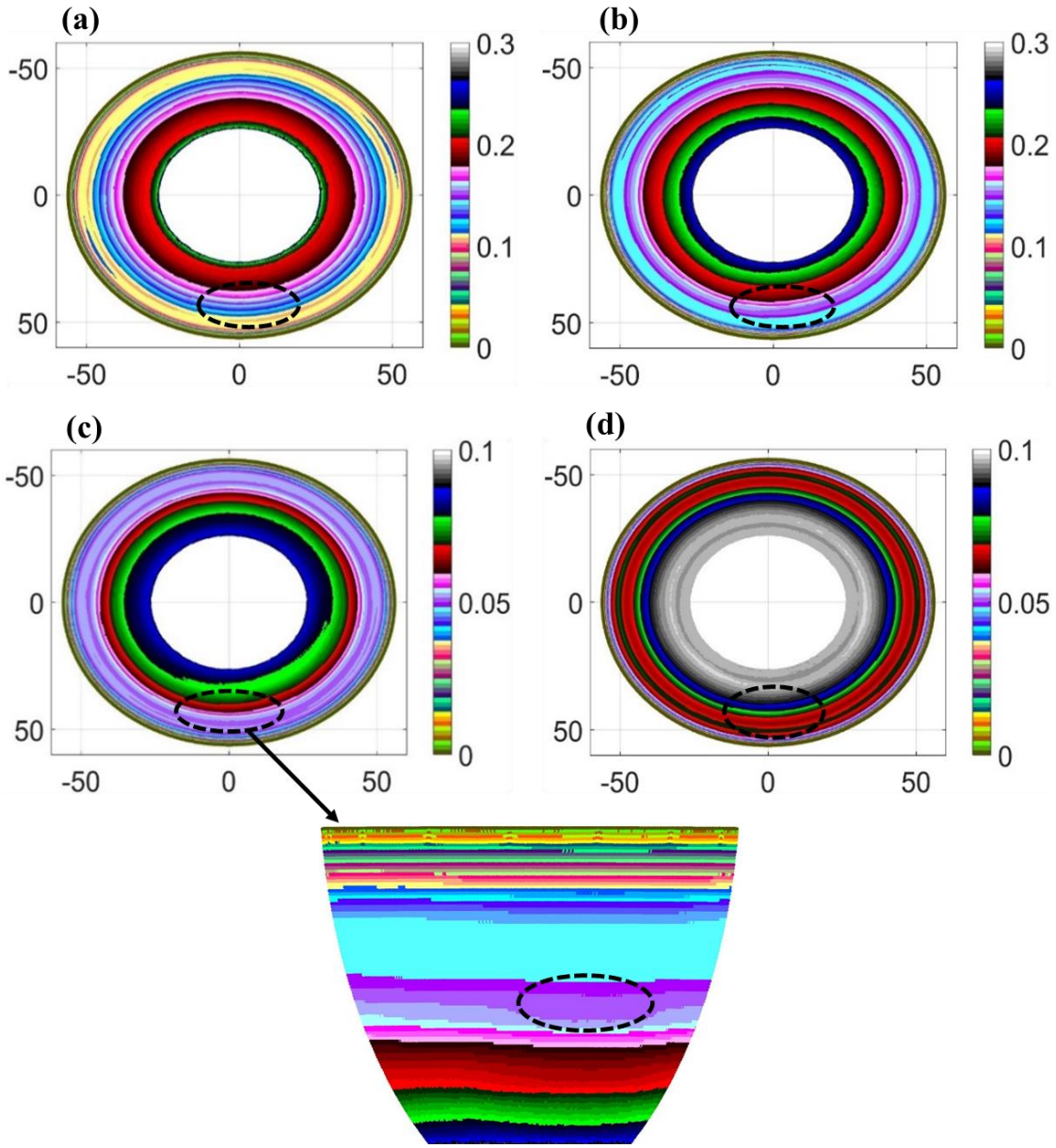

Figure 7.4: Location B: Average radial displacement distribution (all units in mm) for a 10 mm inclusion located with a dotted black circle at frequencies of: (a) 16 Hz; (b) 24 Hz; (c) 32 Hz; and (d) 40 Hz

Figure 7.5 shows 10 mm inclusion case at location C, which is slightly off centre in Figure 7.1. Even the area near to the chest wall is also effected by the inclusion in this case, seen by

the smaller average radial displacements at frequencies of 16 Hz and 24 Hz. However, input frequencies of 32 Hz and 40 Hz show smaller average radial displacement only near to where the inclusion is inserted, and the rest of the phantom region reacts as healthy tissue. Thus, each frequency react somewhat differently in this case, but all of them locate the inclusion.

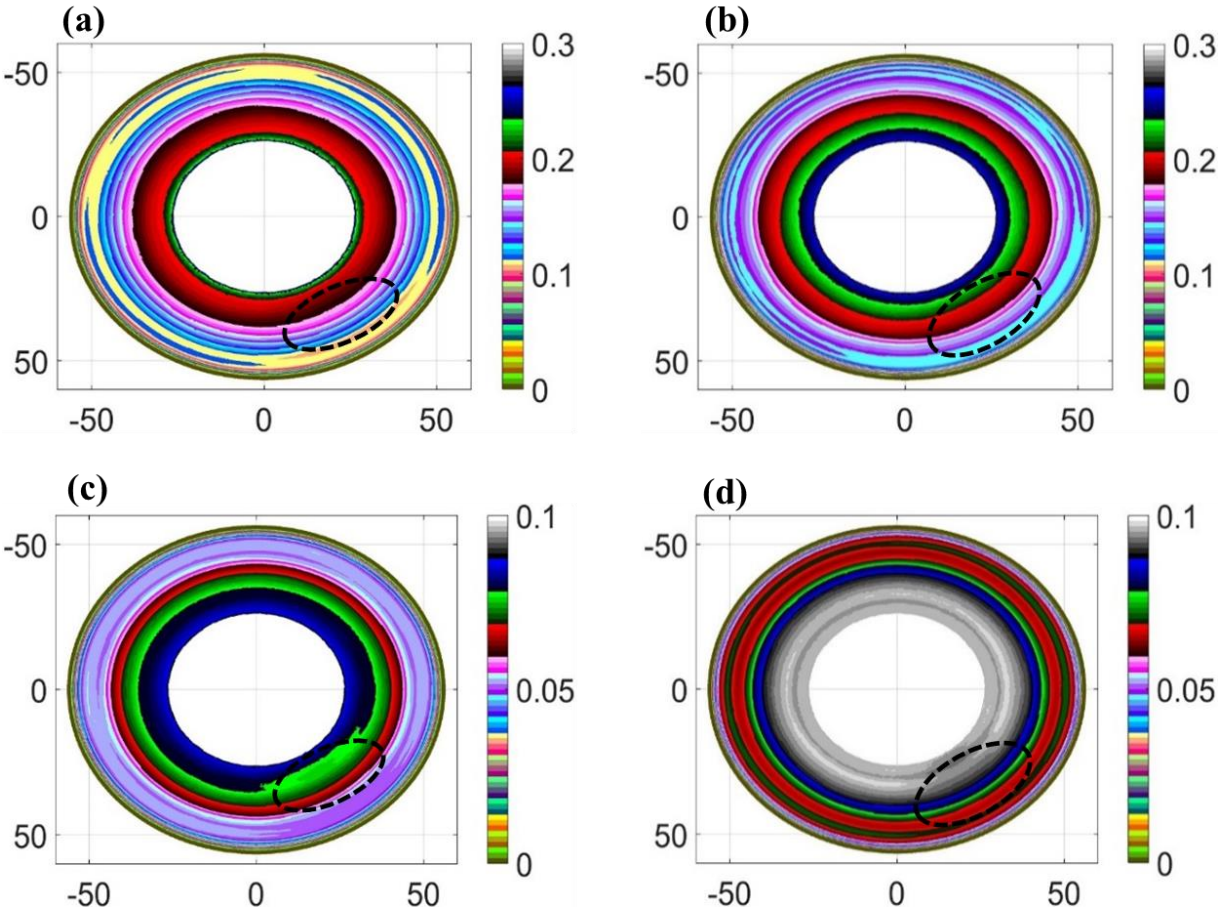

Figure 7.5: Location C: Average radial displacement distribution (all units in mm) for a 10 mm inclusion located with a dotted black circle at frequencies of: (a) 16 Hz; (b) 24 Hz; (c) 32 Hz; and (d) 40 Hz

Figure 7.6 shows promising results for the larger 20 mm inclusion at location A. A greater region on the phantom surface displays the impact of the inclusion from the chest wall to the bottom of the phantom near the actuator. It is again located by smaller average radial displacements. At every frequency it is easy to locate this larger, stiffer inclusion.

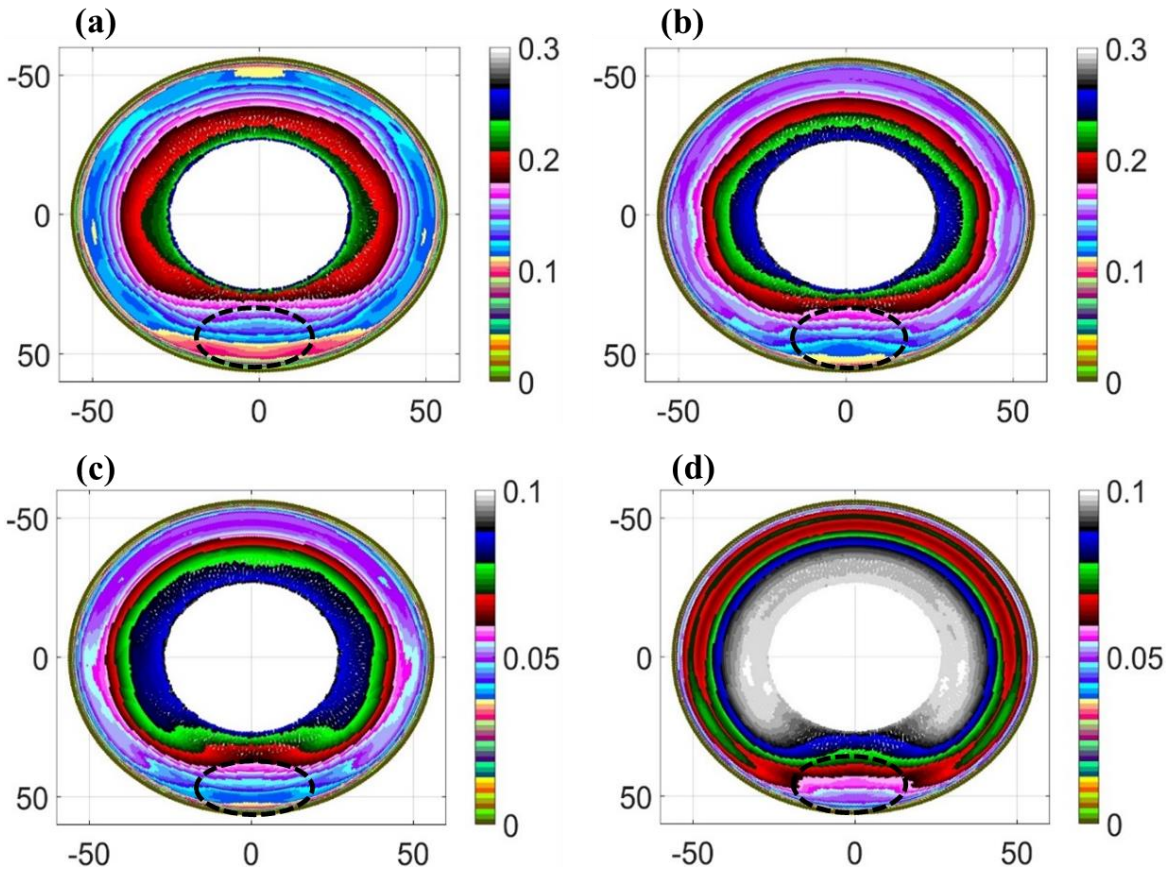

Figure 7.6: Location A: Average radial displacement distribution (all units in mm) for a 20 mm inclusion located with a dotted black circle at frequencies of: (a) 16 Hz; (b) 24 Hz; (c) 32 Hz; and (d) 40 Hz

Figure 7.7 shows the results for the 20 mm inclusion at location B, 12 mm from the centre of the phantom. Half of the phantom surface is affected and shows smaller average radial displacement compared to the other side. The black thick line divides the phantom to clearly indicate the side affected by the inclusion, and the healthy side. In contrast, the 10 mm inclusion in Figure 7.4 showed a much smaller affected region. Finally, Figure 7.8 shows the case with the 20 mm inclusion inserted near the actuator in location C. These results and others indicate that the inclusion is near to the phantom surface, a greater region will be affected by the inclusion.

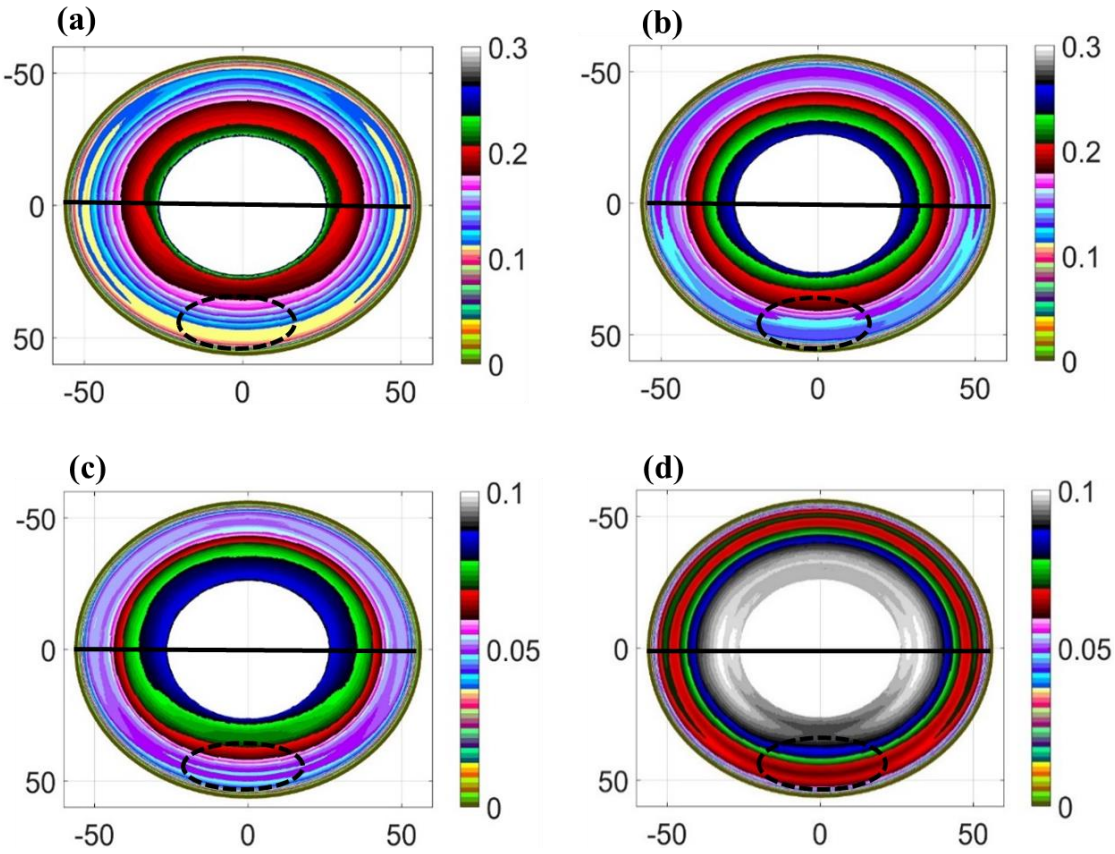

Figure 7.7: Location B: Average radial displacement distribution (all units in mm) for a 20 mm inclusion located with a dotted black circle at frequencies of: (a) 16 Hz; (b) 24 Hz; (c) 32 Hz; and (d) 40 Hz

The overall results are promising for diagnostics and show robustness to location chosen. In general, the larger the inclusion, the greater the area affected. Equally, the deeper the inclusion, the smaller the area affected. Thus, the average radial displacement varies throughout the phantom surface as a function of inclusion location and actuation frequency. These results all match expectations and prior experimental results [27, 32].

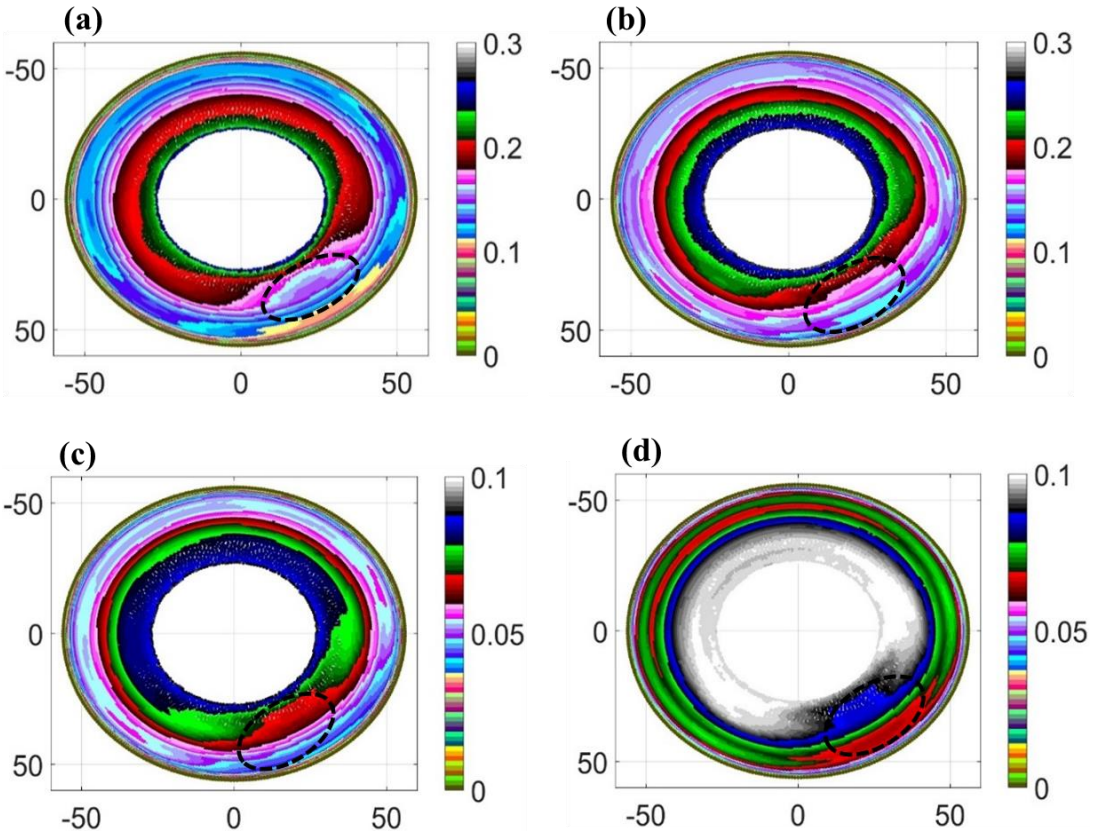

Figure 7.8: Location C: Average radial displacement distribution (all units in mm) for a 20 mm inclusion located with a dotted black circle at frequencies of: (a) 16 Hz; (b) 24 Hz; (c) 32 Hz; and (d) 40 Hz

7.5 Summary

The same FE modelling procedure validated in Chapter 4 and 5 was used to model new phantoms with 20 mm and 10 mm diameter stiff inclusions and at different positions. The goal was to assess the sensitivity and robustness of surface motion with inclusion position and actuation frequency. The results show inclusions can be identified with surface motion at every frequency using average radial displacement to locate stiffer inclusions. Average radial displacement varies with changing inclusion position. Thus, these results can help DIET screening diagnostic development by reducing extensive phantom testing to a series of FE analysis.

Chapter 8: Conclusions

Breast cancer is a major health issue. Globally, millions of women are diagnosed with breast cancer and many of them die every year globally. Early detection of breast cancer improves treatment effectiveness and enhances the odds of survival. The most typical breast cancer screening methods, include MRI and mammography. However, due to drawbacks and limitations around cost, discomfort, and invasiveness, there is need of better screening techniques.

Digital imaged elasto-tomography (DIET) has been developed to overcome some of the limitations of current techniques. This technique enables non-invasive, low-cost screening, which could enable earlier detection of breast cancer. Combined with effective treatment, early detection is proven to reduce both mortality and the total cost of cancer screening and care. Thus, DIET offers a significant potential improvement in the ability to screen for cancer and improve outcomes.

The research presented in this thesis addresses three major significant issues hindering DIET development. These issues include the lack of a rapid ability to develop the system with an over reliance on clinical testing and technology improvement, which is slow and can be skewed by outlying response. Equally, a clinical testing approach does not allow re-testing easily when systems are improved, so that improvements cannot be well-quantified. Finally, the current prototypes measure surface motions with advanced algorithms. However, their exact error is not known as it has been difficult to validate to a gold standard measurement,

which limits the ability to determine if surface motion based diagnostics have the resolution to detect stiffer inclusions within the error induced by measurement error of surface motions.

Thus, this thesis directly examines: a) the development of more realistic tissue mimicking breast phantoms using silicone materials; b) validation and quantification of the error of the surface motion measurements and algorithms; and c) finite element modelling of silicone phantoms, which would provide a faster approach to development, as finite element methods could provide "data" far faster and then be validated in limited phantom experiments, all before clinical validation and testing.

The aim for the first issue was to find the most suitable commonly available material to mimic breast tissue, for use in DIET development. The linear and nonlinear mechanical properties of agar, gelatin, and silicone materials are measured and compared with real breast tissue values from the literature to develop a best formulation that offered repeatability and good representation of the tissue material properties. Two widely recognised measurement procedures are used. Quasi-static uniaxial compression was performed under a strain rate of 0.5 mm/min up to 15% strain with preloads of 0.05 N, 0.1 N, and 0.2 N, was used to measure the elastic moduli. Dynamic testing over a frequency range of 0.1-50 Hz for agar and 0.1-100 Hz for gelatin and silicone with the same preload was used to measure the storage moduli. Elastic and storage moduli were (5-81 kPa, 17-85 kPa, 5-112 kPa) and (3-128 kPa, 10-109 kPa, 5-73 kPa) for agar, gelatine, and silicone, respectively at the three preloads. Finally, breast shaped mimicking silicone phantoms were fabricated for in vitro trials of a DIET breast cancer screening system assessing changes in mechanical properties. These results thus enable easily fabricated and repeatable testable tissue mimicking breast phantoms for developing DIET motion sensing technology and cancer detection diagnostics.

Finite element modelling and laser Doppler vibrometry are presented to quantify errors and validate current optical flow algorithm, based on surface displacements of the breast phantom using a laser-based gold standard measurement, which is important, as surface motion is the key diagnostic metric in the DIET concept. Finite element modelling results showed good to strong correlation ranging from 0.7 to 1.0 in all cases with over 90% having a value over 0.9. Magnitudes for each frame of the dynamic response also matched well, indicating the material properties and geometry were accurate enough to provide this level of correlation. The results from the optical flow motion algorithm used with DIET and a laser Doppler vibrometer show the optical flow algorithm captures surface motion of breast shaped silicone phantoms with good accuracy. Thus, measurement error was quantified and found to be on the order of 10um or less. This value can thus be used to quantify the range of error of any motion-based diagnostics developed. The optical flow algorithm is thus suitable and robust enough for use in clinical breast screening.

These first two outcomes justified the development of FE models to generate data for development, prior to phantom testing, saving further time and experimental effort. Results showed good correlation throughout the dynamic response cycle between experimental and FE model results. In particular, the results of further FE modelling also show inclusions can be localised and detected, and these results can help in development of DIET screening diagnostics. Thus, the results justify the use of FE model data in lieu of experimental phantom data for development. The overall modelling approach was also relatively simple, and could thus potentially be generalised to human breast geometries in further work.

In summary, all these major significant issues which impeding DIET development were successfully addressed. All of these requirement enable faster and more robust development of the technology and can potentially be generalised further.

Chapter 9: Future work

9.1 Complex breast phantom

Real human breast tissue is complex and contains different kind of tissues such as fatty, glandular and fibrous tissues. Current fabricated phantoms have only skin, adipose and cancerous tissues. Fabricating different sizes of homogenous and heterogeneous breast phantoms by adding glandular and fibrous tissues would benefit future research endeavours in the development of DIET screening methods. Considering and investigating mechanical properties of different types of silicone materials for glandular and fibrous tissues which should match real breast tissues would help in making heterogeneous breast phantom.

There were only one material considered for cancerous tissues. Investigation the mechanical properties of benign and malignant tumors and creating phantoms that resemble both benign and malignant tumors would be another recommendation.

9.2 Finite element modelling of complex breast phantom

In DIET experimental data, two preload force applied on breast phantoms, a 2N and a 4N preload. In this thesis, only 2N preload data of DIET and finite element methods were validated. In future work the validation process can also be performed for 4N preload.

Same procedure can be follow to validate DIET experimental results and finite element method for more realistic and complex breast phantom by adding fibrous and glandular

tissues. It is also recommended that inserting benign and malignant types of tumors be investigated.

9.3 Other measurement methods

Using other measurement methods to analyse surface motion of the breast phantoms would be recommended. In this thesis single point laser Doppler vibrometer was used to measured horizontal displacement on the phantom surface, in future 3D laser scanning can be used to measure 3D displacements at phantom surface.

Edge detection technique is another method to extract features from an image. Because edges provide connectivity information between nodes, and curved lines. The majority of common edge detection techniques detect edges by calculating the gradient or first partial derivatives in the horizontal and vertical directions of the image. Edge detection algorithms which utilize first derivative operators include the Roberts, Prewitt, Sobel, Frei-Chen, and Canny algorithms. DIET captures 50 images from different camera angles at different phase. Multi-view data collection can be used to interpolate the 3D surface motion of the breast phantoms.

References

[1] A. Jemal, F. Bray, M. M. Center, J. Ferlay, E. Ward, and D. Forman, "Global cancer statistics," *CA: a cancer journal for clinicians,* vol. 61, pp. 69-90, 2011.

[2] Globocan. (2012). *Estimated Cancer Incidence, Mortality and Prevalence Worldwide.* Available: http://globocan.iarc.fr/Pages/fact_sheets_cancer.aspx

[3] N. Z. M. o. Health, "Cancer: New registrations and deaths 2012," 06 October 2015.

[4] A. Jemal, R. Siegel, E. Ward, T. Murray, J. Xu, and M. J. Thun, "Cancer statistics, 2007," *CA: a cancer journal for clinicians,* vol. 57, pp. 43-66, 2007.

[5] A. C. Society. (2015). *Cancer Facts and Figures 2015. Atlanta, Ga: American Cancer Society,* . Available: www.cancer.org/acs/groups/content/@editorial/documents/document/acspc-044552.pdf

[6] A. C. Society. (2004-2014). *Breast Cancer Facts & Figures.* Available: http://www.cancer.org/research/cancerfactsstatistics/breast-cancer-facts-figures

[7] X. Zhou and R. Gordon, "Detection of early breast cancer: an overview and future prospects," *Critical reviews in biomedical engineering,* vol. 17, pp. 203-255, 1988.

[8] F. McKenzie, L. Ellison-Loschmann, and M. Jeffreys, "Investigating reasons for socioeconomic inequalities in breast cancer survival in New Zealand," *Cancer epidemiology,* vol. 34, pp. 702-708, 2010.

[9] D. Cormack, B. Robson, G. Purdie, M. Ratima, and R. Brown, "Access to cancer services for Maori," *Wellington: Ministry of Health,* 2005.

[10] A. Jemal, R. Siegel, E. Ward, Y. Hao, J. Xu, T. Murray*, et al.*, "Cancer statistics, 2008," *CA: a cancer journal for clinicians,* vol. 58, pp. 71-96, 2008.

[11] M. M. Tilanus-Linthorst, I. M. M. Obdeijn, K. C. Bartels, H. J. de Koning, and M. Oudkerk, "First experiences in screening women at high risk for breast cancer with MR imaging," *Breast cancer research and treatment,* vol. 63, pp. 53-60, 2000.

[12] J. D. Boice Jr, C. E. Land, R. E. Shore, J. E. Norman, and M. Tokunaga, "Risk of Breast Cancer Following Low-Dose Radiation Exposure 1," *Radiology,* vol. 131, pp. 589-597, 1979.

[13] R. E. Gross, "Breast cancer: risk factors, screening, and prevention," in *Seminars in oncology nursing*, 2000, pp. 176-184.

[14] C. G. o. H. F. i. B. Cancer, "Menarche, menopause, and breast cancer risk: individual participant meta-analysis, including 118 964 women with breast cancer from 117 epidemiological studies," *The lancet oncology,* vol. 13, pp. 1141-1151, 2012.

[15] S. Opdahl, M. Alsaker, I. Janszky, P. Romundstad, and L. Vatten, "Joint effects of nulliparity and other breast cancer risk factors," *British journal of cancer,* vol. 105, p. 731, 2011.

[16] A. B. Mariotto, K. R. Yabroff, Y. Shao, E. J. Feuer, and M. L. Brown, "Projections of the cost of cancer care in the United States: 2010–2020," *Journal of the National Cancer Institute,* 2011.

[17] R. Sullivan, J. Peppercorn, K. Sikora, J. Zalcberg, N. J. Meropol, E. Amir*, et al.*, "Delivering affordable cancer care in high-income countries," *The lancet oncology,* vol. 12, pp. 933-980, 2011.

[18] S. Ray, V. Bonthapally, D. McMorrow, M. Bonafede, and P. Landsman-Blumberg, "Patterns of treatment, healthcare utilization and costs by lines of therapy in metastatic breast cancer in a large insured US population," *Journal of comparative effectiveness research,* vol. 2, pp. 195-206, 2013.

[19] C. J. Rosenquist and K. K. Lindfors, "Screening mammography in women aged 40-49 years: analysis of cost-effectiveness," *Radiology,* vol. 191, pp. 647-650, 1994.
[20] S. A. Feig, "Mammographic screening of women aged 40–49 years. Benefit, risk, and cost considerations," *Cancer,* vol. 76, pp. 2097-2106, 1995.
[21] S. V. Sree, E. Y.-K. Ng, R. U. Acharya, and O. Faust, "Breast imaging: a survey," *World journal of clinical oncology,* vol. 2, p. 171, 2011.
[22] M. Bushra and S. Muhammad, "Automated Detection of Breast Tumor in Different Imaging Modalities: A Review," *Current Medical Imaging Reviews,* vol. 12, pp. 1-19, 2016.
[23] I. Hina Muhammad, G. P. Christopher, K. S. Matthew, H. Marcus, and J. G. Chase, "Attributes, Performance, and Gaps in Current & Emerging Breast Cancer Screening Technologies," *Current Medical Imaging Reviews,* vol. 13, pp. 1-10, 2017.
[24] R. N. Strickland, *Image-processing techniques for tumor detection*: CRC Press, 2002.
[25] A. Peters, A. Milsant, J. Rouzé, L. Ray, J. G. Chase, and E. E. W. V. Houten, "Digital image-based elasto-tomography: proof of concept studies for surface based mechanical property reconstruction," *JSME International Journal Series C Mechanical Systems, Machine Elements and Manufacturing,* vol. 47, pp. 1117-1123, 2004.
[26] A. Peters, J. G. Chase, and E. E. W. Van Houten, "Estimating elasticity in heterogeneous phantoms using Digital Image Elasto-Tomography," *Medical & Biological Engineering & Computing,* vol. 47, pp. 67-76, 2009.
[27] A. S. Kashif, T. F. Lotz, A. M. Heeren, and J. G. Chase, "Separate modal analysis for tumor detection with a digital image elasto tomography (DIET) breast cancer screening system," *Medical physics,* vol. 40, p. 113503, 2013.
[28] C. Zhou, J. G. Chase, H. Ismail, C. Pretty, G. W. Rodgers, M. K. Signal*, et al.*, "Nominal Stiffness Identification for Tumor Detection of Women Breast in a Digital Image Elasto Tomography (DIET) System," *IFAC-PapersOnLine,* vol. 50, pp. 2031-2036, 2017.
[29] C. Zhou, J. G. Chase, H. Ismail, G. W. Rodgers, C. Pretty, M. Signal*, et al.*, "A Surface Vibration-based Method for Tumor Detection of Women Breast in a DIET System," *Procedia Engineering,* vol. 199, pp. 310-315, 2017/01/01/ 2017.
[30] C. Zhou, J. G. Chase, H. Ismail, M. K. Signal, M. Haggers, G. W. Rodgers*, et al.*, "Silicone phantom validation of breast cancer tumor detection using nominal stiffness identification in digital imaging elasto-tomography (DIET)," *Biomedical Signal Processing and Control,* vol. 39, pp. 435-447, 2018.
[31] C. E. Hann, J. G. Chase, X. Chen, C. Berg, R. G. Brown, and R. B. Elliot, "Strobe imaging system for digital image-based elasto-tomography breast cancer screening," *IEEE Transactions on Industrial Electronics,* vol. 56, pp. 3195-3202, 2009.
[32] A. Peters, S. Wortmann, R. Elliott, M. Staiger, J. G. Chase, and E. V. Houten, "Digital image-based elasto-tomography: first experiments in surface based mechanical property estimation of gelatine phantoms," *JSME International Journal Series C Mechanical Systems, Machine Elements and Manufacturing,* vol. 48, pp. 562-569, 2005.
[33] R. G. Brown, C. E. Hann, and J. G. Chase, "Vision-based 3D surface motion capture for the DIET breast cancer screening system," in *Mechatronics and Machine Vision in Practice, 2008. M2VIP 2008. 15th International Conference on*, 2008, pp. 628-633.
[34] R. G. Brown, J. G. Chase, and C. E. Hann, "A pointwise smooth surface stereo reconstruction algorithm without correspondences," *Image and Vision Computing,* vol. 30, pp. 619-629, 2012.
[35] R. Brown, C. Hann, J. G. Chase, and L. Ray, "Discrete color-based Euclidean-invariant signatures for feature tracking in a DIET breast cancer screening system," in *Medical Imaging*, 2007, pp. 65110D-65110D-9.
[36] E. E. Van Houten, A. Peters, and J. G. Chase, "Phantom elasticity reconstruction with Digital Image Elasto-Tomography," *Journal of the mechanical behavior of biomedical materials,* vol. 4, pp. 1741-1754, 2011.

[37] E. K. Arleo, R. E. Hendrick, M. A. Helvie, and E. A. Sickles, "Comparison of recommendations for screening mammography using CISNET models," *Cancer,* vol. 123, pp. 3673-3680, 2017.
[38] S. Pandya and R. G. Moore, "Breast development and anatomy," *Clinical obstetrics and gynecology,* vol. 54, pp. 91-95, 2011.
[39] J. M. B. Pang, K. L. Gorringe, and S. B. Fox, "Ductal carcinoma in situ–update on risk assessment and management," *Histopathology,* vol. 68, pp. 96-109, 2016.
[40] G. J. Whitman, D. G. Sheppard, M. J. Phelps, and B. N. Gonzales, "Breast cancer staging," in *Seminars in roentgenology*, 2006, pp. 91-104.
[41] C. S. N. Zealand. *What is breast cancer*. Available: https://canterbury-west-coast.cancernz.org.nz/cancer-information/cancer-types/breast-cancer/what-is-breast-cancer/
[42] A. A. Muggerud, M. Hallett, H. Johnsen, K. Kleivi, W. Zhou, S. Tahmasebpoor*, et al.*, "Molecular diversity in ductal carcinoma in situ (DCIS) and early invasive breast cancer," *Molecular Oncology,* vol. 4, pp. 357-368, 2010/08/01/ 2010.
[43] C. F. Cowell, B. Weigelt, R. A. Sakr, C. K. Y. Ng, J. Hicks, T. A. King*, et al.*, "Progression from ductal carcinoma in situ to invasive breast cancer: Revisited," *Molecular Oncology,* vol. 7, pp. 859-869, 2013.
[44] "Breast," in *AJCC Cancer Staging Manual*, F. L. Greene, D. L. Page, I. D. Fleming, A. G. Fritz, C. M. Balch, D. G. Haller*, et al.*, Eds., ed New York, NY: Springer New York, 2002, pp. 223-240.
[45] S. F. Hurley and J. M. Kaldor, "The benefits and risks of mammographic screening for breast cancer," *Epidemiologic Reviews,* vol. 14, pp. 101-130, 1992.
[46] A. B. de González and G. Reeves, "Mammographic screening before age 50 years in the UK: comparison of the radiation risks with the mortality benefits," *British journal of cancer,* vol. 93, pp. 590-596, 2005.
[47] J. G. Elmore, K. Armstrong, C. D. Lehman, and S. W. Fletcher, "Screening for breast cancer," *Jama,* vol. 293, pp. 1245-1256, 2005.
[48] A. Qaseem, V. Snow, K. Sherif, M. Aronson, K. B. Weiss, and D. K. Owens, "Screening mammography for women 40 to 49 years of age: a clinical practice guideline from the American College of Physicians," *Annals of internal medicine,* vol. 146, pp. 511-515, 2007.
[49] J. S. Mandelblatt, K. A. Cronin, S. Bailey, D. A. Berry, H. J. de Koning, G. Draisma*, et al.*, "Effects of mammography screening under different screening schedules: model estimates of potential benefits and harms," *Annals of internal medicine,* vol. 151, pp. 738-747, 2009.
[50] M. Løberg, M. L. Lousdal, M. Bretthauer, and M. Kalager, "Benefits and harms of mammography screening," *Breast Cancer Research,* vol. 17, pp. 1-12, 2015.
[51] G. I. Andreea, R. Pegza, L. Lascu, S. Bondari, Z. Stoica, and A. Bondari, "The role of imaging techniques in diagnosis of breast cancer," *Curr Health Sci J,* vol. 37, pp. 55-61, 2011.
[52] R. G. Blanks, T. P. Marshall, J. Nottingham, J. Patnick, and H. Thornton, "Women need better information on routine mammography," *British Medical Journal,* vol. 327, pp. 868-868, 2003.
[53] G. T. Barnes, "Mammography equipment: compression, scatter control, and automatic exposure control," *Syllabus: a categorical course in physics,* pp. 73-82, 1993.
[54] L. Robinson, P. Hogg, and A. Newton-Hughes, "The power and the pain: Mammographic compression research from the service-users' perspective," *Radiography,* vol. 19, pp. 190-195, 2013.
[55] J. Bai, Z. He, J. Dong, G. Yao, H. Chen, and K. Li, "Correlation of pain experience during mammography with factors of breast density and breast compressed thickness," *Journal of Shanghai Jiaotong University (Medical Science),* vol. 30, p. 1062, 2010.
[56] S. A. Feig, "Adverse effects of screening mammography," *Radiologic Clinics of North America,* vol. 42, pp. 807-819, 2004.

[57] D. Miller, V. Livingstone, and P. Herbison, "Interventions for relieving the pain and discomfort of screening mammography," *Cochrane Database Syst Rev,* vol. 1, 2008.

[58] S. Kashikar-Zuck, F. J. Keefe, P. Kornguth, P. Beaupre, A. Holzberg, and D. Delong, "Pain coping and the pain experience during mammography: a preliminary study," *Pain,* vol. 73, pp. 165-172, 1997.

[59] A. M. Myklebust, T. Seierstad, E. Stranden, and A. Lerdal, "Level of satisfaction during mammography screening in relation to discomfort, service provided, level of pain and breast compression," *European Journal of Radiography,* vol. 1, pp. 66-72, 2009.

[60] C. M. Vachon, K. R. Brandt, K. Ghosh, C. G. Scott, S. D. Maloney, M. J. Carston*, et al.*, "Mammographic breast density as a general marker of breast cancer risk," *Cancer Epidemiology Biomarkers & Prevention,* vol. 16, pp. 43-49, 2007.

[61] J. A. Harvey and V. E. Bovbjerg, "Quantitative assessment of mammographic breast density: relationship with breast cancer risk 1," *Radiology,* vol. 230, pp. 29-41, 2004.

[62] N. F. Boyd, L. J. Martin, M. J. Yaffe, and S. Minkin, "Mammographic density: a hormonally responsive risk factor for breast cancer," *British Menopause Society Journal,* vol. 12, pp. 186-193, 2006.

[63] C. A. Haiman, L. Bernstein, D. Berg, S. A. Ingles, M. Salane, and G. Ursin, "Genetic determinants of mammographic density," *Breast Cancer Res,* vol. 4, p. R5, 2002.

[64] J. E. Joy, E. E. Penhoet, and D. B. Petitti, "Benefits and Limitations of Mammography," 2005.

[65] I. Saarenmaa, T. Salminen, U. Geiger, P. Heikkinen, S. Hyvärinen, J. Isola*, et al.*, "The effect of age and density of the breast on the sensitivity of breast cancer diagnostic by mammography and ultasonography," *Breast cancer research and treatment,* vol. 67, pp. 117-123, 2001.

[66] M. L. Burman, S. H. Taplin, D. F. Herta, and J. G. Elmore, "Effect of false-positive mammograms on interval breast cancer screening in a health maintenance organization," *Annals of internal medicine,* vol. 131, pp. 1-6, 1999.

[67] N. Ohuchi, A. Suzuki, T. Sobue, M. Kawai, S. Yamamoto, Y.-F. Zheng*, et al.*, "Sensitivity and specificity of mammography and adjunctive ultrasonography to screen for breast cancer in the Japan Strategic Anti-cancer Randomized Trial (J-START): a randomised controlled trial," *The Lancet,* 2015.

[68] J. E. Martin, M. Moskowitz, and J. R. Milbrath, "Breast cancer missed by mammography," *American Journal of Roentgenology,* vol. 132, pp. 737-739, 1979.

[69] R. E. Bird, T. W. Wallace, and B. C. Yankaskas, "Analysis of cancers missed at screening mammography," *Radiology,* vol. 184, pp. 613-617, 1992.

[70] L. Kallsher, "Factors influencing false negative rates in xeromammography," *Radiology,* vol. 133, pp. 297-301, 1979.

[71] S. K. Goergen, J. Evans, G. Cohen, and J. H. MacMillan, "Characteristics of breast carcinomas missed by screening radiologists," *Radiology,* vol. 204, pp. 131-135, 1997.

[72] R. Holland, J. Hendriks, and M. Mravunac, "Mammographically occult breast cancer: a pathologic and radiologic study," *Cancer,* vol. 52, pp. 1810-1819, 1983.

[73] M. Kriege, C. T. Brekelmans, C. Boetes, P. E. Besnard, H. M. Zonderland, I. M. Obdeijn*, et al.*, "Efficacy of MRI and mammography for breast-cancer screening in women with a familial or genetic predisposition," *New England Journal of Medicine,* vol. 351, pp. 427-437, 2004.

[74] F. Sardanelli, F. Podo, G. D'Agnolo, A. Verdecchia, M. Santaquilani, R. Musumeci*, et al.*, "Multicenter Comparative Multimodality Surveillance of Women at Genetic-Familial High Risk for Breast Cancer (HIBCRIT Study): Interim Results 1," *Radiology,* vol. 242, pp. 698-715, 2007.

[75] J. L. Jesneck, J. Y. Lo, and J. A. Baker, "Breast Mass Lesions: Computer-aided Diagnosis Models with Mammographic and Sonographic Descriptors 1," *Radiology,* vol. 244, pp. 390-398, 2007.
[76] J. M. Seely, "Management of breast magnetic resonance imaging-detected lesions," *Canadian Association of Radiologists Journal,* vol. 63, pp. 192-206, 2012.
[77] V. L. Ernster, R. Ballard-Barbash, W. E. Barlow, Y. Zheng, D. L. Weaver, G. Cutter*, et al.*, "Detection of ductal carcinoma in situ in women undergoing screening mammography," *Journal of the National Cancer Institute,* vol. 94, pp. 1546-1554, 2002.
[78] P. Skrabanek, "The cost-effectiveness of breast cancer screening," *International journal of technology assessment in health care,* vol. 7, pp. 633-635, 1991.
[79] M. L. Brown, "Economic considerations in breast cancer screening of older women," *Journal of gerontology,* vol. 47, pp. 51-58, 1992.
[80] A. Elixhauser, "Costs of breast cancer and the cost-effectiveness of breast cancer screening," *International journal of technology assessment in health care,* vol. 7, pp. 604-615, 1991.
[81] A. I. Mushlin and L. Fintor, "Is screening for breast cancer cost-effective?," *Cancer,* vol. 69, pp. 1957-1962, 1992.
[82] I. Okubo, H. Glick, H. Frumkin, and J. M. Eisenberg, "Cost-effectiveness analysis of mass screening for breast cancer in Japan," *Cancer,* vol. 67, pp. 2021-2029, 1991.
[83] T. N. Z. B. C. Foundation. Available: http://nzbcf.org.nz/BREASTCANCER/Mammograms/WhatShouldIDo.aspx
[84] A. Miller, "The costs and benefits of breast cancer screening," *American journal of preventive medicine,* vol. 9, pp. 175-180, 1992.
[85] P. J. Van Der Maas, H. J. De Koning, V. Ineveld, B. Martin, G. J. Van Oortmarssen, J. D. F. Habbema*, et al.*, "The cost-effectiveness of breast cancer screening," *International Journal of Cancer,* vol. 43, pp. 1055-1060, 1989.
[86] H. J. de Koning, B. Martin van Ineveld, G. J. van Oortmarssen, J. De Haes, H. J. Collette, J. H. Hendriks*, et al.*, "Breast cancer screening and cost-effectiveness; policy alternatives, quality of life considerations and the possible impact of uncertain factors," *International Journal of Cancer,* vol. 49, pp. 531-537, 1991.
[87] N. Houssami and D. L. Miglioretti, "Digital breast tomosynthesis: a brave new world of mammography screening," *JAMA oncology,* vol. 2, pp. 725-727, 2016.
[88] N. Houssami and P. Skaane, "Overview of the evidence on digital breast tomosynthesis in breast cancer detection," *The Breast,* vol. 22, pp. 101-108, 2013.
[89] S. M. Friedewald, "Breast Tomosynthesis: Practical Considerations," *Radiologic Clinics of North America,* 2017.
[90] G. van Schie, R. Mann, M. Imhof-Tas, and N. Karssemeijer, "Generating synthetic mammograms from reconstructed tomosynthesis volumes," *IEEE transactions on medical imaging,* vol. 32, pp. 2322-2331, 2013.
[91] J. Melnikow, J. J. Fenton, D. Miglioretti, E. P. Whitlock, and M. S. Weyrich, "Screening for Breast Cancer With Digital Breast Tomosynthesis," 2016.
[92] M. R. B. Imaging. *The Breast Health Resource* Available: http://imaginis.com/breasthealth/mri.asp.
[93] A. Berger, "How does it work?: Magnetic resonance imaging," *BMJ: British Medical Journal,* vol. 324, p. 35, 2002.
[94] J. Safir, J. L. Zito, M. E. Gershwind, D. Faegenburg, C. E. Tobin, P. D. Cayea*, et al.*, "Contrast-enhanced breast mri for cancer detection using a commercially available system—a perspective," *Clinical imaging,* vol. 22, pp. 162-179, 1998.
[95] E. Warner, D. Plewes, R. Shumak, G. Catzavelos, L. Di Prospero, M. Yaffe*, et al.*, "Comparison of breast magnetic resonance imaging, mammography, and ultrasound for surveillance of women at high risk for hereditary breast cancer," *Journal of Clinical Oncology,* vol. 19, pp. 3524-3531, 2001.

[96] C. Laura, M. Elisabetta De, S. Federica, T. Angela, M. Isabella, B. Rachele, *et al.*, "Radiological Screening Programs for Women at High Risk of Developing Breast Cancer," *Current Women`s Health Reviews,* vol. 8, pp. 72-85, 2012.

[97] E. A. Morris, "Rethinking breast cancer screening: ultra fast breast magnetic resonance imaging," *Journal of Clinical Oncology,* vol. 32, pp. 2281-2283, 2014.

[98] W. A. Berg, "Tailored supplemental screening for breast cancer: what now and what next?," *American Journal of Roentgenology,* vol. 192, pp. 390-399, 2009.

[99] L. Kovacs, M. Eder, R. Hollweck, A. Zimmermann, M. Settles, A. Schneider, *et al.*, "Comparison between breast volume measurement using 3D surface imaging and classical techniques," *The Breast,* vol. 16, pp. 137-145, 2007.

[100] J. B. Sutcliffe and P. M. Otto, "Controversies in breast MRI," *Current problems in diagnostic radiology,* vol. 42, pp. 149-163, 2013.

[101] S. Harms, D. Flamig, K. Hesley, M. Meiches, R. Jensen, W. Evans, *et al.*, "MR imaging of the breast with rotating delivery of excitation off resonance: clinical experience with pathologic correlation," *Radiology,* vol. 187, pp. 493-501, 1993.

[102] S. Uma, S. Raju, and R. J. Naranamangalam, "Characterization of Breast Lesions by Magnetic Resonance Imaging (MRI) and Spectroscopy (MRS)," *Current Medical Imaging Reviews,* vol. 2, pp. 329-340, 2006.

[103] P. C. Stomper, S. Herman, D. L. Klippenstein, J. S. Winston, S. B. Edge, M. A. Arredondo, *et al.*, "Suspect breast lesions: findings at dynamic gadolinium-enhanced MR imaging correlated with mammographic and pathologic features," *Radiology,* vol. 197, pp. 387-395, 1995.

[104] C. D. Lehman, C. Gatsonis, C. K. Kuhl, R. E. Hendrick, E. D. Pisano, L. Hanna, *et al.*, "MRI evaluation of the contralateral breast in women with recently diagnosed breast cancer," *New England Journal of Medicine,* vol. 356, pp. 1295-1303, 2007.

[105] S. Lord, W. Lei, P. Craft, J. Cawson, I. Morris, S. Walleser, *et al.*, "A systematic review of the effectiveness of magnetic resonance imaging (MRI) as an addition to mammography and ultrasound in screening young women at high risk of breast cancer," *European journal of cancer,* vol. 43, pp. 1905-1917, 2007.

[106] B. Choi, H. Kim, E. Kim, B.-s. Kim, J.-Y. Han, S.-S. Yoo, *et al.*, "New subtraction algorithms for evaluation of lesions on dynamic contrast-enhanced MR mammography," *European radiology,* vol. 12, pp. 3018-3022, 2002.

[107] A. Rim, M. Chellman-Jeffers, and A. Fanning, "Trends in breast cancer screening and diagnosis," *Cleveland Clinic journal of medicine,* vol. 75, p. S2, 2008.

[108] S. A. Langer, K. C. Horst, D. M. Ikeda, B. L. Daniel, C. S. Kong, and F. M. Dirbas, "Pathologic correlates of false positive breast magnetic resonance imaging findings: which lesions warrant biopsy?," *The American journal of surgery,* vol. 190, pp. 633-640, 2005.

[109] R. M. Mann, C. K. Kuhl, K. Kinkel, and C. Boetes, "Breast MRI: guidelines from the European society of breast imaging," *European radiology,* vol. 18, pp. 1307-1318, 2008.

[110] C. K. Kuhl, P. Mielcareck, S. Klaschik, C. Leutner, E. Wardelmann, J. r. Gieseke, *et al.*, "Dynamic breast mr imaging: Are signal intensity time course data useful for differential diagnosis of enhancing lesions? 1," *Radiology,* vol. 211, pp. 101-110, 1999.

[111] R. Woodhams, S. Ramadan, P. Stanwell, S. Sakamoto, H. Hata, M. Ozaki, *et al.*, "Diffusion-weighted imaging of the breast: principles and clinical applications," *Radiographics,* vol. 31, pp. 1059-1084, 2011.

[112] C. Westra, V. Dialani, T. S. Mehta, and R. L. Eisenberg, "Using T2-weighted sequences to more accurately characterize breast masses seen on MRI," *American Journal of Roentgenology,* vol. 202, pp. W183-W190, 2014.

[113] A. P. Carpenter, L. M. Leemis, A. S. Papir, D. J. Phillips, and G. S. Phillips, "Managing magnetic resonance imaging machines: support tools for scheduling and planning," *Health care management science,* vol. 14, pp. 158-173, 2011.

[114] S. Saadatmand, M. M. Tilanus-Linthorst, E. J. Rutgers, N. Hoogerbrugge, J. C. Oosterwijk, R. A. Tollenaar*, et al.*, "Cost-effectiveness of screening women with familial risk for breast cancer with magnetic resonance imaging," *Journal of the National Cancer Institute,* vol. 105, pp. 1314-1321, 2013.
[115] S. Rankin, "MRI of the breast," *The British journal of radiology,* vol. 73, pp. 806-818, 2000.
[116] C. K. Kuhl and H. H. Schild, "Dynamic image interpretation of MRI of the breast," *Journal of Magnetic Resonance Imaging,* vol. 12, pp. 965-974, 2000.
[117] S. Edell and M. Eisen, "Current imaging modalities for the diagnosis of breast cancer," *Delaware medical journal,* vol. 71, pp. 377-382, 1999.
[118] J. Hardy, T. Powles, I. Judson, C. Heron, M. Williams, G. Cherryman*, et al.*, "How many tests are required in the diagnosis of palpable breast abnormalities?," *Clinical Oncology,* vol. 2, pp. 148-152, 1990.
[119] H. A. Moss, P. D. Britton, C. D. Flower, A. H. Freeman, D. J. Lomas, and R. M. Warren, "How reliable is modern breast imaging in differentiating benign from malignant breast lesions in the symptomatic population?," *Clinical radiology,* vol. 54, pp. 676-682, 1999.
[120] P. Skaane, K. Engedal, and A. Skjennald, "Interobserver variation in the interpretation of breast imaging: comparison of mammography, ultrasonography, and both combined in the interpretation of palpable noncalcified breast masses," *Acta Radiologica,* vol. 38, pp. 497-502, 1997.
[121] I. Khalkhali and H. Vargas, "Practical use of ultrasound at a dedicated breast center," *The breast journal,* vol. 11, pp. 165-166, 2005.
[122] H. Madjar, "Role of breast ultrasound for the detection and differentiation of breast lesions," *Breast Care,* vol. 5, pp. 109-114, 2010.
[123] B. D. FORNAGE, "Local and Regional Staging of Invasive Breast Cancer With Sonography: 25 Years of Practice at MD Anderson Cancer Center," *Oncologist,* vol. 19, pp. 5-15, 2014.
[124] R. A. Smith, D. Saslow, K. A. Sawyer, W. Burke, M. E. Costanza, W. Evans*, et al.*, "American Cancer Society guidelines for breast cancer screening: update 2003," *CA: a cancer journal for clinicians,* vol. 53, pp. 141-169, 2003.
[125] M. Haloua, N. Krekel, V. Coupé, J. Bosmans, A. L. Cardozo, S. Meijer*, et al.*, "Ultrasound-guided surgery for palpable breast cancer is cost-saving: Results of a cost-benefit analysis," *The Breast,* vol. 22, pp. 238-243, 2013.
[126] S. K. Moore, "Better breast cancer detection," *Spectrum, IEEE,* vol. 38, pp. 50-54, 2001.
[127] F. Arena, C. Barone, and T. DiCicco, "Use of digital infrared imaging in enhanced breast cancer detection and monitoring of the clinical response to treatment," in *Engineering in Medicine and Biology Society, 2003. Proceedings of the 25th Annual International Conference of the IEEE*, 2003, pp. 1129-1132.
[128] T. M. Kolb, J. Lichy, and J. H. Newhouse, "Occult cancer in women with dense breasts: detection with screening US--diagnostic yield and tumor characteristics," *Radiology,* vol. 207, pp. 191-199, 1998.
[129] W. A. Berg, Z. Zhang, D. Lehrer, R. A. Jong, E. D. Pisano, R. G. Barr*, et al.*, "Detection of breast cancer with addition of annual screening ultrasound or a single screening MRI to mammography in women with elevated breast cancer risk," *Jama,* vol. 307, pp. 1394-1404, 2012.
[130] M. S. Soo, J. A. Baker, and E. L. Rosen, "Sonographic detection and sonographically guided biopsy of breast microcalcifications," *American Journal of Roentgenology,* vol. 180, pp. 941-948, 2003.
[131] W. Buchberger, P. DeKoekkoek-Doll, P. Springer, P. Obrist, and M. Dünser, "Incidental findings on sonography of the breast: clinical significance and diagnostic workup," *AJR. American journal of roentgenology,* vol. 173, pp. 921-927, 1999.

[132] E. A. Sickles, R. A. Filly, and P. W. Callen, "Breast cancer detection with sonography and mammography: comparison using state-of-the-art equipment," *American Journal of Roentgenology,* vol. 140, pp. 843-845, 1983.
[133] R. Lawson, "Implications of surface temperatures in the diagnosis of breast cancer," *Canadian Medical Association Journal,* vol. 75, p. 309, 1956.
[134] R. Lawson, "Thermography; a new tool in the investigation of breast lesions," *Canadian services medical journal,* vol. 8, p. 517, 1957.
[135] R. Lawson, "A new infrared imaging device," *Canadian Medical Association Journal,* vol. 79, p. 402, 1958.
[136] J. P. Brooks, W. B. Perry, A. T. Putnam, and R. E. Karulf, "Thermal imaging in the detection of bowel ischemia," *Diseases of the colon & rectum,* vol. 43, pp. 1319-1321, 2000.
[137] A. Clark, J. Mangat, S. S. Tay, Y. King, C. Monk, P. White*, et al.*, "Facial thermography is a sensitive and specific method for assessing food challenge outcome," *Allergy,* vol. 62, pp. 744-749, 2007.
[138] A. Corvi, B. Innocenti, and R. Mencucci, "Thermography used for analysis and comparison of different cataract surgery procedures based on phacoemulsification," *Physiological measurement,* vol. 27, p. 371, 2006.
[139] S. Fok, E. Ng, and K. Tai, "Early detection and visualization of breast tumor with thermogram and neural network," *Journal of Mechanics in Medicine and Biology,* vol. 2, pp. 185-195, 2002.
[140] S. Fok, E. Ng, and G. Thimm, "Developing case-based reasoning for discovery of breast cancer," *Journal of Mechanics in Medicine and Biology,* vol. 3, pp. 231-245, 2003.
[141] E. Y. Ng and N. Sudharsan, "Computer simulation in conjunction with medical thermography as an adjunct tool for early detection of breast cancer," *BMC cancer,* vol. 4, p. 17, 2004.
[142] P. Kapoor and S. Prasad, "Image processing for early diagnosis of breast cancer using infrared images," in *Computer and Automation Engineering (ICCAE), 2010 The 2nd International Conference on*, 2010, pp. 564-566.
[143] Z. L. Sagi, "Device for use in early detection of breast cancer," ed: Google Patents, 1985.
[144] M. Diakides, J. D. Bronzino, and D. R. Peterson, *Medical Infrared Imaging: Principles and Practices*: CRC press, 2012.
[145] M. Kaczmarek and A. Nowakowski, "Analysis of transient thermal processes for improved visualization of breast cancer using IR imaging," in *Engineering in Medicine and Biology Society, 2003. Proceedings of the 25th Annual International Conference of the IEEE*, 2003, pp. 1113-1116.
[146] H. Qi, P. T. Kuruganti, and W. E. Snyder, "Detecting breast cancer from thermal infrared images by asymmetry analysis," *Medicine and Medical Research,* vol. 38, 1995.
[147] E. Ring and K. Ammer, "The technique of infrared imaging in medicine," *Thermology international,* vol. 10, pp. 7-14, 2000.
[148] J. F. Head, C. Lipari, F. Wang, and R. L. Elliott, "Image analysis of digitized infrared images of the breasts from a first generation infrared imaging system," in *Engineering in Medicine and Biology Society, 1997. Proceedings of the 19th Annual International Conference of the IEEE*, 1997, pp. 681-684.
[149] D. A. Kennedy, T. Lee, and D. Seely, "A comparative review of thermography as a breast cancer screening technique," *Integrative Cancer Therapies,* vol. 8, pp. 9-16, 2009.
[150] Y. Ohashi and L. Uchida, "Applying dynamic thermography in the diagnosis of breast cancer," *Engineering in Medicine and Biology Magazine, IEEE,* vol. 19, pp. 42-51, 2000.
[151] Y. Parisky, A. Sardi, R. Hamm, K. Hughes, L. Esserman, S. Rust*, et al.*, "Efficacy of computerized infrared imaging analysis to evaluate mammographically suspicious lesions," *American Journal of Roentgenology,* vol. 180, pp. 263-269, 2003.
[152] H. J. ISARD, W. BECKER, R. SHILO, and B. J. OSTRUM, "Breast thermography after four years and 10,000 studies," *American Journal of Roentgenology,* vol. 115, pp. 811-821, 1972.

[153] E. C. Fear, X. Li, S. C. Hagness, and M. Stuchly, "Confocal microwave imaging for breast cancer detection: Localization of tumors in three dimensions," *Biomedical Engineering, IEEE Transactions on,* vol. 49, pp. 812-822, 2002.
[154] S. Gabriel, R. Lau, and C. Gabriel, "The dielectric properties of biological tissues: II. Measurements in the frequency range 10 Hz to 20 GHz," *Physics in medicine and biology,* vol. 41, p. 2251, 1996.
[155] J. L. Schepps and K. R. Foster, "The UHF and microwave dielectric properties of normal and tumour tissues: variation in dielectric properties with tissue water content," *Physics in medicine and biology,* vol. 25, p. 1149, 1980.
[156] T. M. Grzegorczyk, P. M. Meaney, P. A. Kaufman, R. M. di Florio-Alexander, and K. D. Paulsen, "Fast 3-D tomographic microwave imaging for breast cancer detection," *Medical Imaging, IEEE Transactions on,* vol. 31, pp. 1584-1592, 2012.
[157] N. C. Haslam, A. R. Gillespie, and C. Haslam, "Aperture synthesis thermography-A new approach to passive microwave temperature measurements in the body," *Microwave Theory and Techniques, IEEE Transactions on,* vol. 32, pp. 829-835, 1984.
[158] A. Barrett, P. C. Myers, and N. Sadowsky, "Detection of breast cancer by microwave radiometry," *Radio Science,* vol. 12, pp. 167-171, 1977.
[159] D. Land, "A clinical microwave thermography system," *IEE Proceedings A (Physical Science, Measurement and Instrumentation, Management and Education, Reviews),* vol. 134, pp. 193-200, 1987.
[160] S. B. Field and C. Franconi, "Physics and technology of hyperthermia," 1987.
[161] E. C. Fear, "Microwave imaging of the breast," *Technology in Cancer Research & Treatment,* vol. 4, pp. 69-82, 2005.
[162] X. Li, E. J. Bond, B. D. Van Veen, and S. C. Hagness, "An overview of ultra-wideband microwave imaging via space-time beamforming for early-stage breast-cancer detection," *Antennas and Propagation Magazine, IEEE,* vol. 47, pp. 19-34, 2005.
[163] A. Fhager, M. Gustafsson, and S. Nordebo, "Image reconstruction in microwave tomography using a dielectric Debye model," *Biomedical Engineering, IEEE Transactions on,* vol. 59, pp. 156-166, 2012.
[164] J. P. Stang, *A Three-dimensional Active Microwave Imaging System for Breast Cancer Screening*: ProQuest, 2008.
[165] J. Bourqui, J. M. Sill, and E. C. Fear, "A prototype system for measuring microwave frequency reflections from the breast," *Journal of Biomedical Imaging,* vol. 2012, p. 9, 2012.
[166] S. Chaudhary, R. Mishra, A. Swarup, and J. M. Thomas, "Dielectric properties of normal & malignant human breast tissues at radiowave & microwave frequencies," *Indian journal of biochemistry & biophysics,* vol. 21, p. 76, 1984.
[167] J. M. Sill and E. C. Fear, "Tissue sensing adaptive radar for breast cancer detection - experimental investigation of simple tumor models," *Microwave Theory and Techniques, IEEE Transactions on,* vol. 53, pp. 3312-3319, 2005.
[168] M. Klemm, J. Leendertz, D. Gibbins, I. Craddock, A. Preece, and R. Benjamin, "Microwave radar-based breast cancer detection: Imaging in inhomogeneous breast phantoms," *Antennas and Wireless Propagation Letters, IEEE,* vol. 8, pp. 1349-1352, 2009.
[169] M. Klemm, I. Craddock, J. Leendertz, A. Preece, and R. Benjamin, "Experimental and clinical results of breast cancer detection using UWB microwave radar," in *Antennas and Propagation Society International Symposium, 2008. AP-S 2008. IEEE*, 2008, pp. 1-4.
[170] E. C. Fear, P. M. Meaney, and M. Stuchly, "Microwaves for breast cancer detection?," *Potentials, IEEE,* vol. 22, pp. 12-18, 2003.
[171] B. S. Garra, E. I. Cespedes, J. Ophir, S. R. Spratt, R. A. Zuurbier, C. M. Magnant*, et al.*, "Elastography of breast lesions: initial clinical results," *Radiology,* vol. 202, pp. 79-86, 1997.

[172] J. L. Gennisson, T. Deffieux, M. Fink, and M. Tanter, "Ultrasound elastography: Principles and techniques," *Diagnostic and Interventional Imaging,* vol. 94, pp. 487-495, 2013/05/01/ 2013.
[173] A. Goddi, M. Bonardi, and S. Alessi, "Breast elastography: a literature review," *Journal of ultrasound,* vol. 15, pp. 192-198, 2012.
[174] N. Cho, W. K. Moon, J. S. Park, J. H. Cha, M. Jang, and M. H. Seong, "Nonpalpable breast masses: evaluation by US elastography," *Korean journal of radiology,* vol. 9, pp. 111-118, 2008.
[175] A. Thomas, S. Kümmel, F. Fritzsche, M. Warm, B. Ebert, B. Hamm*, et al.*, "Real-time sonoelastography performed in addition to B-mode ultrasound and mammography: improved differentiation of breast lesions?," *Academic radiology,* vol. 13, pp. 1496-1504, 2006.
[176] A. Evans, P. Whelehan, K. Thomson, D. McLean, K. Brauer, C. Purdie*, et al.*, "Quantitative shear wave ultrasound elastography: initial experience in solid breast masses," *Breast Cancer Res,* vol. 12, p. R104, 2010.
[177] J. Ophir, I. Cespedes, H. Ponnekanti, Y. Yazdi, and X. Li, "Elastography: a quantitative method for imaging the elasticity of biological tissues," *Ultrasonic imaging,* vol. 13, pp. 111-134, 1991.
[178] P.-B. Claire, S. Mallika, K. L. Karen, and F. I. Michael, "Ultrasonic Elasticity Imaging as a Tool for Breast Cancer Diagnosis and Research," *Current Medical Imaging Reviews,* vol. 2, pp. 157-164, 2006.
[179] H. Zhi, B. Ou, B.-M. Luo, X. Feng, Y.-L. Wen, and H.-Y. Yang, "Comparison of ultrasound elastography, mammography, and sonography in the diagnosis of solid breast lesions," *Journal of ultrasound in medicine,* vol. 26, pp. 807-815, 2007.
[180] I. A. Gheonea, Z. Stoica, and S. Bondari, "Differential diagnosis of breast lesions using ultrasound elastography," *Indian Journal of Radiology and Imaging,* vol. 21, p. 301, 2011.
[181] J. R. Grajo and R. G. Barr, "Compression elasticity imaging of the breast: An overview," *Applied Radiology,* vol. 41, p. 18, 2012.
[182] A. Peters, J. G. Chase, and E. E. Van Houten, "Digital image elasto-tomography: combinatorial and hybrid optimization algorithms for shape-based elastic property reconstruction," *Biomedical Engineering, IEEE Transactions on,* vol. 55, pp. 2575-2583, 2008.
[183] J. G. Chase, E. Van Houten, L. Ray, D. Bates, J.-P. Henderson, C. Ewing*, et al.*, "Digital image-based elasto-tomography for soft tissue imaging," 2004.
[184] A. S. Kashif, T. F. Lotz, M. D. McGarry, A. J. Pattison, and J. G. Chase, "Silicone breast phantoms for elastographic imaging evaluation," *Medical physics,* vol. 40, p. 063503, 2013.
[185] M. I. Hina, G. P. Christopher, K. S. Matthew, H. Marcus, Z. Cong, and J. G. Chase, "Mechanical behaviour of tissue mimicking breast phantom materials," *Biomedical Physics & Engineering Express,* vol. 3, p. 045010, 2017.
[186] A. Peters, H. Uwe-Berger, J. Chase, and E. Houten, "Digital Image–Based Elasto–Tomography: Non–Linear Mechanical Property Reconstruction of Homogeneous Gelatine Phantoms," *Int J Inform Syst Sci,* vol. 2, pp. 512-521, 2006.
[187] A. Peters, J. G. Chase, and E. E. Van Houten, "Digital image elasto-tomography: mechanical property estimation of silicone phantoms," *Medical & biological engineering & computing,* vol. 46, pp. 205-212, 2008.
[188] T. Botterill, T. Lotz, A. Kashif, and J. G. Chase, "Reconstructing 3-D Skin Surface Motion for the DIET Breast Cancer Screening System," *Medical Imaging, IEEE Transactions on,* vol. 33, pp. 1109-1118, 2014.
[189] C. K. Kuhl, R. K. Schmutzler, C. C. Leutner, A. Kempe, E. Wardelmann, A. Hocke*, et al.*, "Breast MR imaging screening in 192 women proved or suspected to be carriers of a breast cancer susceptibility gene: preliminary results 1," *Radiology,* vol. 215, pp. 267-279, 2000.
[190] G. D. Dodd, "Present status of thermography, ultrasound and mammography in breast cancer detection," *Cancer,* vol. 39, pp. 2796-2805, 1977.

[191] T. M. Kolb, J. Lichy, and J. H. Newhouse, "Comparison of the Performance of Screening Mammography, Physical Examination, and Breast US and Evaluation of Factors that Influence Them: An Analysis of 27,825 Patient Evaluations 1," *Radiology,* vol. 225, pp. 165-175, 2002.

[192] R. Manoliu and G. Ooms, "The accuracy of mammography: an analysis of 655 histologically verified cases," *Radiologia clinica,* vol. 46, pp. 422-429, 1976.

[193] R. Ohlinger, H. Heyer, A. Thomas, S. Paepke, H. Warm, U. Klug*, et al.*, "Non-palpable breast lesions in asymptomatic women: diagnostic value of initial ultrasonography and comparison with mammography," *Anticancer research,* vol. 26, pp. 3943-3955, 2006.

[194] S. Habib, H. A. Maseeh-uz-Zaman, K. Niaz, H. Hashmi, and S. Kamal, "Diagnostic accuracy of Tc-99m-MIBI for breast carcinoma in correlation with mammography and sonography," *J Coll Physicians Surg Pak,* vol. 19, pp. 622-6, 2009.

[195] C. Standertskjöld-Nordenstam and U. Svinhufvud, "Mammography of symptomatic breasts. A report on 1119 consecutive patients," in *Annales chirurgiae et gynaecologiae*, 1979, pp. 48-53.

[196] E. Luczyńska, S. Heinze-Paluchowska, S. Dyczek, P. Blecharz, J. Rys, and M. Reinfuss, "Contrast-enhanced spectral mammography: comparison with conventional mammography and histopathology in 152 women," *Korean Journal of Radiology,* vol. 15, pp. 689-696, 2014.

[197] R. Egan and K. Egan, "Detection of breast carcinoma: comparison of automated water-path whole-breast sonography, mammography, and physical examination," *American journal of roentgenology,* vol. 143, pp. 493-497, 1984.

[198] C. Spick, D. H. Szolar, K. W. Preidler, M. Tillich, P. Reittner, and P. A. Baltzer, "Breast MRI used as a problem-solving tool reliably excludes malignancy," *European journal of radiology,* vol. 84, pp. 61-64, 2015.

[199] M. Heinisch, H. Gallowitsch, P. Mikosch, E. Kresnik, G. Kumnig, I. Gomez*, et al.*, "Comparison of FDG-PET and dynamic contrast-enhanced MRI in the evaluation of suggestive breast lesions," *The breast,* vol. 12, pp. 17-22, 2003.

[200] Y. Hayashi, H. Takei, S. Nozu, Y. Tochigi, A. Ichikawa, N. Kobayashi*, et al.*, "Analysis of complete response by MRI following neoadjuvant chemotherapy predicts pathological tumor responses differently for molecular subtypes of breast cancer," *Oncology letters,* vol. 5, pp. 83-89, 2013.

[201] P. Belli, M. Costantini, C. Malaspina, A. Magistrelli, G. Latorre, and L. Bonomo, "MRI accuracy in residual disease evaluation in breast cancer patients treated with neoadjuvant chemotherapy," *Clinical radiology,* vol. 61, pp. 946-953, 2006.

[202] H. Satake, K. Shimamoto, A. Sawaki, R. Niimi, Y. Ando, T. Ishiguchi*, et al.*, "Role of ultrasonography in the detection of intraductal spread of breast cancer: correlation with pathologic findings, mammography and MR imaging," *European radiology,* vol. 10, pp. 1726-1732, 2000.

[203] F. Lumachi, A. Tregnaghi, G. Ferretti, M. Povolato, M. Marzola, P. Zucchetta*, et al.*, "Accuracy of ultrasonography and 99m Tc-sestamibi scintimammography for assessing axillary lymph node status in breast cancer patients. A prospective study," *European Journal of Surgical Oncology (EJSO),* vol. 32, pp. 933-936, 2006.

[204] A. T. Stavros, D. Thickman, C. L. Rapp, M. A. Dennis, S. H. Parker, and G. A. Sisney, "Solid breast nodules: use of sonography to distinguish between benign and malignant lesions," *Radiology,* vol. 196, pp. 123-134, 1995.

[205] R.-F. Chang, W.-J. Wu, W. K. Moon, and D.-R. Chen, "Improvement in breast tumor discrimination by support vector machines and speckle-emphasis texture analysis," *Ultrasound in medicine & biology,* vol. 29, pp. 679-686, 2003.

[206] R.-F. Chang, W.-J. Wu, W. K. Moon, Y.-H. Chou, and D.-R. Chen, "Support vector machines for diagnosis of breast tumors on US images," *Academic radiology,* vol. 10, pp. 189-197, 2003.
[207] X. Tang, H. Ding, Y.-e. Yuan, and Q. Wang, "Morphological measurement of localized temperature increase amplitudes in breast infrared thermograms and its clinical application," *Biomedical Signal Processing and Control,* vol. 3, pp. 312-318, 2008.
[208] A. M. Ovechkin and G. Yoon, "Infrared imaging for screening breast cancer metastasis based on abnormal temperature distribution," *Journal of the Optical Society of Korea,* vol. 9, pp. 157-161, 2005.
[209] A. E. Collett, C. Guilfoyle, E. J. Gracely, T. G. Frazier, and A. V. Barrio, "Infrared Imaging Does Not Predict the Presence of Malignancy in Patients with Suspicious Radiologic Breast Abnormalities," *The breast journal,* vol. 20, pp. 375-380, 2014.
[210] M. Kontos, R. Wilson, and I. Fentiman, "Digital infrared thermal imaging (DITI) of breast lesions: sensitivity and specificity of detection of primary breast cancers," *Clinical radiology,* vol. 66, pp. 536-539, 2011.
[211] T. B. Borchartt, R. Resmini, A. Conci, A. Martins, A. C. Silva, E. M. Diniz*, et al.*, "Thermal feature analysis to aid on breast disease diagnosis," in *Proceedings of 21st Brazilian Congress of Mechanical Engineering—COBEM2011*, 2011, pp. 24-28.
[212] C. FARRELL, J. D. WALLACE, and C. M. MANSFIELD, "The use of thermography in detection of metastatic breast cancer," *American Journal of Roentgenology,* vol. 111, pp. 148-152, 1971.
[213] G. M. Giuseppetti, A. Martegani, B. Di Cioccio, and S. Baldassarre, "Elastosonography in the diagnosis of the nodular breast lesions: preliminary report," *La Radiologia medica,* vol. 110, pp. 69-76, 2004.
[214] C. De Korte, E. Cespedes, A. Van der Steen, B. Norder, and K. Te Nijenhuis, "Elastic and acoustic properties of vessel mimicking material for elasticity imaging," *Ultrasonic imaging,* vol. 19, pp. 112-126, 1997.
[215] C. J. Teirlinck, R. A. Bezemer, C. Kollmann, J. Lubbers, P. R. Hoskins, P. Fish*, et al.*, "Development of an example flow test object and comparison of five of these test objects, constructed in various laboratories," *Ultrasonics,* vol. 36, pp. 653-660, 1998.
[216] K. Takegami, Y. Kaneko, T. Watanabe, T. Maruyama, Y. Matsumoto, and H. Nagawa, "Polyacrylamide gel containing egg white as new model for irradiation experiments using focused ultrasound," *Ultrasound in medicine & biology,* vol. 30, pp. 1419-1422, 2004.
[217] M. Brewin, L. Pike, D. Rowland, and M. Birch, "The acoustic properties, centered on 20 MHz, of an IEC agar-based tissue-mimicking material and its temperature, frequency and age dependence," *Ultrasound in medicine & biology,* vol. 34, pp. 1292-1306, 2008.
[218] C. Sun, S. D. Pye, J. E. Browne, A. Janeczko, B. Ellis, M. B. Butler*, et al.*, "The speed of sound and attenuation of an IEC agar-based tissue-mimicking material for high frequency ultrasound applications," *Ultrasound in medicine & biology,* vol. 38, pp. 1262-1270, 2012.
[219] S. L. Vieira, T. Z. Pavan, J. E. Junior, and A. A. Carneiro, "Paraffin-gel tissue-mimicking material for ultrasound-guided needle biopsy phantom," *Ultrasound in medicine & biology,* vol. 39, pp. 2477-2484, 2013.
[220] W. Xia, D. Piras, M. Heijblom, W. Steenbergen, T. G. Van Leeuwen, and S. Manohar, "Poly (vinyl alcohol) gels as photoacoustic breast phantoms revisited," *Journal of biomedical optics,* vol. 16, pp. 075002-075002-10, 2011.
[221] W. Li, B. Belmont, J. M. Greve, A. B. Manders, B. C. Downey, X. Zhang*, et al.*, "Polyvinyl chloride as a multimodal tissue-mimicking material with tuned mechanical and medical imaging properties," *Medical Physics,* vol. 43, pp. 5577-5592, 2016.
[222] J. Fromageau, J.-L. Gennisson, C. Schmitt, R. L. Maurice, R. Mongrain, and G. Cloutier, "Estimation of polyvinyl alcohol cryogel mechanical properties with four ultrasound

elastography methods and comparison with gold standard testings," *IEEE transactions on ultrasonics, ferroelectrics, and frequency control,* vol. 54, 2007.

[223] J. Browne, K. Ramnarine, A. Watson, and P. Hoskins, "Assessment of the acoustic properties of common tissue-mimicking test phantoms," *Ultrasound in medicine & biology,* vol. 29, pp. 1053-1060, 2003.

[224] R. Sinkus, J. Lorenzen, D. Schrader, M. Lorenzen, M. Dargatz, and D. Holz, "High-resolution tensor MR elastography for breast tumour detection," *Physics in Medicine and Biology,* vol. 45, p. 1649, 2000.

[225] T. A. Krouskop, T. M. Wheeler, F. Kallel, B. S. Garra, and T. Hall, "Elastic moduli of breast and prostate tissues under compression," *Ultrasonic imaging,* vol. 20, pp. 260-274, 1998.

[226] A. Sarvazyan, A. Skovoroda, S. Emelianov, J. Fowlkes, J. Pipe, R. Adler*, et al.*, "Biophysical bases of elasticity imaging," in *Acoustical imaging*, ed: Springer, 1995, pp. 223-240.

[227] A. Skovoroda, A. Klishko, D. Gusakyan, Y. I. Mayevskii, V. Yermilova, G. Oran-skaya*, et al.*, "Quantitative analysis of the mechanical characteristics of pathologically changed soft biological tissues," *Biophysics,* vol. 40, pp. 1359-1364, 1995.

[228] J. C. Y. Lai, C. B. Soh, E. Gunawan, and K. S. Low, "Homogeneous and heterogeneous breast phantoms for ultra-wideband microwave imaging applications," *Progress In Electromagnetics Research,* vol. 100, pp. 397-415, 2010.

[229] B. Henin, A. Abbosh, and W. Al Abdulla, "Electro-biomechanical breast phantom for hybrid breast imaging," in *2015 International Symposium on Antennas and Propagation (ISAP)*, 2015, pp. 1-3.

[230] M. O. Culjat, D. Goldenberg, P. Tewari, and R. S. Singh, "A review of tissue substitutes for ultrasound imaging," *Ultrasound in medicine & biology,* vol. 36, pp. 861-873, 2010.

[231] T. J. Hall, M. Bilgen, M. F. Insana, and T. A. Krouskop, "Phantom materials for elastography," *Ultrasonics, Ferroelectrics, and Frequency Control, IEEE Transactions on,* vol. 44, pp. 1355-1365, 1997.

[232] J. I. Silver, "Development of ultrasound based techniques for measuring skeletal muscle motion," Citeseer, 2009.

[233] Z. P. Theo, L. M. Ernest, R. F. Gary, O. C. Antonio Adilton, and J. H. Timothy, "Nonlinear elastic behavior of phantom materials for elastography," *Physics in Medicine and Biology,* vol. 55, p. 2679, 2010.

[234] P. Kozlov and G. Burdygina, "The structure and properties of solid gelatin and the principles of their modification," *Polymer,* vol. 24, pp. 651-666, 1983.

[235] K. J. Quinn and J. M. Courtney, "Silicones as biomaterials," *British polymer journal,* vol. 20, pp. 25-32, 1988.

[236] M. Lazebnik, E. L. Madsen, G. R. Frank, and S. C. Hagness, "Tissue-mimicking phantom materials for narrowband and ultrawideband microwave applications," *Physics in medicine and biology,* vol. 50, p. 4245, 2005.

[237] K. Manickam, R. R. Machireddy, and S. Seshadri, "Characterization of biomechanical properties of agar based tissue mimicking phantoms for ultrasound stiffness imaging techniques," *Journal of the Mechanical Behavior of Biomedical Materials,* vol. 35, pp. 132-143, 2014/07/01/ 2014.

[238] E. L. Madsen, M. A. Hobson, H. Shi, T. Varghese, and G. R. Frank, "Tissue-mimicking agar/gelatin materials for use in heterogeneous elastography phantoms," *Physics in medicine and biology,* vol. 50, p. 5597, 2005.

[239] T. Z. Pavan, E. L. Madsen, G. R. Frank, A. A. O. Carneiro, and T. J. Hall, "Nonlinear elastic behavior of phantom materials for elastography," *Physics in medicine and biology,* vol. 55, p. 2679, 2010.

[240] X. Liang, A. L. Oldenburg, V. Crecea, S. Kalyanam, M. F. Insana, and S. A. Boppart, "Modeling and measurement of tissue elastic moduli using optical coherence elastography," in *Biomedical Optics (BiOS) 2008*, 2008, pp. 685803-685803-8.

[241] A. I. Farrer, H. Odéen, J. de Bever, B. Coats, D. L. Parker, A. Payne*, et al.*, "Characterization and evaluation of tissue-mimicking gelatin phantoms for use with MRgFUS," *Journal of therapeutic ultrasound,* vol. 3, p. 9, 2015.

[242] A. Payne, J. Bever, A. Farrer, B. Coats, D. L. Parker, and D. A. Christensen, "A simulation technique for 3D MR-guided acoustic radiation force imaging," *Medical physics,* vol. 42, pp. 674-684, 2015.

[243] *Dynamic Mechanical Analysis Q800 Specifications*. Available: www.tainstruments.com/pdf/brochure/dma.pdf

[244] M. Mooney, "A theory of large elastic deformation," *Journal of applied physics,* vol. 11, pp. 582-592, 1940.

[245] R. S. Rivlin and D. Saunders, "Large elastic deformations of isotropic materials. VII. Experiments on the deformation of rubber," *Philosophical Transactions of the Royal Society of London A: Mathematical, Physical and Engineering Sciences,* vol. 243, pp. 251-288, 1951.

[246] R. Ogden, "Large deformation isotropic elasticity—On the correlation of theory and experiment for incompressible rubberlike solids," *Rubber Chemistry and Technology,* vol. 46, pp. 398-416, 1973.

[247] S. Diridollou, D. Black, J. Lagarde, Y. Gall, M. Berson, V. Vabre*, et al.*, "Sex-and site-dependent variations in the thickness and mechanical properties of human skin in vivo," *International journal of cosmetic science,* vol. 22, pp. 421-435, 2000.

[248] S. Abbas, Z. Judit, and P. Donald, "Elastic moduli of normal and pathological human breast tissues: an inversion-technique-based investigation of 169 samples," *Physics in Medicine and Biology,* vol. 52, p. 1565, 2007.

[249] V. Nayar, J. Weiland, C. Nelson, and A. Hodge, "Elastic and viscoelastic characterization of agar," *Journal of the mechanical behavior of biomedical materials,* vol. 7, pp. 60-68, 2012.

[250] Q. Yu-Neifert, "A three-dimensional finite element model to predict the applicability of holographic interferometry to breast tumor detection," University of Akron, Department of Biomedical Engineering, 1995.

[251] Y. Kita, R. Highnam, and M. Brady, "Correspondence between different view breast X-rays using a simulation of breast deformation," in *Computer Vision and Pattern Recognition, 1998. Proceedings. 1998 IEEE Computer Society Conference on*, 1998, pp. 700-707.

[252] F. S. Azar, D. N. Metaxas, and M. D. Schnall, "A finite element model of the breast for predicting mechanical deformations during biopsy procedures," in *Mathematical Methods in Biomedical Image Analysis, 2000. Proceedings. IEEE Workshop on*, 2000, pp. 38-45.

[253] A. Samani, J. Bishop, M. J. Yaffe, and D. B. Plewes, "Biomechanical 3-D finite element modeling of the human breast using MRI data," *IEEE transactions on medical imaging,* vol. 20, pp. 271-279, 2001.

[254] P. R. Bakic, "Breast tissue description and modeling in mammography," 2001.

[255] A. P. Del Palomar, B. Calvo, J. Herrero, J. López, and M. Doblaré, "A finite element model to accurately predict real deformations of the breast," *Medical Engineering & Physics,* vol. 30, pp. 1089-1097, 2008.

[256] P. Pathmanathan, D. Gavaghan, J. Whiteley, M. Brady, M. Nash, P. Nielsen*, et al.*, "Predicting tumour location by simulating large deformations of the breast using a 3D finite element model and nonlinear elasticity," in *International Conference on Medical Image Computing and Computer-Assisted Intervention*, 2004, pp. 217-224.

[257] Y. Zhang, Y. Qiu, D. B. Goldgof, S. Sarkar, and L. Li, "3D finite element modeling of nonrigid breast deformation for feature registration in-ray and MR images," in *Applications of Computer Vision, 2007. WACV'07. IEEE Workshop on*, 2007, pp. 38-38.

[258] Y.-L. Liu, P.-Y. Liu, M.-L. Huang, J.-T. Hsu, R.-P. Han, and J. Wu, "Simulation of breast compression in mammography using finite element analysis: A preliminary study," *Radiation Physics and Chemistry,* vol. 140, pp. 295-299, 2017/11/01/ 2017.

[259] F. S. Azar, D. N. Metaxas, and M. D. Schnall, "A deformable finite element model of the breast for predicting mechanical deformations under external perturbations," *Academic Radiology,* vol. 8, pp. 965-975, 2001.

[260] N. Ruiter, T. Müller, R. Stotzka, H. Gemmeke, J. Reichenbach, and W. Kaiser, "Automatic image matching for breast cancer diagnostics by a 3d deformation model of the mamma," *Biomedizinische Technik/Biomedical Engineering,* vol. 47, pp. 644-647, 2002.

[261] A. W. C. Lee, V. Rajagopal, T. P. Babarenda Gamage, A. J. Doyle, P. M. F. Nielsen, and M. P. Nash, "Breast lesion co-localisation between X-ray and MR images using finite element modelling," *Medical Image Analysis,* vol. 17, pp. 1256-1264, 2013/12/01/ 2013.

[262] J. A. Schnabel, C. Tanner, A. D. Castellano-Smith, A. Degenhard, M. O. Leach, D. R. Hose*, et al.*, "Validation of nonrigid image registration using finite-element methods: application to breast MR images," *IEEE transactions on medical imaging,* vol. 22, pp. 238-247, 2003.

[263] C. W. Washington and M. I. Miga, "Modality independent elastography (MIE): A new approach to elasticity imaging," *IEEE transactions on medical imaging,* vol. 23, pp. 1117-1128, 2004.

[264] V. Rajagopal, J. H. Chung, D. Bullivant, P. M. Nielsen, and M. P. Nash, "Determining the finite elasticity reference state from a loaded configuration," *International Journal for Numerical Methods in Engineering,* vol. 72, pp. 1434-1451, 2007.

[265] A. S. Kashif, "Imaging technology for digital image based motion detection in the DIET breast cancer screening system," 2013.

[266] Y.-c. Fung, *Biomechanics: mechanical properties of living tissues*: Springer Science & Business Media, 2013.

[267] Hibbitt, Karlsson, and Sorensen, *ABAQUS/standard User's Manual* vol. 1: Hibbitt, Karlsson & Sorensen, 2001.

[268] V. ABAQUS, "6.14 Documentation," *Dassault Systemes Simulia Corporation,* 2014.

[269] V. Rajagopal, P. Nielsen, and M. Nash, "A 3D finite element model of the breast to study breast cancer," in *World congress on medical physics and biomedical engineering*, 2003.

[270] P. Wellman, R. D. Howe, E. Dalton, and K. A. Kern, "Breast tissue stiffness in compression is correlated to histological diagnosis," *Harvard BioRobotics Laboratory Technical Report,* 1999.

[271] B. D. Bradley, A. D. Chan, and M. J. D. Hayes, "A 3D scanning system for biomedical purposes using the laser light-sectioning method and elliptical fourier descriptors," in *Medical Measurements and Applications, 2008. MeMeA 2008. IEEE International Workshop on*, 2008, pp. 101-105.

[272] M. Hajeer, D. Millett, A. Ayoub, and J. Siebert, "Current Products and Practices: Applications of 3D imaging in orthodontics: Part I," *Journal of orthodontics,* vol. 31, pp. 62-70, 2004.

[273] R. J. Hennessy, S. McLearie, A. Kinsella, and J. L. Waddington, "Facial surface analysis by 3D laser scanning and geometric morphometrics in relation to sexual dimorphism in cerebral–craniofacial morphogenesis and cognitive function," *Journal of anatomy,* vol. 207, pp. 283-295, 2005.

[274] N. H. Trinh, J. Lester, B. C. Fleming, G. Tung, and B. B. Kimia, "Accurate measurement of cartilage morphology using a 3D laser scanner," in *International Workshop on Computer Vision Approaches to Medical Image Analysis*, 2006, pp. 37-48.

[275] Z. B. Azouz, C. Shu, R. Lepage, and M. Rioux, "Extracting main modes of human body shape variation from 3D anthropometric data," in *3-D Digital Imaging and Modeling, 2005. 3DIM 2005. Fifth International Conference on*, 2005, pp. 335-342.

[276] G. C. Righini, A. Tajani, and A. Cutolo, *An introduction to optoelectronic sensors* vol. 7: World Scientific, 2009.
[277] J. Sokołowski, M. Lachowska, R. Bartoszewicz, and K. Niemczyk, "Methodology for Intraoperative Laser Doppler Vibrometry Measurements of Ossicular Chain Reconstruction," *Clinical and experimental otorhinolaryngology,* vol. 9, p. 98, 2016.